Università degli Studi della Basilicata

Dottorato di Ricerca in

Ingegneria per l'innovazione e lo Sviluppo Sostenibile

ADVANCED MODELLING OF OVER-STROKE DISPLACEMENT CAPACITY FOR CURVED SURFACE SLIDER DEVICES

Settore Scientifico-Disciplinare

ICAR/09

Coordinatrice del Dottorato

Prof.ssa Aurelia Sole

Dottorando

Dott. Alessio Telesca

Tutor

Prof. Felice Carlo Ponzo

Co-tutor

Prof. Antonio Di Cesare

Ciclo XXXIV

Acknowledgements

I would like to spend here some words to thank my supervisors Prof. Felice Ponzo and Antonio Di Cesare for giving me the opportunity to work with them in this research project, for being my guides in all of its phases, and for supporting me with their knowledge, I'm very grateful.

I am also grateful to all the people met in these three years in the School of Engineering at the UNIBAS, Domenico Nigro, Gianluca Auletta, Nicla Lamarucciola, Antonella Nigro and Antonello Mossucca, thanks, to you all, the working environment you created has been warm and inspiring. A special thank is due to Luciano Viggiani a friend rather than a colleague.

I would also like to acknowledge the financial support of RELUIS 2019–2021 project funded by the Italian Civil Protection Department, Mrs. Maria Gabriella Castellano and Mr. Samuele Infanti from FIP MEC srl [https://www.fipmec.it/] and Mr. Alberto Pavese and Mr. Marco Furinghetti from the EUCENTRE Foundation [https://www.eucentre.it/] for providing support in the laboratory testing phase and for the inspiring professional exchange of ideas.

Dear family and friends, words could never be enough to thank you all, you're all very precious to me and I hope I'll give back to you all the love I've received. I wish to thank my dad, my sister and my whole family for all the love given, you made me who I am, you always entrusted me, you always supported me, and I'm infinitely grateful. Thank you Faby and Frank, for all the support and the trust in these years, every time we meet I feel like home, and I'm very grateful. Thanks, Alice for the days spent singing together and for always being present for me, thanks Gaia for the chats for opening with me, and for being a good friend.

Thank you, my friends, Eros and Martin, for always having my back, our bond is strong and I feel deeply connected to you. Thanks, Pierluigi for the climbing adventures, the weekends of nature and for all the laughs. Thanks, Simone for being a good friend, for the support and the trust. Thank you, Marcello, for the good time together, all the laughs and to always inspire me with new ideas. Thank you, Angelo, for believing and trusting me more than I do and for your always precious advices. Thank you, Paola, for the intimate chats, for the laughs and for the great trust. Thanks to Francesco e Letizia, you have all my respect, you are caring advisers and I'm thankful for the time spent together. And lastly, thank you Monica, for the trust, the respect and all the kind words you've had for me, last year we made a lot of joyful experiences together, and I'll always carry them in my heart.

Contents

Abstract

This doctoral dissertation aims to report on the research work carried out and to provide a contribution to the field of seismic base isolation. Since its introduction, the base isolation strategy proved to be an effective solution for the protection of structures and their components from the earthquake-induced damage, enhancing their resilience and implying a significative decrease in time and cost of repair compared to a conventional fixed-base structure.

Sliding isolation devices feature some important characteristics, over other devices, that make them particularly suitable for the application in the existing buildings retrofit such as the high displacements capacity combined with limited plan dimensions. Even though these devices diffusion has gotten more popular worldwide in last years, a full understanding of their performances and limits as well as their behaviour under real seismic excitations has not been yet completely achieved. When Curved Surface Sliders reach their displacement capacity, they enter the so-called over-stroke sliding regime which is characterized by an increase in stiffness and friction coefficient. While in the over-stroke displacements regime, anyways, sliding isolators are still capable, until certain threshold values, of preserving their ability to support gravity loads.

In this doctoral dissertation, the analysis of Curved Surface Sliding devices influence on different structures and under different configurations is presented and a tool for to help professionals in the design phase is provided. The research main focuses are: i) the numerical investigation of the over-stroke displacement influence on base isolated structures; ii) the numerical investigation of displacement retaining elements influence on base isolated structures; iii) the development of a mechanical model and an algebraic solution describing the over-stroke sliding regime and the associated limit displacements.

Introduction

The experience gained from recent earthquakes together with the scientific and technical advances contributed to the development of new anti-seismic techniques and to make important progress in earthquake engineering. One of the most recent and consolidated anti-seismic design approaches is the performance-based design which sets limit conditions and damage scenarios to be prevented during seismic events with a certain intensity. This approach aims at preventing the structural collapse involving local ductile failure at key predictable locations on structural elements and on non-structural elements. Recent earthquakes proved the performance-based design efficiency in preventing collapse but also highlighted the consequent economic loss linked to the non-structural damaged elements repair. The unsustainable repair costs are even higher and problematic in the case of strategic structures such as hospitals whose content is very valuable and whose full operability is required immediately after strong seismic events.

Base-isolation is one of the seismic protection strategies which aims at creating resilient buildings by reducing base shear forces and floor accelerations which are accountable for the major damage onto non-structural components. The base isolation technique diffusion has significantly grown in last years leading to the development of more and more efficient isolation devices. The base isolation technique effectiveness relies on isolators technology, and on the full knowledge of their dynamic behaviour which is currently being studied in great detail and which is influencing the updating and the revision of current building codes.

The mostly diffused anti-seismic devices are the elastomeric isolators and Curved Surface Sliders (CSS). CSS devices are based on the pendulum principle granting them a good recentring capability, and their functioning is governed by a friction mechanism which provides good energy-dissipation. Although the basic functioning principles of CSS devices are very

simple, their behaviour has not been fully investigated. The friction mechanism depends on large number of parameters such as the axial load, the sliding velocity, the material roughness, the temperature and the aging state of the sliding components. All of these parameters are subjected to a significant variability during seismic events, and their influence on the dynamic behaviour of CSS devices is not fully known. Moreover, CSS devices are capable, in some mechanical configurations which do not include displacement retaining elements, to accommodate displacements even larger than their displacement capacity. When such a displacement occurs, the CSS bearing enter in the so-called Over-Stroke sliding regime which is characterized by different stiffness and friction coefficients. The over-stroke effect has been poorly investigated mainly due to a construction practice, only allowed by American standards, which tends to limit displacements higher than certain threshold values, employing mechanical elements such as restraining rings.

The present doctoral dissertation scope is the analysis of the performances of curved surface sliding seismic isolators with retaining elements or considering the over-stroke displacements and on characterizing their behaviour through an algebraic solution capable of representing the over-stroke sliding regime and the associated limit displacements.

In *Chapter 1*, a summary of seismic isolation base concepts and a general overview of the current codes provisions and requirement is reported. *Chapter 2* provides a detailed description of the Curved Surface Sliding isolators starting from their main components and its kinematics. Three main typologies of CSS devices are presented, namely Single, Double and Triple CSS. Mathematical models available in literature that describe the main principles of operations and tribological aspects of devices behaviour are presented. The basic theories reported in this section are illustrated as a basis for further investigations made in successive sections. In *Chapter 3* the Over-stroke behaviour of Double Concave Surface Sliders (DCCSS) is presented. The phenomenon is investigated through experimental tests and an *ad-hoc* numerical model

built within the OpenSEES® Framework is proposed and validated. Moreover, an insight on displacement retaining elements is given providing, in this case too, a numerical OpenSEES model capable of representing their force vs displacement behaviour. A final summary of presented models is provided to be used within the body of the present document. *Chapter 4* presents the seismic risk probabilistic assessment, and how it is dealt with in later sections employing fragility functions associated to structures and the annual rates of failure combining both the structural vulnerability and the site hazard function. *Chapter 5* reports on the study about the influence of the over-stroke effect on the seismic performance of civil use buildings. In particular, eight three-dimensional OpenSEES structural models are presented. Nonlinear static analyses are performed onto the models built within the RINTC 2019-21 research project which are then upgraded with a base-isolation DCCSS system. Nonlinear Time History Analyses (NTHA) are performed presenting a specific seismic input chosen through the conditional spectrum approach. Results are finally presented in terms of fragility curves, annual frequencies of exceedance and annual rates of failure. In *Chapter 6* the influence of retaining elements on the structural response of base-isolated buildings is investigated. In particular, two parametric analyses are performed featuring either unlimited stiffness and finite stiffness retaining elements. As done in the previous section, case study structures are described, nonlinear static analyses and NTHA are performed and results are presented in terms of fragility curves, annual frequencies of exceedance and annual rates of failure. In *Chapter 7* the algebraic solution development for the over-stroke sliding regime constitutive law and for the associated limit displacements is presented. The algebraic solution is developed on the basis of consolidated past theories, and two limit displacements respectively related to the attainment of a contact pressure limit value and to the condition in which the isolation device experiences vertical instability are algebraically described. The algebraic solution is compared to results from experimental tests and from a more complex numerical model showing in all cases a good

reliability. The algebraic solution is finally integrated within a Matlab® script capable of determining displacements and forces limit values, and of performing NTHA on a Single Degree of Freedom DCCSS model employing the Newmark Equation of Motion integration. Finally in *Chapter 8* the main outcomes of the study are summarized, the innovative findings are enlightened, and general indications are drawn.

1 Seismic isolation

Seismic isolation is a passive structural protection approach to protect structures and their components, from the damaging effects of earthquakes. It is based on the principle of separating the superstructure from the base action of ground motions, thus it aims to reduce the seismic demand rather than increasing the resistance of the structure. Generally, earthquakes acceleration response spectra are characterized by strong amplifications in low period range, which corresponds with the fundamental period of vibration of most fixed-base structures. The isolation system is usually placed below the main mass of the structure, ad it is designed to reduce its the seismic response by increasing the fundamental period and entering in a lower acceleration area of the response spectrum (Figure 1.1 a). Such a designed isolation system keeps the structure in an elastic range by drastically reducing ground motion accelerations, and allows the structure to withstand strong earthquakes without significant structural damage. The isolation layer is the interface between the upper part of the structure (superstructure), which is isolated and the lower part (substructure) which is assumed to move together with the ground. The isolation system layer is a critical part in the design process of non-structural components such as the electrical and hydraulic systems of a building. These systems need to accommodate large relative displacements in a short space and are thus equipped with particular components properly designed. The isolation system is required to bear the gravity loads of the superstructure and the non-seismic vertical and lateral forces such as wind loads, to avoid engaging the lateral motion when it is not required. Isolation systems are thus provided with a low horizontal stiffness capable of retaining them from moving for low stresses, with a large horizontal capacity, and with a geometry and materials capable of granting the ability to support vertical loads. The fundamental period increase led by the base isolation reduces, on the one hand, the accelerations on the superstructure, but increases, on the other hand, the spectral displacements (Figure 1.1 b). In order to avoid excessive lateral displacements which would

affect the design and the safety of building systems, isolation systems feature bearings which are characterized by proper restoring capabilities, or bearings without any restoring capability coupled by supplemental dissipative and recentring devices. Nowadays the base isolation technique is being more and more implemented in the seismic retrofit of existing structures designed with outdated building codes. The social and economic benefits of seismic isolation find their maximum expression in the application onto buildings that are required to remain completely operational even after a strong earthquake, such as hospitals and fire stations and on structures with a content value much higher than that of the structural components, such as museums and banks.

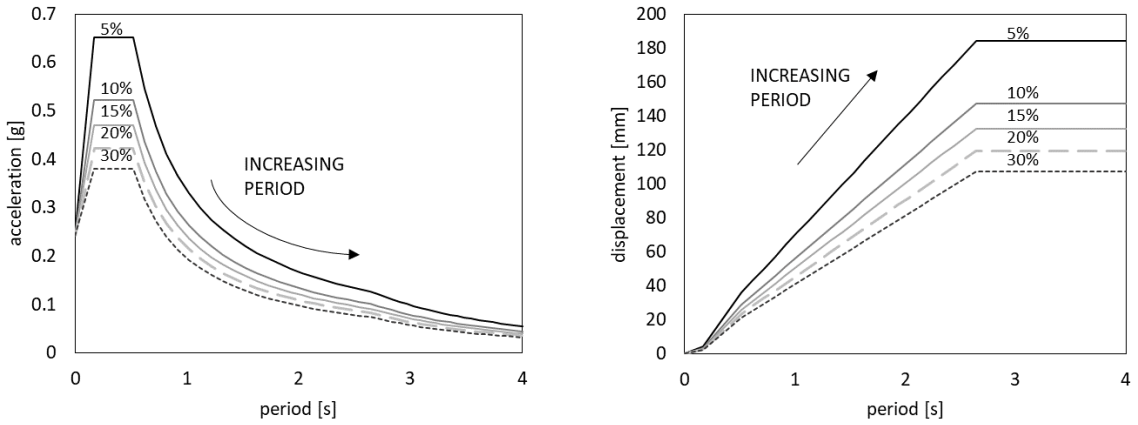

a) b)

Figure 1.1. Seismic isolation theory: shift of the fundamental period of the structure on example a) acceleration and displacement b) response spectra.

1.1 Isolation devices

An isolation system is composed of many isolation devices, nowadays there are a lot of isolation devices which differ in terms of constructive technology, materials, geometry and functioning.

The mostly diffused anti-seismic devices are the elastomeric isolators and Curved Surface Sliders (CSS). Elastomeric isolators can be constructed using different geometries and materials

but usually feature a series of rubber and steel layer. Their seismic behaviour is mainly based on the rubber characteristics which grants a good energy dissipation and re-centring force, while steel layers provide the required vertical load bearing capability. Three main typologies of rubber bearings can be distinguished based on their damping capability:

- Low Damping Rubber Bearings (LDRB) composed of rubber layers separated by steel sheets. When the earthquake lateral force hits these devices, the shear deformation of rubber layers provides the required isolation, however the dissipative capability is usually low so that the isolation system requires additional devices;
- High Damping Rubber Bearing (HDRB) which differs from the LDRB bearing for its material molecular structure. These devices equivalent damping ratio range from 6 to 10% resulting in a wider hysteretic loop. The energy dissipation, however, is still limited, and an HDRB base isolation system may require additional damping devices for medium to high intensity ground motions;
- Lead Rubber Bearing (LRB) composed of an elastomeric shell featuring a vertical lead core capable of increasing the damping ratio up to 40%. The lead core provides a significantly higher reaction force for the bearing, compared to LDRB and HDRB, resulting in a wider hysteretic loop and in a higher damping capability. LRBs are the most applied elastomeric isolators, and their implementation in an isolation system does not require any additional elements.

Sliding isolator are composed by a certain number of moving parts (at least two) made up of steel and composite materials which slide one on another expressing a specific frictional force. the mostly used sliding isolators are:

- Flat Surface Sliders (FSS) are free sliding bearings with two or more flat steel sliding surfaces in contact through friction pads of polymeric materials. These isolators do not

provide any re-centring capability so they are often used in combination with other kind of devices such as elastomeric bearings;

- Curved Surface Sliders (CSS) are composed by at least one concave sliding plate which dynamics employ the pendulum mechanism generating a re-centring force through the radius of curvature and the vertical load on the bearing itself. These devices are usually named as Single, Double, Triple (and so on …) Curved Surface Slider depending on the number of sliding interfaces between the mechanical parts. CSS devices also feature an inner Slider which can be either rigid or articulated (allowing relative movements between its top and bottom surfaces) and features spherical surfaces that match the sliding plates geometry in order to allow relative movements between them.

1.2 Reference standards

Despite the numerous historical proofs of the isolation technique effectiveness, the first base isolation technical standards are quite recent. In Italy the OPCM 3274 [OPCM, 2003] was endorsed in 2003, while at European level the EN 1998 (Eurocode 8) was completed in 2005 [Eurocode 8 part 1, 2004; Eurocode 8 part 2, 2005]. The most recent codes are the European EN15129 [UNI EN 15129, 2009] about anti-seismic devices and the Italian design code for both fixed-base and seismically isolated structures, the "Norme Tecniche per le Costruzioni" NTC2018 [NTC, 2018].

1.2.1 Standards definitions

Since there are very few differences from the Italian Building Code [NTC, 2018], for sake of brevity, only EN 1998-1 [Eurocode 8-part1, 2004] contents are here summarized. The basic provisions for the design of base isolation are:

- the structural elements located above (superstructure) and below (substructure) the isolation layer should be stiff enough in both horizontal and vertical directions to minimize the effects of differential displacements;
- the centre of stiffness and the centre of damping of the isolation system should be as close as possible to the projection on the isolation interface of the centre of mass of the structure in order to minimize the torsional effects;
- the distribution of gravitational loads should be as uniform as possible in order to minimize potential differences in the response of each isolation device;
- the peak seismic displacement of the isolation system is amplified by the safety factor $\gamma_x = 1.20$ which grants the system reliability.

The Eurocode defines a structure as "fully isolated" if, during the seismic motion, it remains within the elastic range, otherwise, it is defined as "partially isolated". The Eurocode 8 also provides the following definitions in order to allow the isolation system modeling using a simplified bilinear law: strength at zero displacement F_0, initial elastic stiffness K_i, post-elastic stiffness K_P. The design displacement of the isolation system d_{bd} is the maximum horizontal displacement of the isolation system in one of the main horizontal directions, occurring for the design seismic action. The effective stiffness K_{eff} is the secant stiffness of the design hysteretic cycle and equals the ratio between the design horizontal force F_{max} and displacement d_{bd}. The effective damping ξ_{eff} of the isolation system represents the percentage of energy dissipated in a cycle having d_{bd} amplitude (see Figure 1.3). The effective period of the isolated structure $T_{eff} = 2\pi\sqrt{M/K_{eff}}$ is the fundamental period of a Single Degree of Freedom (SDoF) system having the mass of the superstructure M and the effective stiffness of the isolation system K_{eff}.

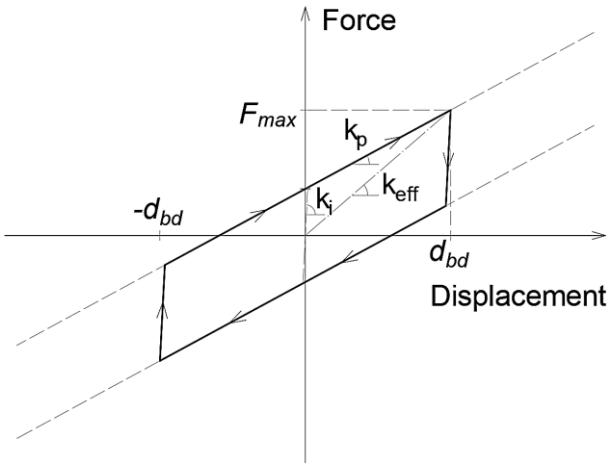

Figure 1.2. Example hysteretic cycle for an isolation system.

1.2.2 Analysis methods

- Nonlinear Time History Analysis (NTHA): is the reference analysis method since it is always applicable. The response of the base isolation system is described using a properly calibrated hysteretic model, while a linear model can be used for the superstructure, both linear and nonlinear models can be used to represent the dynamic response in a less or more (respectively) accurate way. The superstructure viscous damping should not interfere with the isolation system hysteretic damping, and should be the same of the fixed-base superstructure.
- Equivalent linear (dynamic) analysis: is a time-history analysis in which both the isolation system and the superstructure are modelled as linear and viscously damped elements. In particular, the isolation system is modelled by setting its stiffness $K = K_{Eff}$ and its modal damping $\xi = \xi_{eff}$. The torsional effects due to accidental eccentricities are computed statically and superimposed to results of the dynamic analysis being the effects superimposition granted by the linearity of the analysis.

  The isolation system behavior can be modelled as linear if all the following conditions are met:

a) The effective stiffness K_{eff} is not is not lower than 50% of the secant stiffness of the isolation system at a displacement $d = 0.2 \cdot d_{bd}$;

b) The effective damping is lower than 30 percent, $\xi_{eff} < 30\%$;

c) The isolation system force-displacement characteristics variability is lower than 10% due to the rate of loading or due to the vertical loads;

d) The increase of the restoring force in the isolation system for displacements $0.5 \cdot d_{bd} < d < 1.0 \cdot d_{bd}$ is not less than 2,5% of the total gravity load above the isolation system.

- Iterative equivalent linear (dynamic) analysis: since in some cases the effective stiffness K_{eff} or the effective damping ξ_{eff} of the isolation system depend on the design displacement d_{bd}, an iterative procedure should be applied until the difference between the iteration values of d_{bd} does not exceed the 5%.
- Simplified equivalent linear (static) analysis: is based on the assumption that the superstructure behaves as a rigid body translating above the isolation system.

  Once the displacement of the isolation system in each horizontal direction are calculated, the equivalent horizontal forces $f_i = m_i \cdot S_a(T_{eff}, \xi_{eff})$ are applied along both the horizontal main directions and at each floor of the building. A seismic action amplification factor δ_i can be used to account for torsional effects when these are relevant and the centre of stiffness eccentricity with the superstructure centre of mass exceeds the 7.5% of the superstructure length in the orthogonal direction. In addition to conditions for the equivalent linear (dynamic) analysis, this analysis method can only be used when:

  a) the distance from the nearest active fault with $M_s \geq 6.5$ is greater than 15 km;

  b) the largest planar dimension of the superstructure is not greater than 50m;

c) the effective period T_{eff} is higher than 3 times the fundamental period of the fixed-base superstructure T_f and lower than 3 seconds $3T_f \leq T_{eff} \leq 3s$;

d) the substructure is sufficiently rigid to minimise the effects of differential displacements of the ground, in particular, the vertical stiffness of the isolation system is much higher than the effective stiffness $K_v > 150\,K_{eff}$ resulting in negligible vertical displacements;

e) all devices are located above elements of the substructure which support vertical loads.

- Multi-modal linear spectral analysis: is the modal analysis of the base-isolated structure applied separately in all the directions (horizontal and vertical). The isolation system is modelled by considering the effective stiffness (K_{eff}), while 50% uncracked section is usually assumed when computing the stiffness of the superstructure elements. The 50% reduction is operated onto the material elastic module E_m for the damage limitation prescribed by the EN1998 (Eurocode 8) [Eurocode 8 part 1, 2004; Eurocode 8 part 2, 2005]. For modes characterized by a period $T > 0.8 \cdot T_{eff}$, the elastic spectrum should be reduced by the effective damping ξ_{eff} of the isolation system, while for higher modes, when the period $T < 0.8 \cdot T_{eff}$, the spectrum should be considered with its elastic damping $\xi = 5\%$ as in the fixed-base configuration. Torsional effects due to accidental eccentricities are computed statically and then added to results using the effects superimposition.
- Simplified modal linear spectral analysis: is a modal analysis in which the superstructure is considered as a rigid body translating on the isolation layer with the effective period of vibration T_{eff}. This analysis method too allows using the effects superimposition to account for torsional effects.

1.2.3 Seismic design actions

For the purpose of EN 1998, national territories shall be subdivided by the National Authorities into seismic zones, depending on the local hazard. By definition, the hazard within each zone is assumed to be constant. For most of the applications of EN 1998, the hazard is described in terms of a single parameter, i.e., the value of the reference peak ground acceleration on type A ground (bedrock or other rock-like geological formation,), a_{gR}. The reference peak ground acceleration a_{gR}, chosen by the National Authorities for each seismic zone, corresponds to the reference return period T_{NCR} of the seismic action for the No-Collapse Requirement (or equivalently the reference probability of exceedance in 50 years, P_{NCR}). The importance factor $\gamma_I = 1.0$ (coefficient that accounts for the consequences of a structural failure) is assigned to this reference period T_{NCR}. In case of different return periods, the design ground acceleration a_g is equal to γ_I times the reference peak ground acceleration a_{gR}: $a_g = \gamma_I \cdot a_{gR}$.

The Italian Building Code (§ 2.4.1-2.4.3) introduces some other parameters to define the design seismic action. The nominal life of a construction is introduced V_N depending on the type of structure, then the coefficient of use C_U is introduced depending on the structural function and importance and lastly, the reference period V_R is introduced, which is product of the nominal life and the coefficient of use ($V_R = V_N \cdot C_U$). The building code adopts the performance-based seismic design method, based on the definition of performance levels (or limit states). Four are the reference performance levels that needs to be accounted for, and verified in the design process:

- Operability Limit State (OLS): it is one of the serviceability limit states (SLE), and requires all the structural and non-structural components to be fully operational and undamaged after the seismic event;

- Damage Limit State (DLS): this a SLE too and requires all structural and non-structural elements to only suffer light damages. Furthermore, the structural elements stiffness and ductility shall not be invalidated. Overall damages should be easily repaired;
- Life Safety Limit State (LLS): is one of the ultimate limit states (SLU) and refers to the condition in which non-structural elements suffer significant damages but structural elements stiffness and strength are reduced but not impaired. The structural integrity may be restored through local and global reinforcement actions;
- Collapse prevention Limit State (CLS): is a SLU too and refers to the condition in which both structural and non-structural elements suffer severe damages. The structure is not operational but, thanks to the structural elements' residual stiffness and strength against vertical loads it is not collapsed.

The Italian building code adopts the Poisson model to predict the temporal uncertainty of an earthquake with a return period equal to: $T_R = -V_R/ln(1-\rho_{V_R})$, where ρ_{V_R} is the exceedance probability within the reference period V_R of the considered limit state (see Table 1.1).

Table 1.1 Limit states exceeding probability and return periods for a reference period of 50 years

Limit State		Exceeding probability ρ_{V_R}	Return Period T_R (y) V_R=50 y
Serviceability limit states (SLE)	OLS	81%	30
	DLS	63%	50
Ultimate limit states (SLU)	LLS	10%	475
	CLS	5%	975

The reference elastic acceleration spectrum (see Figure 1.3) for structures characterized by a fundamental period $T_1 < 4.0s$ is defined by the Italian code (§ 3.2.3.2.1) is defined by three main period values:

- T_B the period corresponding to the start of the constant acceleration section on the spectrum;

- T_C the period corresponding to the start of the constant velocity section on the spectrum;
- T_D the period corresponding to the start of the constant displacement section;

and by three key parameters a_g, S, F_0 which are:

- a_g the peak ground acceleration for a bedrock soil;
- $S = S_S \cdot S_T$ which is the coefficient accounting for the soil S_S and the topographic S_T conditions;
- F_0 is the maximum spectral amplification factor, defining the maximum reach acceleration on the spectrum $S_{a,max} = a_g \cdot F_0$.

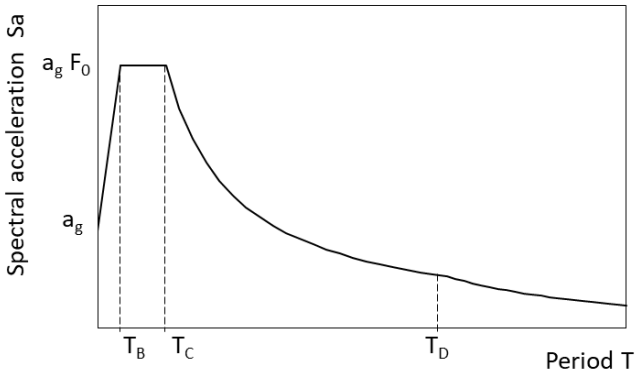

Figure 1.3. Elastic response spectrum and key parameters

1.2.4 Additional comments

The most relevant reference standards for the CSS isolation system design are the italian design code, the NTC18 [NTC 2018] and the european device standard EN 15129 [UNI EN 15129, 2009] which are both based on the provisions of the European design standard EN1998 (Eurocode 8) [Eurocode 8 part 1, 2004; Eurocode 8 part 2, 2005].

Both the NTC18 and the EN15129 require an increased reliability for CSS isolation devices, anyways, the standards provide different design approaches. While in the NTC18 the increased reliability provision is granted by the aforementioned performance-based seismic design with

the Life safety Limit State (LLS) for the superstructure, and the Collapse Limit State (CLS) for the isolation system, in the EN15129 a specific provision is given onto the Bearing Design displacement d_{bd}. The EN15129, thus, grants the increased reliability of CSS devices providing a reliability factor γ_{IS} equal to 1.2 or 1.5 for buildings and bridges respectively, so that the maximum displacement considered in the design procedure is $d_{Ed} = \gamma_{IS} d_{bd}$. Both standards have been considered in the body of the present doctoral dissertation always showing their direct reference.

Another controversial theme dealt with in the present dissertation, is the one of retaining elements. Retaining elements are mechanical or constructive parts which oppose to the free movement of CSS sliders beyond certain displacements. Commonly used elements are restraining rings, their use is admitted by American Standards [ASCE/SEI 7-10, 2013] [ASCE, A. 2010] and consist of steel rings positioned on the border of the housing plates. The constructive technology of restraining rings may be different and the most common types have been described and tested by [Bao and Becker, 2018]. Other displacement restrainers are moat walls, which are external retaining elements placed at a certain distance from CSS devices. In [Masroor and Mosqueda, 2013] an impact element considering moat wall flexibility is proposed based on theoretical observations and experimental simulations, and the implications of the presence of such elements are discussed. Although American standards allow the use of these mechanical elements that serve as stoppers, the European Standard [UNI EN 15129 (2009)] does not and, thus, implies that CSS sliders displacements can possibly go beyond the capacity d_C of devices in the so-called Over-Stroke sliding regime.

The present doctoral dissertation also exposes results from Nonlinear Static (pushover) analyses conducted on base-isolated prototype structures. The Nonlinear static analysis method is not allowed by the italian design standard NTC18 for base-isolated structures, nevertheless American standards such as [FEMA P-695, 2009], [FEMA-356, 2000] allow its employment.

The FEMA P-695 [FEMA P-695, 2009] in section *10.3.5 Nonlinear Static Analysis for Period-Based Ductility, SSFs, Record-to-Record Variability and Overstrength - Pushover Analysis of Isolated Systems*, reports the following:

Nonlinear static analysis is performed on isolated structures with the isolation system free to displace. Pushover forces are based on a uniform pattern of lateral load emulating the approximate pattern of uniform lateral displacement of the isolated structure (at displacements up to significant yielding of the superstructure). Approximately the same ultimate strength is obtained from pushover analyses conducted on the same structure in the fixed-base and base-isolated configurations, but the isolated structure effectively shares system ductility between displacement of the isolation system and displacement of the superstructure. It is also noted that pushover analysis of isolated systems is performed without the moat wall springs (as the sudden increase in stiffness associated with the moat wall is inconsistent with the assumptions used in developing structural ductility).

The FEMA 356 [FEMA-356, 2000], in sections *9.2.5.1 Nonlinear Static Procedure* and *9.3.5.1 Nonlinear Static Procedure* reports the following:

The Nonlinear Static Procedure (NSP) for seismically isolated buildings shall be based on the criteria of Section 3.3.3, except that the target displacement and pattern of applied lateral load shall be based on the criteria given in Sections 9.2.5.1.2 and 9.2.5.1.3, respectively. The pattern of applied lateral load shall be proportional to the distribution of the product of building mass and the deflected shape of the isolated mode of response at the target displacement.

The nonlinear mathematical model of the rehabilitated building shall include the nonlinear force-velocity-displacement characteristics of the energy dissipation devices explicitly, and the mechanical characteristics of the components supporting the devices. Stiffness characteristics shall be consistent with the deformations corresponding to the target displacement and a

frequency equal to the inverse of period T_e, as defined in Section 3.3.3.2. For displacement-dependent devices (*§9.3.5.1.1*) the stiffness characteristics of devices shall be included in the mathematical model.

On the basis of the aforementioned American standards, nonlinear static analyses have been performed throughout the present doctoral dissertation on base isolated structures and compared with results from pushover analyses conducted on their fixed-base counterpart.

2 Curved Surface Slider

The Curved Surface Slider (CSS) is also known as Friction Pendulum Slider® (FPS) and was first developed by Zayas in 1987 [Zayas et al. 1987; Zayas et al., 1990]. The CSS is one of mainly used seismic isolator which includes both re-centring and good dissipation capabilities being based on the pendulum mechanic principle. Since the early applications CSS devices have been used for the seismic protection of bridges and in the retrofit of historic buildings [Mokha et al., 1996]. CSS devices equipped with more than one spherical surface are also referred to as multi-spherical sliding bearings [Fenz and Constantinou 2008]. All multi-spherical sliding bearings have multiple sliding surfaces which can feature different friction and radii of curvature (i.e., stiffness). The sliding movement start on each surface is strongly influenced by the relative values of the friction coefficients and then by the mechanical behaviour of the single parts. The sliding motion can also be intentionally stopped at predefined displacements on each of the sliding surfaces by placing displacement restrainer rings. The overall stiffness and friction of the bearing relies on the characteristics of the surfaces upon which the sliding is occurring. The description of the CSS behaviour therefore requires defining on which surfaces sliding is occurring at any generic instant of a seismic event based on the respective radius of curvature, friction coefficient and displacement capacity. Although the theoretical and mechanical working principles of these devices are simple, their overall behaviour is much more complex than other isolators that are currently used. In this chapter, the functioning of CSS isolators and the friction mechanism are described.

2.1 Construction of CSS devices

2.1.1 Single CSS device

The single CSS device (or Single FP Bearing [Sarlis and Constantinou 2013]) is an anti-seismic isolator based on the pendulum principle. It features a Concave Plate (CP) which is constructed as the circular portion of a sphere with given radius R. The external part of the CP is flat and mechanically anchored to the superstructure, while the inner curved part is in contact with a mechanical part called slider. The slider is composed of two curved convex surfaces, one is characterized by the same radius R of the CP, while the other by a much shorter radius R_r which slides on a concave fixed support (Figure 2.1). The CP is characterized by a friction coefficient μ, while the surface on the interface between the slider and the mechanical support features a μ_r friction. The distance from the sliding interface between slider and CP and the pivot point of the slider itself is called h, while the slider height is h' so that the effective radius of the device can be expressed as $R_{eff} = R + h = R + R_r - h'$.

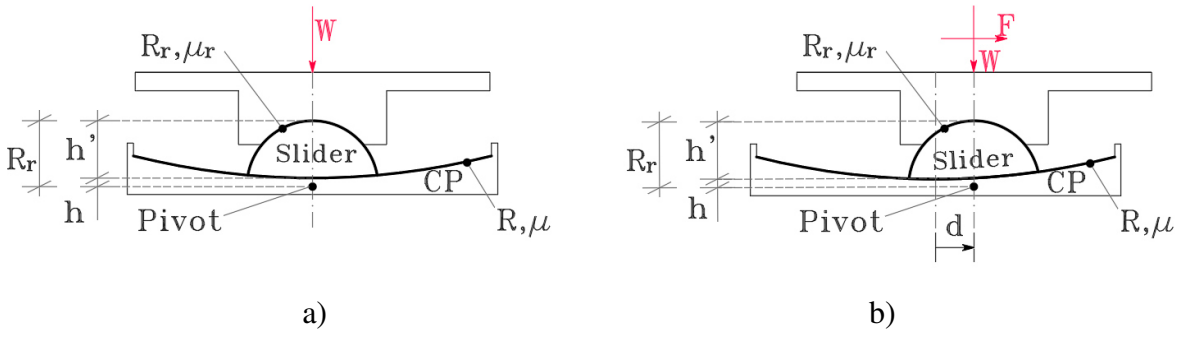

Figure 2.1. Single Curved Surface Slider in a) static and b) dynamic configurations

2.1.2 Double CSS device

The double CSS bearing (or Double Concave Curved Surface Slider (DCCSS) [Di Cesare et al. 2019]) consists of two facing concave stainless-steel surfaces separated by a slider which can be either articulated or rigid. The Top and Bottom Concave Plates (respectively TCP and BCP) are characterized by R_1 and R_2 radii of curvature, respectively, which may be unequal. The coefficients of friction for the TCP and the BCP are as well μ_1 and μ_2, which, just like for the curvature radii, may also be unequal. The nominal displacement capacities of the slider upon the TCP and BCP are d_1 and d_2 respectively, resulting in a total nominal geometric displacement capacity $d = d_1 + d_2$. Due to the effects linked to the slider height h_s and the rotation, the actual displacement capacities are slightly different that the nominal values. The articulation of the slider is necessary when the TCP and the BCP have different mechanical parameters and geometry, and are characterized by different movements. If the TCP and the BCP differ in both geometry and friction coefficient, a rigid slider may cause an uneven material wear and over time, may cause larger variation in its frictional properties. The slider diameter in both articulated and rigid cases is Φ_s and the housing plate inner diameter is Φ_p. Figure 2.2 shows the cross section of an example DCCSS device with a rigid slider. The effective curvature radius for such a CSS device is expressed as follows: $R_{eff} = R_1 + R_2 - h_s$. The main advantage of adopting a DCCSS is that it is characterized by an almost double displacement capacity than a Single CSS device with identical plan dimensions. Accordingly, engineers have recognized that the primary advantage of employing DCCSS bearings is the cost savings that can be achieved through their more compact size.

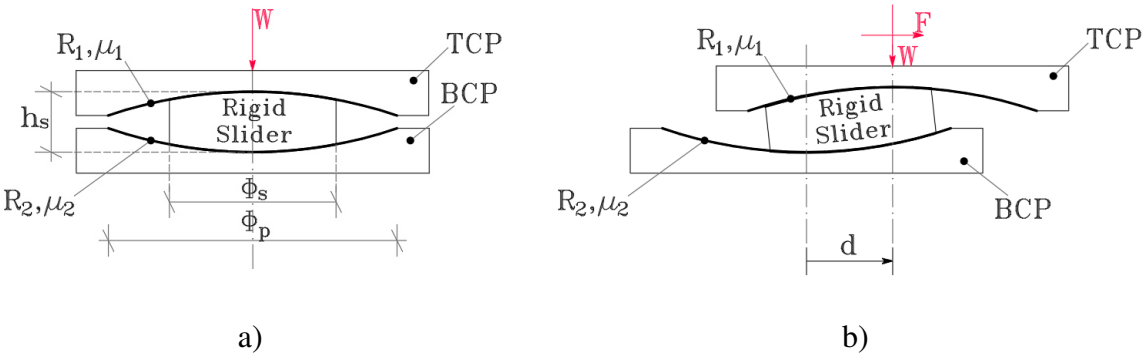

Figure 2.2. Double Concave Curved Surface Slider with Rigid slider in a) static and b) dynamic configurations

2.1.3 Triple CSS device

The triple CSS device consists of two facing concave stainless steel surfaces separated by an internal nested slider (see Figure 2.3). The outer plates effective curvature radii are $R_{eff1} = R_1 - h_1$ and $R_{eff4} = R_4 - h_4$ where R_i is the curvature radius of the generic sliding surface and h_i its distance from the device pivot point. Triple CSS devices feature articulated nested sliders which consists of a rigid slider which separates two concave sliding plates. The slider assembly allows to rotate and accommodate differential rotations and movements between the top and the bottom part of the device. The two inner concave sliding plates and both outer surfaces of the rigid slider are coated with a non-metallic sliding material. Each surface is characterized by its curvature radius R_i and coefficient of friction μ_i. This allows the motion of the rigid slider upon the inner stainless-steel surfaces of the sliding plates. The nominal displacement capacity of each sliding surface is d_i (as with the double CSS bearing, the actual displacement capacities slightly differ from the nominal displacement capacities due to the slider height and rotation). Unlike the single and double CSS bearings, in the triple CSS bearing, there is not a mechanical relationship defining the location of the pivot point which, instead, is located in the instantaneous center of zero rotational velocity of the nested slider. In most cases, the slider height h_s is way smaller than the radius of curvature R_i and the center of zero-rotation

velocity can be assumed at mid-height of the nested slider with a negligible approximation. Similar to the double CSS bearing, triple CSS bearings allow the simultaneous sliding on multiple concave surfaces and therefore can feature a much larger displacement capacity for the same plan dimensions. From an economic standpoint, the economic difference between the costs of DCCSS and Triple CSS bearings of comparable size is negligible.

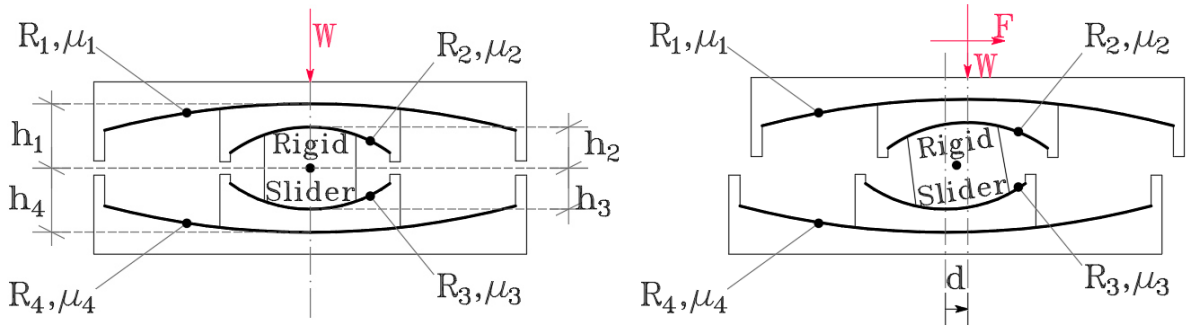

Figure 2.3. Triple Curved Surface Slider in a) static and b) dynamic configurations

2.2 Principles of operation

Principles of operation that apply to all variations of CSS bearings are here discussed. In most of the cases, the theory which applies to the principles of operation for more complex devices is just a logical extension of the theory regulating the single CSS bearing behaviour. The construction of CSS devices, as seen, consists of various arrangements of sliding plates and internal sliders. The first documented isolation system for buildings was a double concave rolling ball bearing that was patented in the US in 1870 by Touaillon [Touaillon et al., 1870] see Figure 2.4. The improvements made in the last 150 years on the system invented and patented by J. Touaillon do not cover the mechanical basic concepts of seismic isolation, but

are focused on the technology and production aspect of isolation devices, which grants a high reliability of materials and mechanical components over the structural lifetime.

The behaviour of CSS devices is based on the theory of the pendulum which assumes that the weight of a system is capable of producing re-centring forces which oppose to the horizontal forces acting on the system itself. The oscillation period, thus, only depends on the radius R of the pendulum, is independent from the mass of the system, and can be expressed as: $T = 2\pi\sqrt{R/g}$, where g is the gravity acceleration.

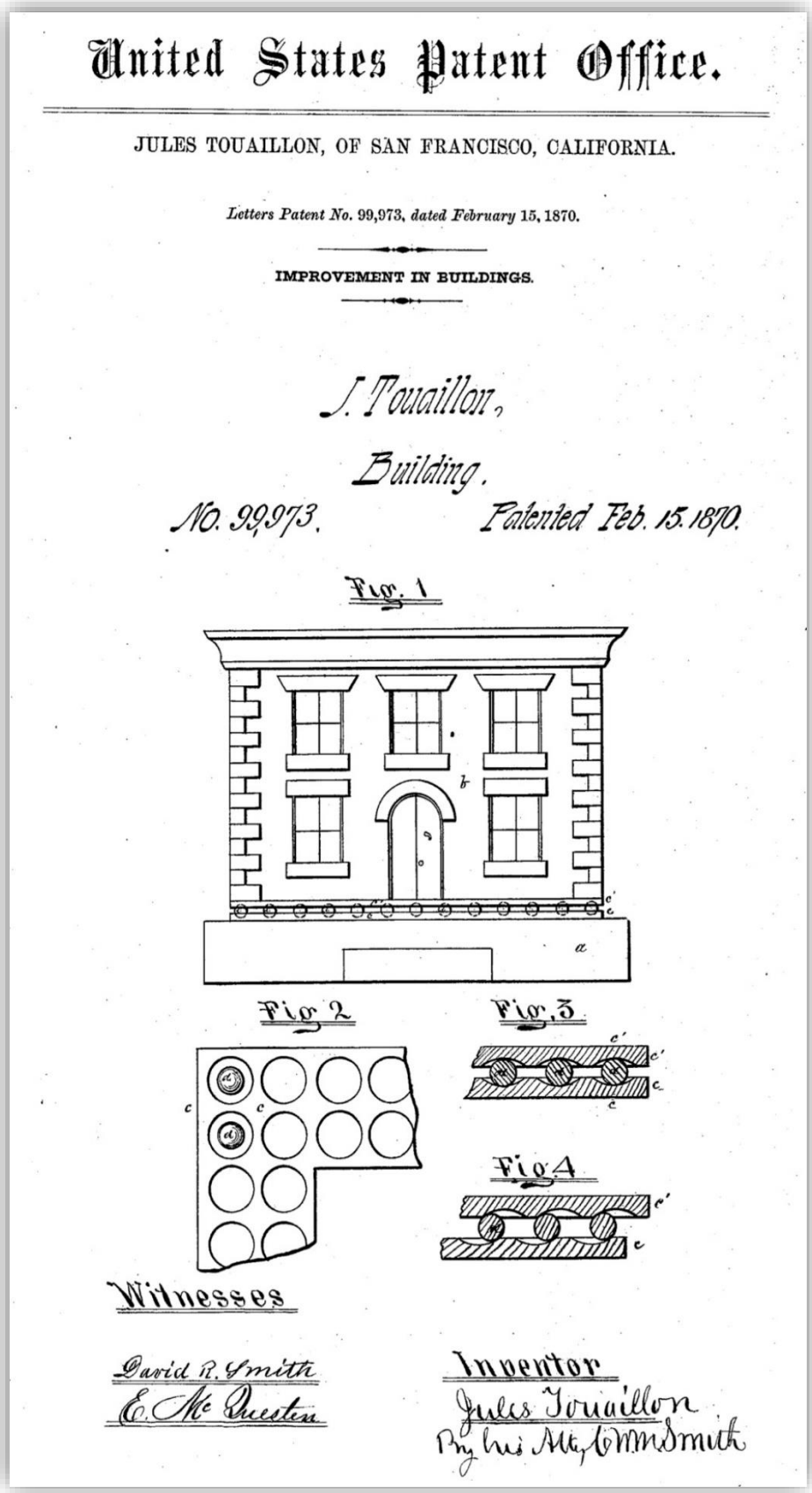

United States Patent Office.

JULES TOUAILLON, OF SAN FRANCISCO, CALIFORNIA.

Letters Patent No. 99,973, dated February 15, 1870.

IMPROVEMENT IN BUILDINGS.

J. Touaillon,

Building.

No. 99,973. Patented Feb. 15. 1870.

Fig. 1

Fig. 2

Fig. 3

Fig. 4

Witnesses

David R. Smith

E. Mc Questen

Inventor

Jules Touaillon

By his Atty's M. M. Smith

Figure 2.4. Patent of Jules Touaillon entitled "Improvement in Buildings", 1870

The behavior of the single CSS bearing was described originally by [Zayas et al. 1987] which original work is here summarized to introduce and explain preliminary concepts relevant to this study. When applied horizontal forces exceed the friction force, sliding initiates and the free body diagram of Figure 2.5a applies.

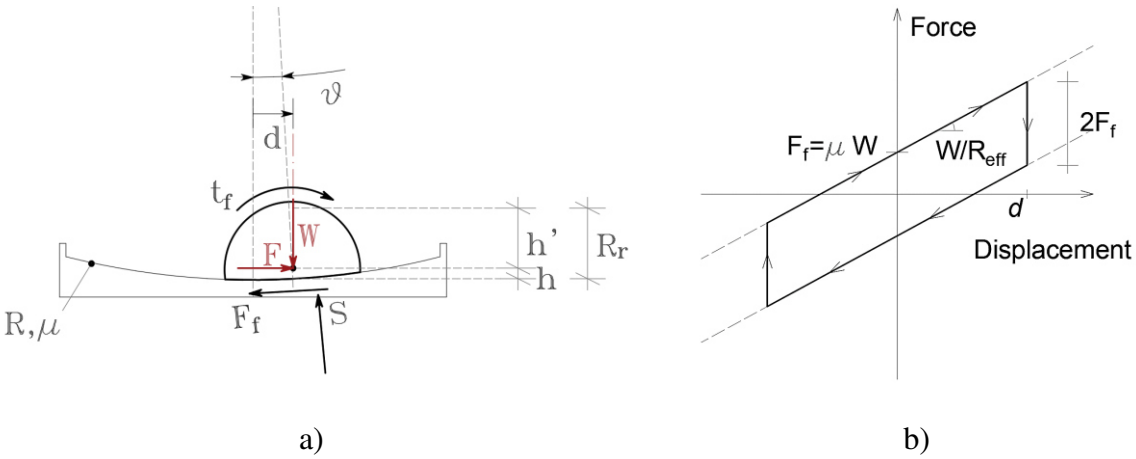

a) b)

Figure 2.5. Single CSS Bearing a) Free Body Diagram of the slider in the deformed configuration, b) hysteretic behaviour.

For a Single CSS the curved sliding surface provides the re-centring force and the energy dissipation, while the secondary sliding surface and the slider accommodate the differential movements and rotations. The equations describing the behaviour of a single CSS bearing with radius of curvature R can be derived from simple equilibrium considerations on Figure 2.5.

In this condition, the forces acting on the slider are:

a) The vertical load, W , acting at the pivot point.

b) The horizontal force, F , transferred through the bearing.

c) The resultant friction force, $F_f = \mu W$, acting along the sliding interface. The friction coefficient μ varies as a function of several factors including sliding velocity and axial load [Mokha et al., 1990]. For dynamic analysis, the equilibrium equations can be used in the form here presented, thus implementing a friction coefficient that updates at each

time step as a function of the instantaneous sliding velocity $\mu(\dot{d})$. It has to be noticed how the use of a constant friction coefficient value is a simplification based on Coulomb model [Mostaghel Davis 1997] and not a limitation for presented formulations.

d) The resultant force of normal pressure acting along the sliding interface, S. This reaction is off-centred in order to satisfy moment equilibrium, resulting in a not uniform pressure distribution on the sliding interface.

e) The sliding movement generates friction traction tensions along the spherical surface of the articulated slider, f_t. Their effect, anyways, is assumed to be part of the friction force, F_f, and they are not explicitly represented in the equilibrium equations [Fenz and Constantinou, 2008].

Considering horizontal and vertical equilibrium equations (Figure 2.5):

$$\begin{cases} F - S \cdot \sin\theta - F_f \cdot \cos\theta = 0 & (a) \\ W - S \cdot \cos\theta + F_f \cdot \sin\theta = 0 & (b) \end{cases} \quad (1)$$

From simple geometric considerations, the displacement d is expressed as follows:

$$d = (R - h)\sin\theta = R_{eff}\sin\theta \quad (2)$$

Where $R_{eff}$is the effective radius representing the distance between the centre of the Concave Plate (CP) (Figure 2.1), and the pivot point of the slider. Combining the exposed equation, the generic force-displacement relationship that governs motion for the Single CSS bearing is found:

$$F = \frac{F_f}{\cos\theta} + \frac{W}{R_{eff}\cos\theta}d \quad (3)$$

In the vast majority of applications, the curvature radius R is far larger than the horizontal displacement d so that $\cos\theta \approx 1$, when these simplifications are made, Equation (3) can be expressed as shown in Equation (4).

$$F = \mu W + \frac{W}{R_{eff}} d \tag{4}$$

This simplification can only be made when the requirement of $d < 0.30\ R$ is met, providing an error lower than 5%. Equations from (1) to (4) have been originally present by Zayas in [Zayas et al. 1987]. The force-displacement relationship based on Equation (4) is represented in Figure 2.5b. Upon reversal of motion, the Single CSS bearing rigidly unloads by $2F_f$ and slides in the opposite direction preserving the same stiffness of the loading branch (Equation (4)) [Fenz and Constantinou, 2008].

Considering the DCCSS bearing, in order to derive the force vs displacement relationship, the motions of the TCP and BCP are considered separately and then combined to reach the relationship for the complete bearing. It is assumed in this first formulation, that the overall displacement is lower than the geometric displacement capacity. Examining the free body diagram of the slider on the concave surfaces in the deformed configuration shown in Figure 2.6 below, the forces acting on the slider are:

a) The vertical load, W, acting at the pivot point;
b) The lateral force, F, transferred through the BCP to the rigid slider;
c) The friction forces, F_{f1}, F_{f2}, acting along the curved surfaces;
d) The resultant forces of normal pressure acting on the sliding interfaces, S_1, S_2. These must be eccentric in order to satisfy moment equilibrium. Accordingly, the pressure distribution on both sliding interfaces is not uniform, as seen for the Single CSS bearing case.

The analytical description of the particular case of DCCSS bearings characterized by the same radii of curvature $R_1 = R_2 = R$ and same coefficients of friction $\mu_1 = \mu_2 = \mu$ is here exposed. Usual values for the μ coefficient of friction range from 0.02 and 0.15 for PTFE-based material

sliding pads at ambient temperature. Angles ϑ_i are formed by the lines connecting the centre of curvature of the concave plates ("1" for the Bottom Concave Plate (BCP) and "2" for the Top Concave Plate (TCP)) and the central point of the contact area between slider and plate, while angles $\vartheta_{s,i}$ form between the latter of these points and the points of application of the resultant forces at the surface of the slider. As seen for the Single CSS case, angles are considered small so that the normal components of force are equal to the applied load W (see Figure 2.6).

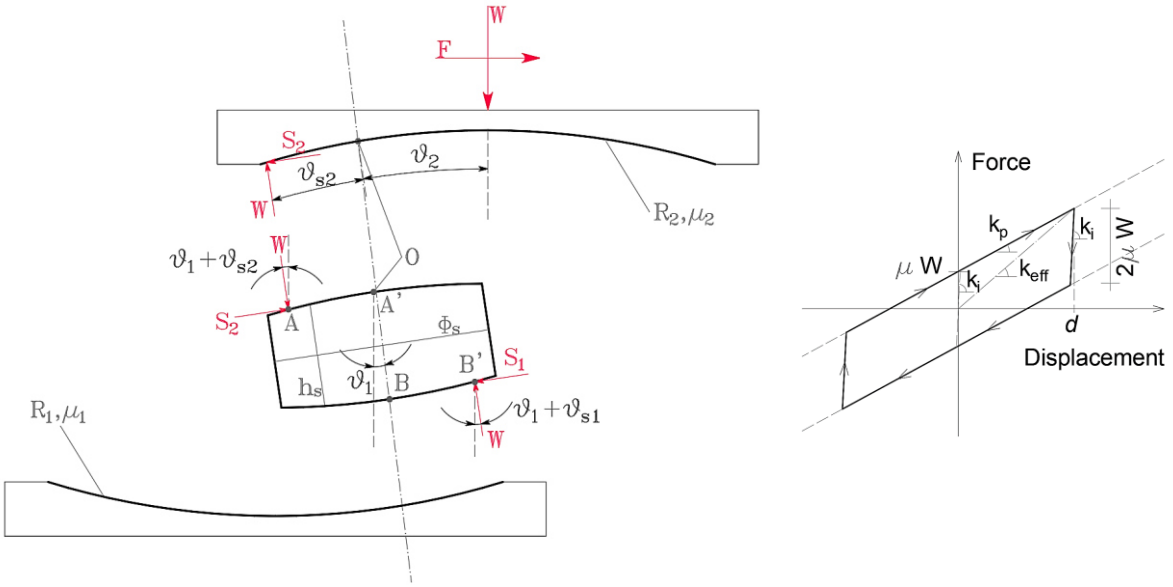

a) b)

Figure 2.6. DCCSS Bearing a) Free Body Diagram of the slider in the deformed configuration, b) hysteretic behaviour.

The resultant force N must be eccentric in order to satisfy moment equilibrium, accordingly the pressure distribution on the sliding interface is not uniform. Equilibrium of force in the horizontal direction (a), equilibrium of moments for the slider around A (b) and horizontal equilibrium of forces for the TCP (c) are here shown:

$$\begin{cases} W\vartheta_{s2} + S_2 = S_1 + W\vartheta_{s1} & (a) \\ W(\vartheta_{s1}R_1 + \vartheta_{s2}R_2) - W\vartheta_{s1}h_s - S_1h_s = 0 & (b) \\ W(\vartheta_1 + \vartheta_{s2}) + S_2 = F & (c) \end{cases} \tag{5}$$

Imposing the constraint on the TCP to be horizontal during the motion, the angles can be represented as:

$$\vartheta_{s1} = \frac{-\mu_1 h_s + R_2(\mu_1 - \mu_2)}{R_1 + R_2 - h_s} \quad (6.\ \text{I})$$

$$\vartheta_{s2} = \frac{\mu_1 R_1 + \mu_2 h_s - \mu_2 R_1}{R_1 + R_2 - h_s} \quad (6.\ \text{II})$$

Considering that the displacement of the TCP is given by $d = (R_1 - h_s)\vartheta_1 + R_2\vartheta_2$, the force-displacement relation of the bearing is:

$$F = \frac{\mu_1 R_1 + \mu_2 R_2}{R_1 + R_2 - h_s} W + \frac{W}{R_1 + R_2 - h_s} d \quad (7)$$

Note that, Equation (7) is valid during sliding on both concave surfaces and that the complete description of the behaviour for a generic DCCSS bearing with any random geometric and mechanical parameters, requires additional considerations [Fenz and Constantinou, 2008] which are here not reported for the sake of brevity. Also note that Equation (7) predicts that the effective radius of the DCCSS bearing is $R_{eff} = R_1 + R_2 - h_s$, which demonstrated that it is identical to that of the Single CSS bearing previously discussed.

The most commonly diffused DCCSS bearing in Europe are characterized by the same radii of curvature $R_1 = R_2 = R$ and same coefficients of friction $\mu_1 = \mu_2 = \mu$. In this particular case, the effective radius can be expressed as $R_{eff} = 2R - h_s$ and Equation (7) is expressed as:

$$F = W\left(2\frac{\mu R}{R_{eff}}\right) + W\frac{d}{R_{eff}} \quad (8)$$

The force vs displacement law of DCCSS devices with rigid slider and identical facing concave plates, is shown in Figure 2.6b. Upon reversal of motion, the bearing unloads by $2\mu W$ with the same initial stiffness k_i characterizing the start of motion, and slides in the opposite direction with the loading and unloading stiffness $k_p = W/R_{eff}$.

The DCCSS isolator can be modelled as a combination in series of two Single CSS and the force-displacement behaviour is equal to that of a Single CSS with same coefficient of friction ($\mu = \mu_1 = \mu_2$) and effective radius of curvature $R_{eff} = R_1 + R_2 - h_s$ [Fenz and Constantinou, 2006].

2.3 Coefficient of Friction

Concave plates are generally characterized by a plan diameter within the range of 100-1000mm, convex plates are coated with polymeric materials having thickness within the range of 5-8mm. The polymeric material more used in the past was the PTFE (*PolyTetraFluoroEthylene*), however, nowadays, the trend is to implement in CSS different materials in order to offer higher resistance to compression loads, different areas of sliding characterized by different friction coefficients and many other technological innovations. The dynamic performance of CSS isolators mainly depends on the frictional properties of the sliding materials. Several studies have shown that the friction coefficient depends on the temperature, axial load and velocity. Many different experimental tests have been performed in recent years in order to properly assess these factors influence on the dynamic performance of CSS sliders [Fenz and Constantinou, 2008b], [Quaglini et al., 2012], [Di Cesare et al., 2019], [Furinghetti et al., 2019], [Furinghetti et al., 2021]. Even though the friction mechanism is very complex, at current state of art, for seismic applications the only influence of sliding velocity and vertical load is generally considered for the design and analysis of isolation systems based on CSS devices [Constantinou et al., 1999], [McVitty and Constantinou, 2015]. These effects influence on the coefficient of friction is here exposed to introduce preliminary concepts further used in this study.

The sliding friction coefficient of steel–PTFE interfaces reduces while increasing the vertical load [Mokha et al., 1990]. This effect has also been confirmed by more recent studies for the steel-PTFE specifically used on CSS devices [Dolce et al., 2005], [Pigouni et al., 2017]. The friction coefficient μ variation law modelled as a function of the vertical load W was introduced by [Bowden and Tabor, 1964] and is currently used for the modelling of CSS isolators. The equation provided by [Bowden and Tabor, 1964] is the following:

$$\mu = a \cdot W^{-b} \tag{9}$$

Where a and b are positive constants determined through friction tests.

One of the most used models describing the friction coefficient μ as a function of the instantaneous sliding velocity v (for a constant vertical load W) has been developed and discussed by [Mokha et al., 1990] and [Constantinou et al., 1990]. The proposed model equation is the following:

$$\mu(v) = \mu_{HV} - (\mu_{HV} - \mu_{LV}) \cdot e^{-a_1|v|} \tag{10}$$

Where μ_{LV} is the friction coefficient at Low Velocities (e.g., $v < 5mm/s$), μ_{HV} refers to High Velocities (e.g., $v > 100mm/s$), v is the instantaneous velocity and a_1 is a parameter governing the transition between the Low and High velocity phases.

The friction coefficient laws of variation reported in Equations (9) and (10) are both implemented in current modelling and analyses to have an accurate description of CSS dynamic behaviour.

3 Over-Stroke regime

As discussed before CSS bearing are widely used worldwide. Aside from all the made characterization, CSS devices can be further divided in two main groups: devices with or without a displacement restrainer. Displacement restrainers are element which prevent the inner slider to slid past a certain point which usually is the perimeter of the housing pad. These elements can be for example displacement restraining rings, as shown in Figure 3.1a, which are made of the same material of the housing plate and can be welded, bolted to it or even form a single block with the pad itself [Bao et al., 2018a]. Retaining elements are widely used in America in order to control displacements and to avoid the isolator disassembly when displacements higher than the design ones occur. Anyways, the impact against such retaining elements may induce significantly high acceleration onto the superstructure. On the contrary, the European Standards do not allow the presence of restraining element and only approves the use of structural joints separating the superstructure from the surrounding constructions, in order to safely accommodate the seismic movement. When displacement restraining elements are not employed, and concave plates feature a flat rim [Bao et al., 2018a] (Figure 3.1b), the inner slider movement beyond the geometric capacity displacement d_c of the isolator is allowed entering in the so-called Over-Stroke displacement regime [Di Cesare et al., 2019], [Ponzo et al., 2020], [Di Cesare et al., 2021], [Ponzo et al., 2021], [Furinghetti et al., 2021]. When the slider runs in the Over-Stroke displacement regime it is capable of providing the CSS device with an increased displacement capacity and sliding force. The equations of motion and the limit displacements for the over-stroke sliding regime have still not been characterized but a proper argumentation is needed in order to provide designers with the accurate displacement capacities and forces of CSS isolators. The following sections of the present dissertation are focused on the analysis of the over-stroke regime for DCCSS devices with rigid slider and same radii of curvature and friction coefficients on both concave plates ($R_1 = R_2,\ \mu_1 = \mu_2$), in terms

of modelling, influence on superstructure and algebraic solution on the basis of ad-hoc laboratory tests.

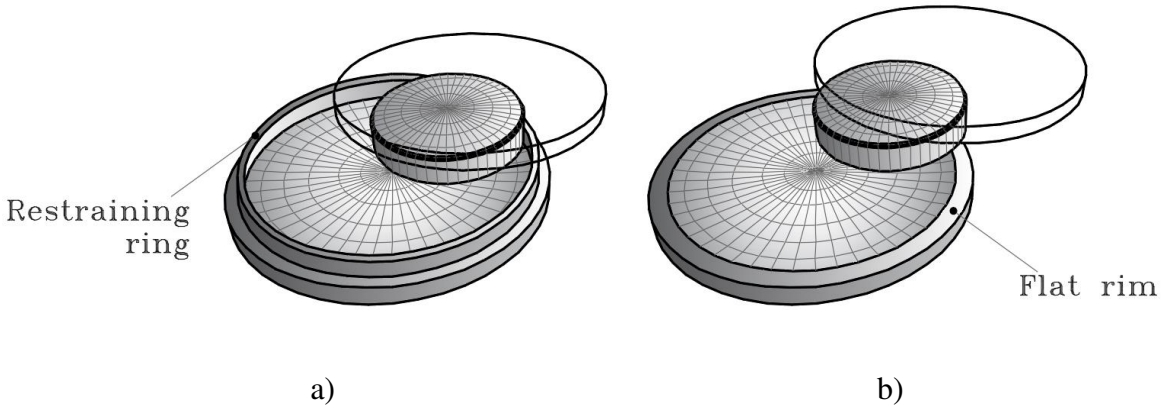

Figure 3.1. DCCSS bearing in deformed condition a) with a restraining ring and b) with a flat rim.

3.1 Experimental tests

Controlled displacement tests on DCCSS bearing without restraining rings are currently underway in Italy in order to investigate the actual device response when the sliding displacement exceeds the geometric displacement capacity d_c and runs over the sliding surfaces border. The results of a preliminary test [Di Cesare et al., 2019] on one device conducted by [https://www.fipmec.it/] are presented here below.

The tested DCCSS bearing is designed to accommodate a nominal displacement at CLS $d_2 = \pm 100\ mm$ while the actual geometric displacement capacity is $d_c = 2\,u = \pm\,136\ mm$ (Figure 3.2). The vertical load used in the test is $W = 2500\ kN$, which corresponds to the design quasi-permanent load. The effective radius of curvature is $R_{eff} = 2500\ mm$. The diameter of the rigid slider is $\Phi_s = 310\ mm$ and the external diameter of the concave plates is $d_{ext} = 446\ mm$. The main characteristics of the DCCSS specimen are reported in Table 3.1. The sliding material utilized in the primary sliding surfaces is an Ultra High Molecular Weight Poly-

Ethylene (UHMW-PE) characterized by exceptional properties in terms of load bearing capability, wear resistance, as well as stability and durability [https://www.fipmec.it/].

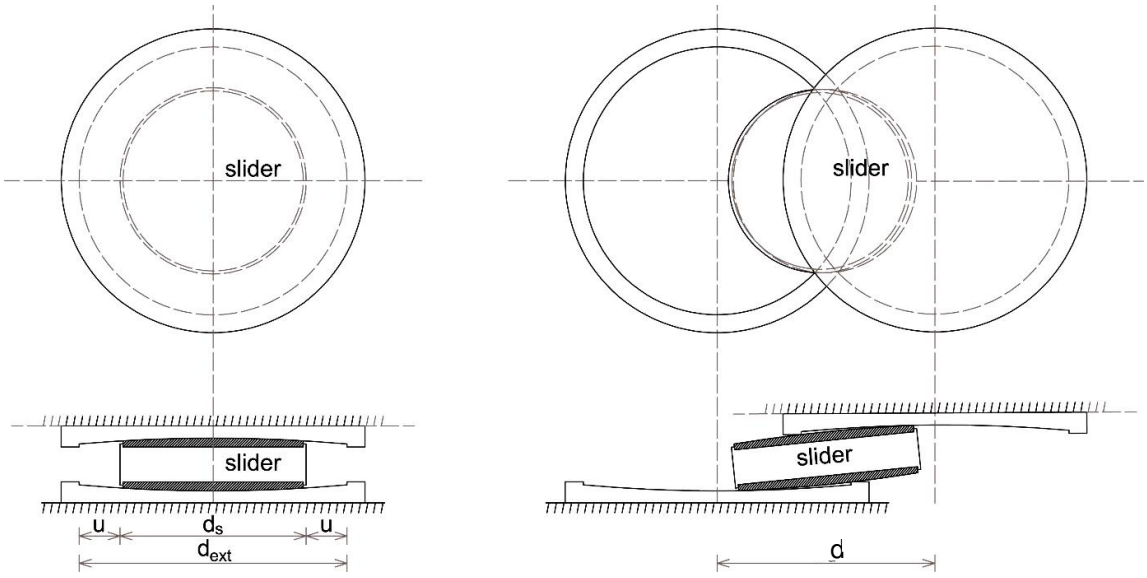

a) b)

Figure 3.2. Plan and cross section views of a Double Concave Curved Surface Slider in a) static and b) over-stroke regime.

Table 3.1 DCCSS specimen parameters.

Sliding Material	d_2	$K_{eff}(d_2)$	R_{eff}	k_p	W	μ	k_i	d_{ext}	Φ_s	d_C
	[mm]	[kN/mm]	[mm]	[kN/mm]	[kN]	[–]	[kN/mm]	[mm]	[mm]	[mm]
UHMW-PE	±100	2.00	2500	1.00	2500	0.04	157.50	446	310	±136

The testing protocol consisted of one full cycle at constant velocity $v = 2.5\, mm/sec$ and constant vertical load (Figure 3.3). A controlled displacement was applied reaching an over-stroke displacement value equal to the geometric displacement capacity d_c plus a quarter of the sliding pad diameter ($d^+ = dc + \Phi_s/4 \approx 215\, mm$) in one direction and half of the sliding pad ($d^- = -\, d_c - \Phi_s/2 \approx -\, 290\, mm$) in the opposite one.

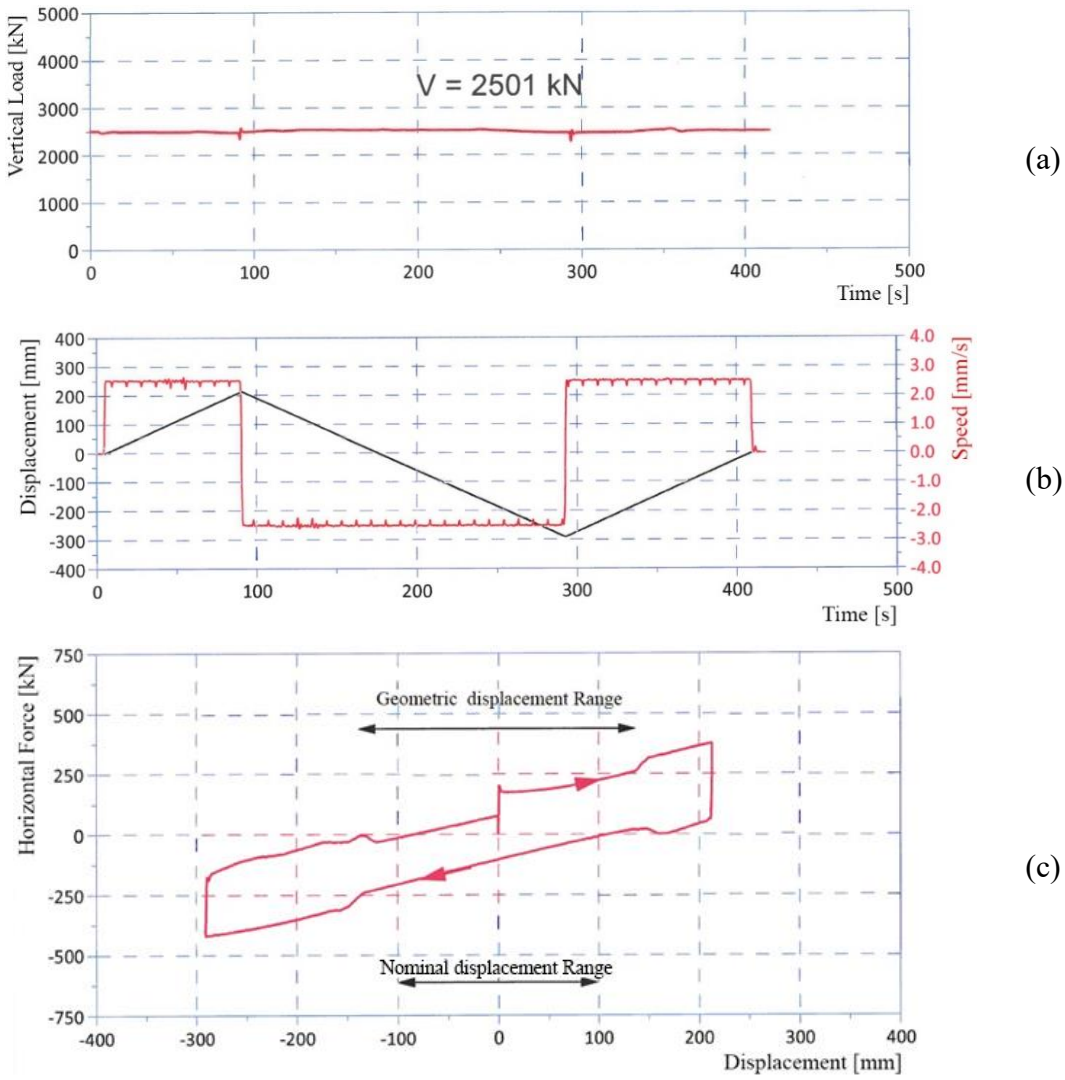

Figure 3.3. (a) Vertical Load – Time, (b) Displacement/ Speed – Time, (c) Horizontal Force – Displacement results obtained from FIP MEC srl test.

Experimental results showed that at the first cycle the load-bearing capacity of the device is not compromised until the slider overcomes the concave surfaces edge up to a quarter or half of its diameter, resulting in a slight increase of friction coefficient ($\mu_2 = \mu + \Delta\mu$). The test outcome showed a breakaway friction condition in the first loading branch due to the very slow velocity applied during the test in order to grant the testing apparatus full control and avoid vertical loading instability. Both in loading and unloading phases, the DCCSS over-stroke cyclic behaviour was characterized by a "sloping dog bone" shape, preserving the re-centring capability and the ability to support gravity loads.

A recent experimental campaign has been perfomed by [Furinghetti et al. 2021]. A total number of three devices whose characteristics are summarized in Table 3.2 has been considered. The testing protocol adopted is the same, consisting of one cycle at constant velocity $v = 2.5\,mm/sec$ and an average constant pressure $\sigma_{test} = 45\,MPa$ (Table 3.2), performed applying a "triangular-shaped" controlled displacement. In these cases, as well as in the case shown in Figure 3.3, the very low velocity of the test determined a Breakaway friction condition which has been shown in Figure 3.4 with a red dashed line.

Table 3.2 Summary of DCCSSs' specimen characteristics.

Specimen	Sliding Material	R_{eff} [mm]	μ [-]	Φ_s [mm]	d_c [mm]	v [mm/s]	σ_{test} [MPa]	d_{test}/d_c [-]
a	Graded PTFE filled with carbon fibres	3080	0.05	260	±275	2.5	45	≈ 1.5
b	Ultra low-density Polyethylen	3080	0.03	260	±275	2.5	45	≈ 1.5
c	Virgin PTFE	3080	0.01	260	±275	2.5	45	≈ 1.5

DCCSS specimens are characterized by an effective radius of curvature of $R_{eff} = 3080mm$, a slider diameter of $\Phi_s = 260mm$ and a geometric capacity displacement of $d_c = \pm 275mm$. The ratio between the maximum displacement reached during the tests and the geometric capacity displacement is $d_{test}/d_c \approx 1.5$. The experimental results show that in the over-stroke regime, the friction coefficient increases of $\Delta\mu = 0.015$ for all tests [https://www.fipmec.it/] and [Furinghetti et al., 2021] and that the load-bearing capacity of the device is not compromised during the sliding in the over-stroke displacements regime. The test displacement history and the force vs displacement cycles for each specimen are shown in Figure 3.4.

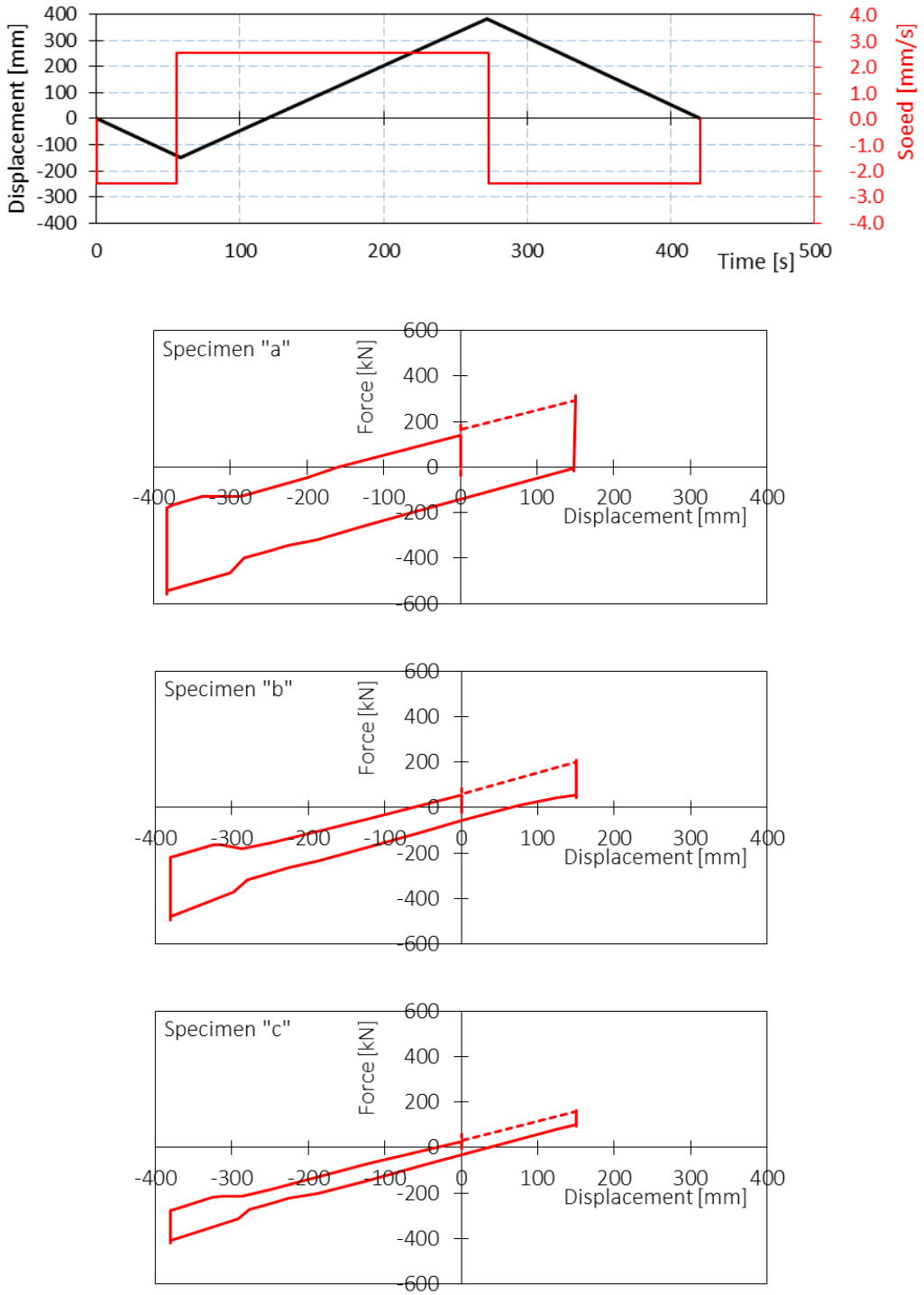

Figure 3.4. Displacement and Speed vs Time and Force vs Displacement results obtained from tests.

3.2 Modelling

The chosen environment for modelling and performing numerical analyses is the OpenSEES Framework [McKenna et al., 2000]. OpenSEES provides professionals with a wide predefined

library in order to allow the representation of the most majority of structural and non-structural elements and behaviours. For CSSs, OpenSEES provides a basic element named *singleFPBearing* which is composed by two nodes, a bottom (*i-node*) and a top node (*j-node*) as shown in Figure 3.5. The *i-node* is fixed in order to represent the BCP of a CSS device or the whole substructure, while the *j-node* is connected to the base grid of beams layer above the isolation system, or, in more simplified models, is free and bears the vertical load W acting on the device and the horizontal forces F. The two nodes are connected with rigid elements and a *Zero-Length* sliding hinge. The two nodes can be either positioned to be at a distance corresponding to the isolator height or to model a *Zero-Length* element.

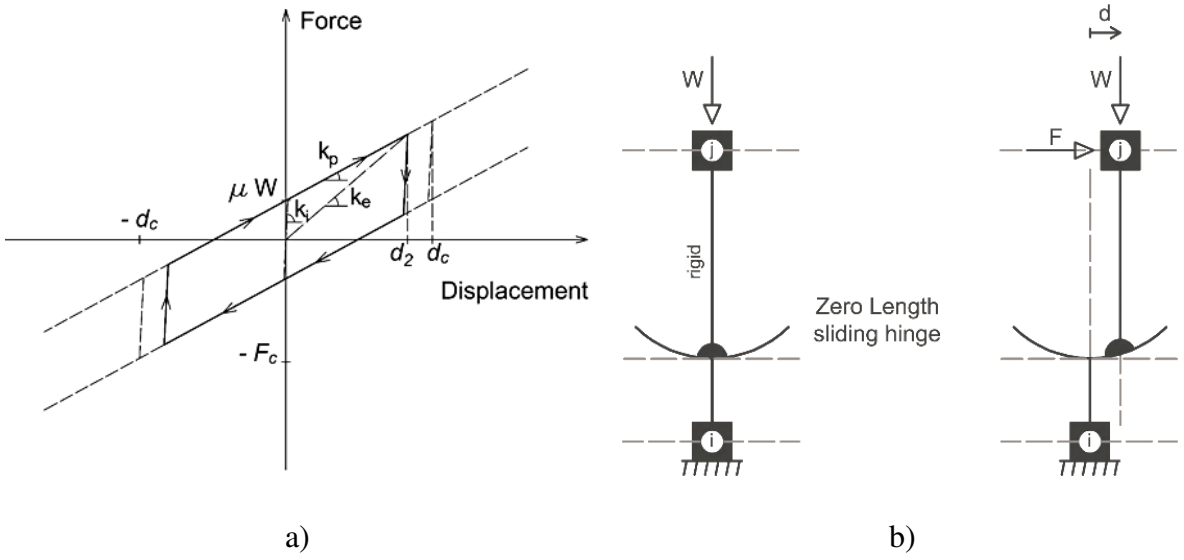

a) b)

Figure 3.5. SingleFPBearing a) Force vs Displacement relationship and b) Spring model representation.

In order to simulate the DCCSS behaviour during the over-stroke displacement the basic *SingleFPBearing* (Figure 3.5) has been modified by adding three zero length parallel elements from the top *j-node* to a new fixed *k-node*, as shown in Figure 3.6a. Two of these three zero length parallel elements have been modelled as elastic-perfectly plastic gap elements (*elasticPPGap*) defined by a gap displacement d_c, an elastic stiffness $E = 2\,k_2$ where $k_2 = 2.50\ kN/mm$ is a secondary stiffness implemented to represent the friction coefficient increase

$\Delta\mu = 0.015$, and a yielding force $F_y = 2\,\Delta\mu \cdot W$ (Figure 3.6b) and no hardening ratio or damage accumulation are considered so the gap material can re-center on load reversal. The last zero length element has been provided with a multi-linear elastic material (*elasticMultiLinear*), characterized by a nonlinear elastic behaviour without energy dissipation, defined by a set of stress-strain points as shown in Figure 3.6b. Force vs Displacement relationships for all of the materials shown in Figure 3.6b and implemented in the model report d_{lim} limit displacement considered for the device.

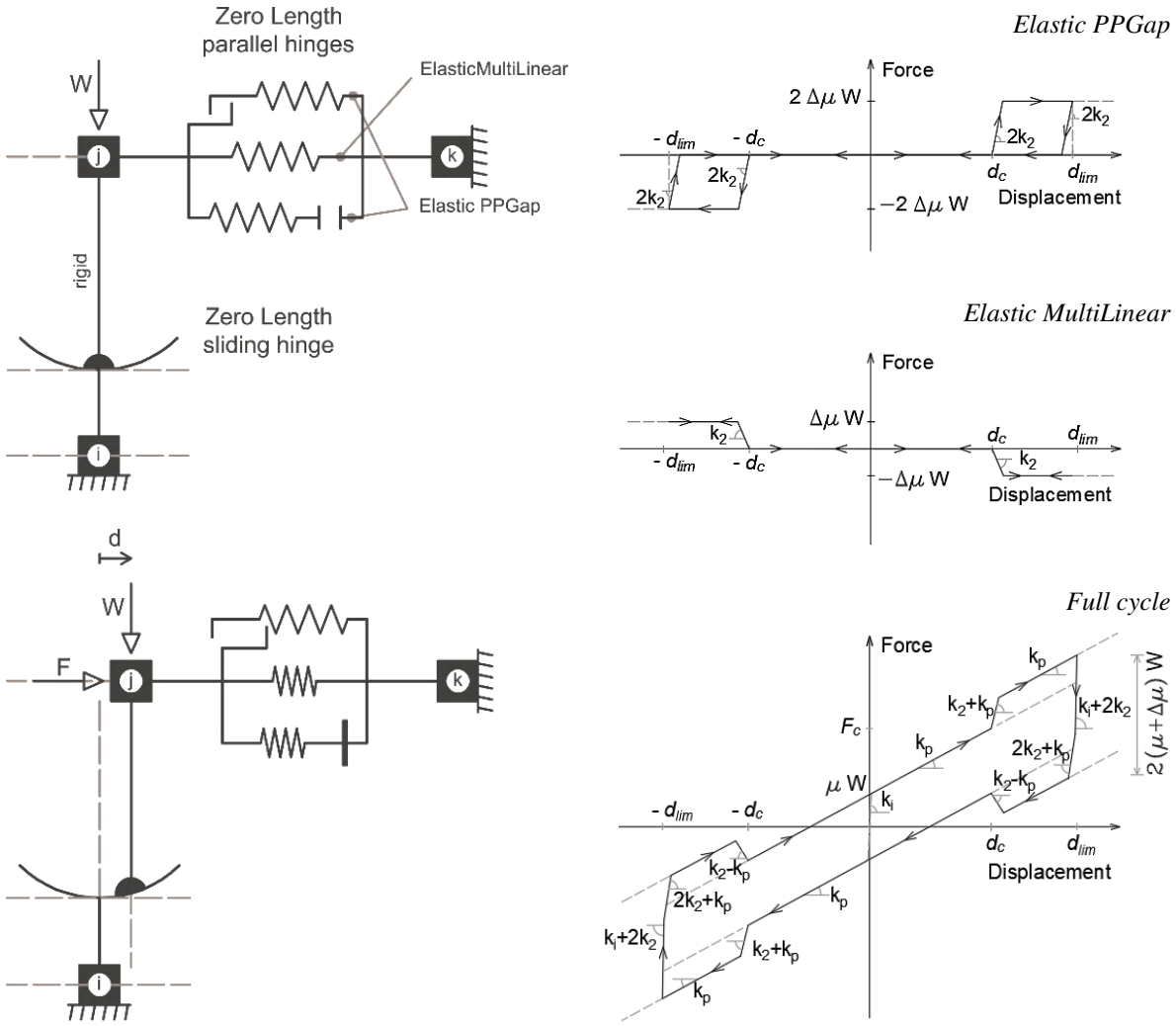

a) b)

Figure 3.6. Modified SingleFPBearing a) Spring model representation and b) force vs displacement relationships.

Anyways it has to be noticed how the numerical model does not implement the DCCSS failure, and the analysis keeps running for displacements even higher than d_{lim} (dashed lines).

Once the OpenSEES modified *SingleFPBearing* parameters have been calibrated on the basis of the experimental outcome, numerical simulations obtained from a single element featuring the modified model have been performed. The comparison between numerical and experimental results shown from Figure 3.7 to Figure 3.10, highlights how the modified model captures the DCCSS experimental cyclic behaviour in the over-stroke regime reasonably well.

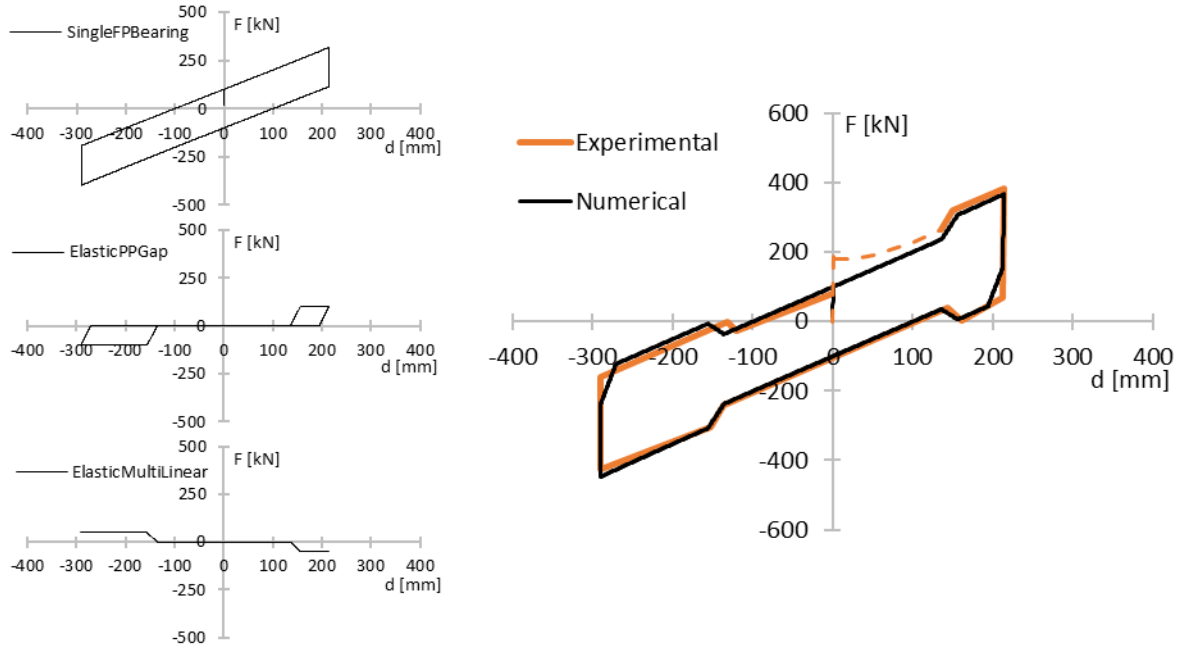

Figure 3.7. FIP [https://www.fipmec.it/] specimen Force vs Displacement relationships for single and composed elements recorded during the numerical simulation.

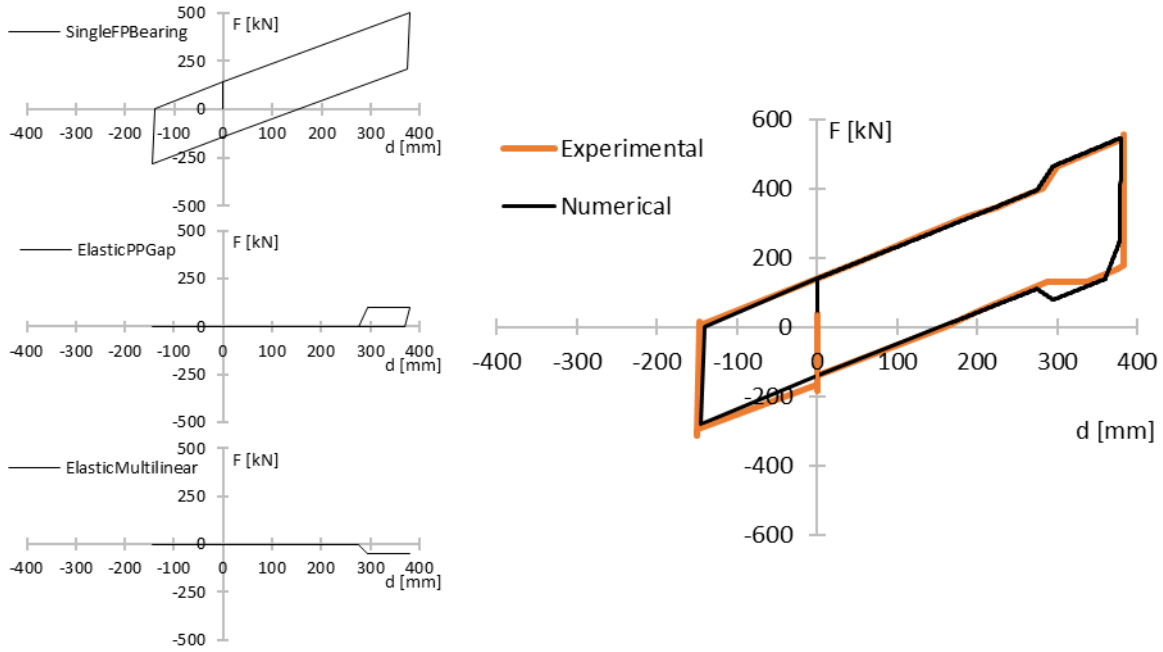

Figure 3.8. "a" specimen [Furinghetti et al.,2021] Force vs Displacement relationships for single and composed elements recorded during the numerical simulation.

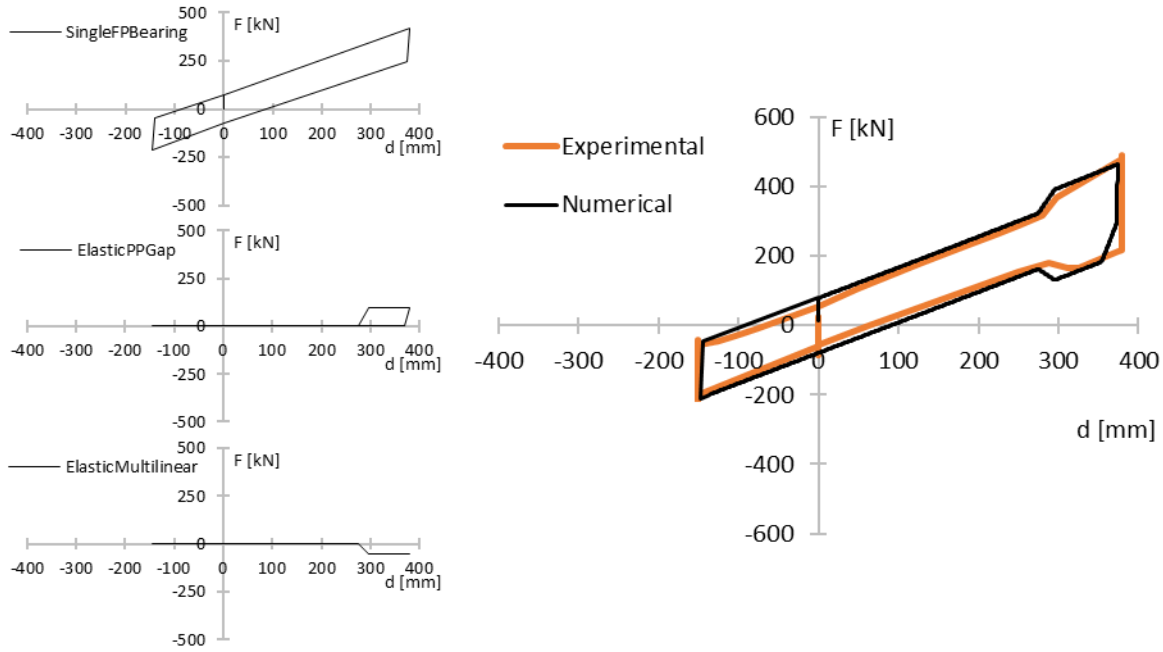

Figure 3.9. "b" specimen [Furinghetti et al.,2021] Force vs Displacement relationships for single and composed elements recorded during the numerical simulation.

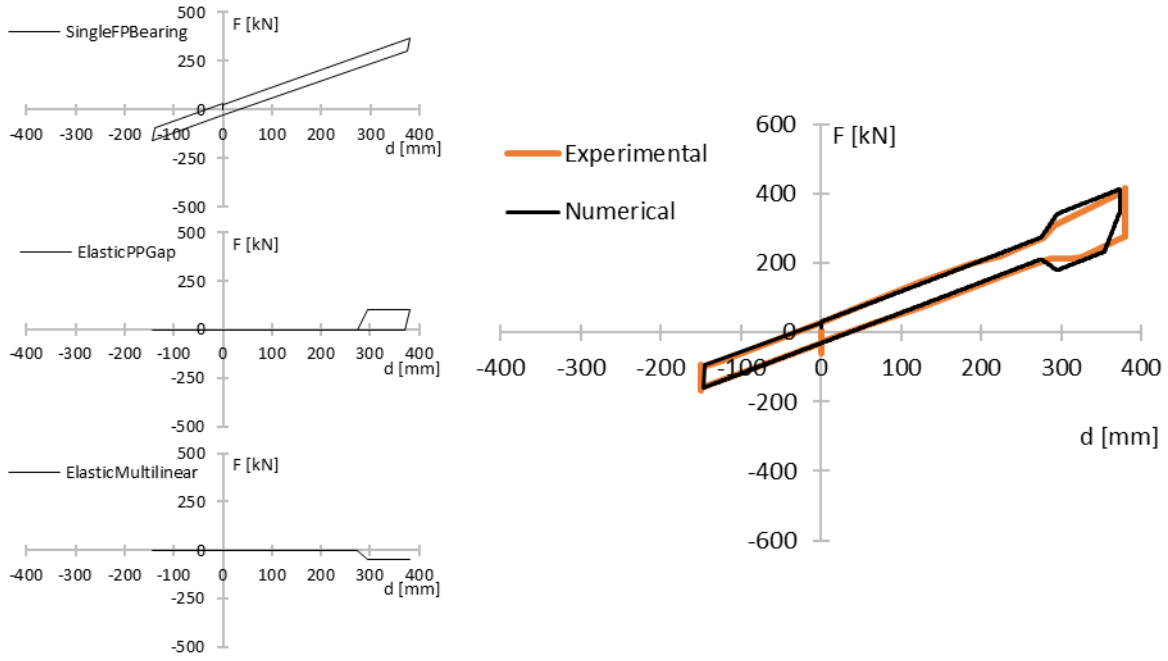

Figure 3.10. "c" specimen [Furinghetti et al.,2021] Force vs Displacement relationships for single and composed elements recorded during the numerical simulation.

3.3 Displacement retaining elements

For rigid rim bearings [Bao and Becker, 2018], the use of end-stroke restraints (end stops) such as restraining rings showed in Figure 3.1a and in Figure 3.11a is admitted by American standards [ASCE/SEI 7-10, 2013] [ASCE, A. 2010]. On the contrary, the European Standard [UNI EN 15129 (2009)] does not allow for any restraining ring or other mechanical element that serves as end-stroke and that can be damaged in case of a seismic event larger than the Maximum Considered Earthquake (MCE) (corresponding to the Italian code CLS). However, the European Standard allows the use of ground retaining walls, see Figure 3.11b, or specific devices such as rubber bumpers attached to the walls, to be used as over-stroke displacement restrainer (end-over-stroke). Usually in Europe, the gap separating the superstructure from the retaining wall is much larger than the displacement capacity of the isolators, and consequently, the inner slider can run on the edge of the sliding surfaces in the over-stroke regime for

earthquakes producing displacement larger than the isolators geometric displacement capacity d_c, but still preserving the ability to support gravity loads and the re-centring capability.

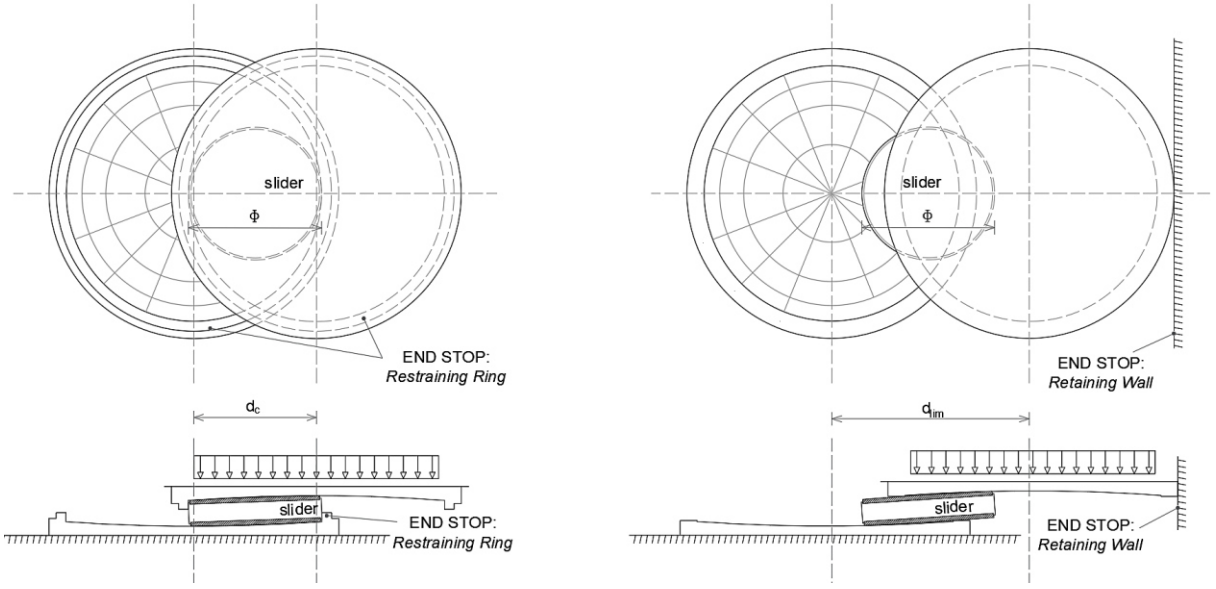

a) b)

Figure 3.11. Maximum lateral displacement of DCCSS Isolators: a) with restraining ring d_c; b) with overstroke capacity and retaining wall $d_{lim} \geq d_c$, in plan and cross-section view.

Retaining elements impact has not been widely observed and studied in the past, except for the studies of [Masroor and Mosqueda, 2013] and [Bao et al., 2018a]. In [Masroor and Mosqueda, 2013] an impact element considering moat wall flexibility is proposed based on theoretical observations and experimental simulations to better understand the consequences on the superstructure of the impact. In [Bao et al., 2018a] an extended experimental campaign to investigate the extreme behaviour of DCCSS bearings under strong ground motions was conducted, considering scaled bearings with four different types of restraining elements representing typical devices found in Europe, Japan, and the United States.

Other retaining elements such as Shape Memory Alloy (SMA) devices combined with DCCSS have been studied by De Domenico, Gandelli and Quaglini in 2020 [De Domenico et al., 2020a]

[De Domenico et al., 2020b]. Parametric studies on this combined system reveal how SMA devices are suitable to limit the maximum displacement under high-intensity earthquakes, also providing good energy dissipation and a high re-centring capability.

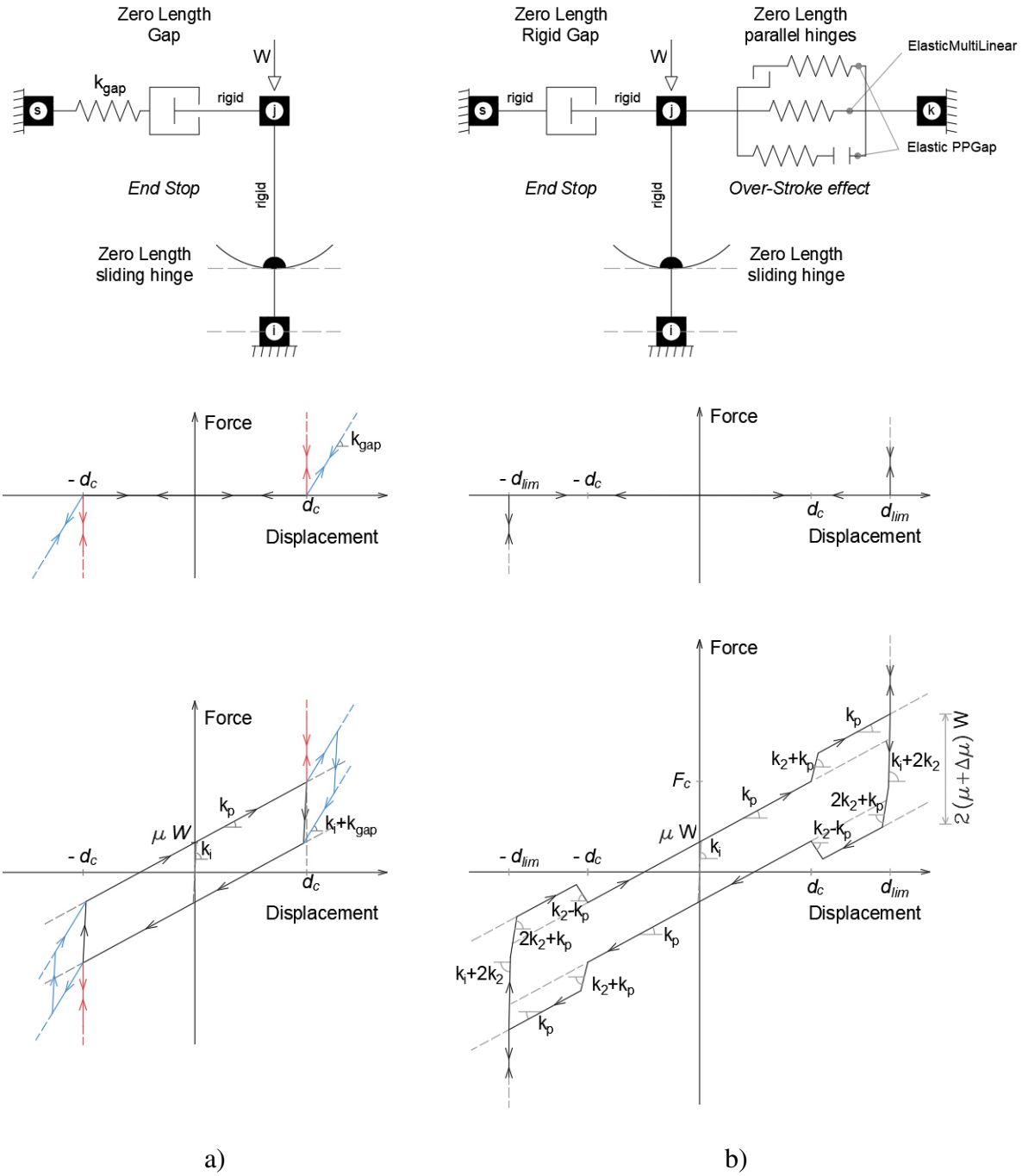

Figure 3.12. Spring model representation of the Modified SingleFPBearing with End-Stop and force vs displacement relationships for a) the restraining ring and b) the retaining wall models.

In the present study, for the purpose of analyzing the superstructural response of DCCSS base isolated structures when retaining elements are employed, specific analyses have been performed considering "end-stops". The failure condition of these restraining elements, anyway, has not been taken into account, modelling them as infinitely rigid or infinitely flexible elements. For the OpenSEES model, the *SingleFPBearing* described in Figure 3.5 and the *Modified SingleFPBearing* described in Figure 3.6, have been provided with an additional zero-length hinge element featuring an *elasticPPGap* material, connected to a fixed *s-node* as shown in Figure 3.12. For restraining rings modelling, the new hinge *elasticPPGap* material has been implemented on the *SingleFPBearing* model and characterized with different levels of stiffness k_{gap}, ranging from infinite to a certain percentage of the superstructural horizontal stiffness starting from a gap displacement of d_c as shown in Figure 3.12c. For retaining walls modelling, *Modified SingleFPBearing* has been provided with the *elasticPPGap* hinge modelled in the only configuration of unlimited strength material starting from a gap displacement of d_{lim} as shown in Figure 3.12b.

3.4 Models Summary

In Table 3.3 a summary of adopted models and their labels using in the body of the present doctoral dissertation is given.

Table 3.3 Summary of DCCSS numerical models adopted throughout the study.

Numerical model Label	*Spring representation*	*Force vs Displacement relationship*
SingleFPBearing	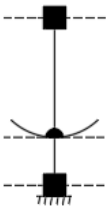	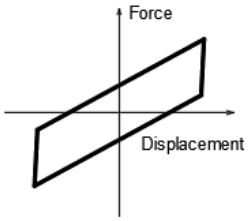
OS_DCCSS	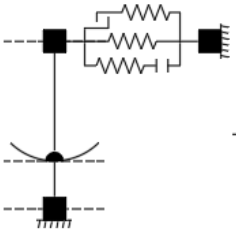	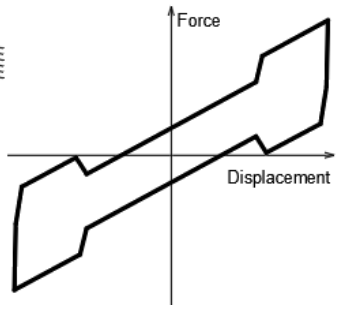
Ring_DCCSS	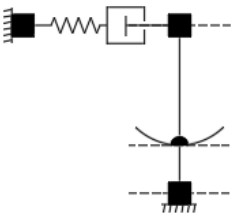	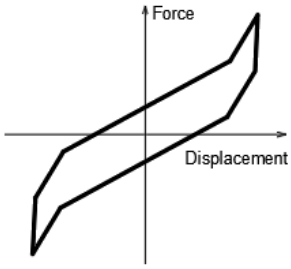
Wall_DCCSS	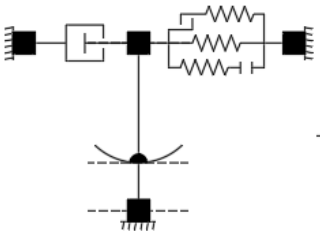	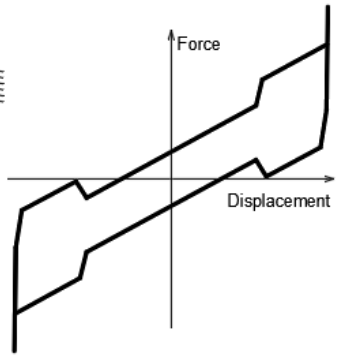

4 Seismic risk probabilistic assessment

In the following sections many different structural systems have been analysed using Nonlinear Time History Analysis (NTHA) and Multi-Stripes Analysis (MSA) methods using different sets of real ground motion recordings. Given the uncertainty of seismic events, results from these analyses needed to be organized in probabilistic distributions with consolidated methods such as the one proposed by Cornell and Krawinkler and Douglas [Cornell and Krawinkler, 2000], [Douglas, 2017] providing the average annual frequency of occurrence of an event:

$$\iiint P(X|DM) \cdot |dP(DM|EDP)| \cdot |dP(EDP|IM)| \cdot |dH(IM)| \tag{11}$$

Where:

- $P(X|DM)$ is the probability of a certain parameter X to reach a certain Damage Measure (DM) limit;
- $P(DM|EDP)$ is the term representing the seismic fragility and the probability of the Damage Measure (DM) to reach the Engineering Demand Parameter (EDP) limit for different seismic Intensity Measures (IM);
- $P(EDP|IM)$ is the probability that events, with an IM high enough to reach the EDP limit, occur;
- $H(IM)$ is the seismic Hazard (H) linked to a certain IM.

The just presented Equation (11) has been formulated considering seismic events modelled as homogeneous Poisson-arrival events.

In the hazard analysis, the seismic environment is considered (nearby faults, their magnitude-frequency recurrence rates, mechanism, site distance, site conditions, etc.) and the seismic hazard is estimated on the considered construction site considering its structural, architectural and other design characteristics. The hazard curve describes the annual frequency with which

seismic actions are estimated to exceed certain levels. Seismic actions are parameterized employing intensity measure IM.

Seismic risk can be considered as the probability to underway a certain economic loss in a given site during a given time lapse. Seismic Risk depends on the seismic hazard, on the structural vulnerability and on the exposition level (structures, people, activities and services subjected to the seismic threat). The evaluation of all of these factors is complex so the preferred approach considers Seismic Risk as only depending on the seismic Hazard and on the structural vulnerability, so that the simplified PEER equation is:

$$\int P(X|DM) \cdot |dH(IM)| \tag{12}$$

Once Limit States (LS) have been defined, the damage is computed employing the density of probability function:

$$\int_{IM\ i}^{IM\ n} P(D > d_{LS}|IM) \cdot \left|\frac{dH(IM)}{dIM}\right| dIM \tag{13}$$

Where:

- $P(D > d_{LS}|IM)$ represents the fragility curve for a certain Limit State;
- $H(IM)$ is the seismic Hazard (H) linked to a certain IM.

If IM is a discrete variable with a finite range of values, the integral function presented in Equation (13) can be expressed as in the following Equation (14):

$$\sum_{IM_i} P(D > d_{SL}|IM) \cdot |\Delta H(IM)| \tag{14}$$

4.1 Hazard Function

The seismic hazard is represented employing the Hazard Curves, usually traced on a plane that sees as the y-axis the *Mean Annual Frequency* associated to the probability of a certain seismic acceleration to occur, and as the x-axis the spectral accelerations S_a. Hazard curves are derived from Probabilistic Seismic Hazard Analysis (PSHA) which provides an explicit prediction of future seismic events for a certain site. The annual probability of exceedance λ allows to assign a certain hazard level to a site. The analytical expression of the annual probability of exceedance λ has been provided by Cornell in [Cornell, 1968] and is reported in Equation (15):

$$\lambda(\mathrm{A} \geq \mathrm{A}_0) = \sum_{i=1}^{N_s} v_i \iint f_{Mi}(m)\, f_{Ri}(r)\, P[A(m,r) \geq A_0 | m, r]\, dm\, dr \tag{15}$$

where:

- v_i is a coefficient used as activity rate, employing the average rate of occurrence of seismic events for a single seismic source i among all possible seismic sources N_s.
- $f_{Mi}(m)$ is the density of probability of the seismic magnitude m and describes the probability of occurrence of a certain seismic event;
- $f_{Ri}(r)$ is the probability density linked to the distance r of the event epicentre from the site;
- $P[A(m,r) \geq A_0 | m, r]$ is the probability of exceeding the threshold value A_0 when an event with magnitude m occurs at a distance r from the site;

The $f_{Mi}(m)$ function follows the Gutenberg-Richter law [Gunteberg and Richter, 1944] represented by the Equation (15):

$$N(m) = 10^{\alpha - bm} = e^{\alpha - \beta m} \tag{16}$$

where:

- $N(m)$ is the number of events reaching the m magnitude;

- a and b are constants depending on the empirical relationships $\alpha = 2.303 \cdot a$ and $\beta = 2.303 \cdot b$;

The proposed Equation (15) anyways is not effective for high seismic intensity levels because historical events cover a short time span when compared to their high return periods. In order to determine the collapse probability for structure characterized by a high fundamental period $T \leq 4s$, the attenuation law proposed by Akkar and Bommer [Akkar and Bommer, 2010] is employed. The attenuation law is reported in Equation (17) and provides the mean acceleration value for a certain site and a given magnitude:

$$\log(y) = b_1 + b_2 M + b_3 M^2 + (b_4 + b_5 M) log \sqrt{R_{jb}^2 + b_6^2} + b_7 S_s + b_8 S_A + b_9 F_N + b_{10} F_R \quad (17)$$

where:

- y is the mean acceleration value expressed in $[cm/s^2]$;
- $b_{1,\dots,i,\dots,10}$ are experimental coefficients depending on the period T;
- $\begin{cases} S_S = 1, \ S_A = 0 & soft\ soil \\ S_S = 0, \ S_A = 1 & hard\ soil \\ S_S = 0, \ S_A = 0 & rock \end{cases}$;
- $\begin{cases} F_N = 1, \ F_R = 0 & Normal\ Fault \\ F_N = 0, \ F_R = 0 & Transcurrent\ Fault \\ F_N = 1, \ F_R = 0 & Inverted\ Fault \end{cases}$;

4.2 Fragility Function

In current practice, a construction vulnerability can be estimated through fragility curves methodology. Fragility curves are statistical-derivation diagrams associating to a given seismic IM, a probability of exceeding a certain Limit State. The best consolidated methodology for building fragility curves has been presented by [Spence and Le Brun, 2006] and [Baker, 2015]. The proposed methodology consists in characterizing each fragility curve using two parameters:

θ the media value and β the standard deviation. The lognormal cumulative distribution function often used to define a fragility function is provided by Equation (18):

$$P(f|IM = x) = \Phi\left(\frac{ln(x/\theta)}{\beta}\right) \quad (18)$$

where:

a) $P(f \mid IM = x)$ is the probability that a ground motion with $IM = x$ will cause the model to reach an EDP limit value (failure f);
b) $\Phi(\,)$ is the standard normal cumulative distribution function (CDF);
c) θ is the median of the fragility function (the IM level with 50% probability of exceeding);
d) β is the standard deviation of $\ln IM$ (sometimes referred to as the dispersion of IM) [Baker et al., 2005], [Baker 2015] and [Castaldo and Alfano, 2019].

The theory proposed by [Spence and Le Brun 2006] and then confirmed by many experimental studies ([Porter et al., 2007], [Bradley and Dhakal, 2008], [Ghafory-Ashtiany et al., 2011], [Eads et al., 2013]) is based on the simple present Equation (18), anyways, further studies, as the ones carried out by [Baker, 2005] led to more accurate analyses. Median and standard deviation values estimation is strongly influenced by the record-to-record variability so that the chosen fitting methodology is the Maximum Likelihood approach. The Maximum Likelihood approach determines θ and β in order to give the final fragility distribution the maximum probability to interpolate the punctual experimental data. This approach is often used because of being:

a) Impartial: not depending on single subjective observations;
b) Effective: being characterized by a very small error;
c) Consistent: in fact, when the number of punctual experimental observations grows larger, the fragility curve tends to converge to real parameters with a smaller error.

Every seismic intensity level $IM = x_j$ is associated with a certain "number of failures", or number of exceeding events for each limit state. Every experimental observation is independent from the others, so that the probability p_j to observe a number z_j of exceeding events out of n_j analyses cis expressed by the binomial distribution of Equation (19).

$$P(z_j failures\ out\ of\ n_j\ EQ) = \binom{n_j}{z_j} p_j^{z_j} \cdot (1 - p_j)^{n_j - z_j} \tag{19}$$

Once experimental results have been obtained from analyses, the Maximum Likelihood approach consists in computing the product of the binomial distribution presented in Equation (19) for each IM.

$$Likelihood = \prod_{j=1}^{m} \binom{n_j}{z_j} p_j^{z_j} \cdot (1 - p_j)^{n_j - z_j} \tag{20}$$

Where m is the number of IM levels considered. Finally, the fragility function is obtained by maximizing the logarithm of the $Likelihood$ function of Equation (20), as shown in the following Equation (21).

$$\{\hat{\theta}, \hat{\beta}\} = (\arg\max)_{\theta,\beta} \sum_{j=1}^{m} \left\{ \ln \binom{n_j}{z_j} + z_j \ln \left\{ \Phi \left[\frac{1}{\beta} \cdot ln \left(\frac{x_j}{\theta} \right) \right] \right\} + (n_j - z_j) \cdot \ln \left\{ 1 - \Phi \left[\frac{1}{\beta} \cdot ln \left(\frac{x_j}{\theta} \right) \right] \right\} \right\} \tag{21}$$

This formulation is particularly favourable because it does not require a pre-defined number of experimental observations for each IM. This is a useful characteristic for the fragility function computation for cases in which, the maximum seismic intensity level considered within the chosen range, is not characterized by an exceeding probability of 100% ($z_j = n_j$), so that the function is capable of predicting the probabilities of exceeding for IM values out of the considered range.

4.3 Annual Rates of Failure

Once hazard and fragility functions have been determined, Seismic Risk and failure probabilities evaluation is possible. Annual Failure Rates are characterized by the following Equation (22):

$$\lambda_f = \lambda \cdot \int_0^{+\infty} P[\, f \,|\, IM = x \,] \cdot f_{IM}(x) \cdot dx \tag{22}$$

The PSHA analyses carried out in the present study consider IM with a return period up to 100,000 years, meaning that the integral function proposed in Equation (22) cannot be fully computed. Thus, if fragility and hazard functions have been computed up to a certain intensity measure $IM_{T_R^*}$ associated to a certain return period T_R^*, the annual failure rate λ_f expression can be simplified in the following λ^* Equation (23):

$$\lambda^* = \lambda \cdot \int_0^{IM_{T_R^*}} P[\, f \,|\, IM = x \,] \cdot f_{IM}(x) \cdot dx \tag{23}$$

Where obviously $\lambda^* \leq \lambda_f$ neglecting the integral $\lambda \cdot \int_{IM_{T_R^*}}^{+\infty} P[\, f \,|\, IM = x \,] \cdot f_{IM}(x) \cdot dx$. Anyways the difference between λ^* and λ_f values is negligible if the failure condition is reached with a 100% probability for IM higher than $IM_{T_R^*}$.

$$P[\, f \,|\, IM = x \,] = 1 \qquad \forall x \geq IM_{T_R^*} \tag{24}$$

When the probability is 100% the value of Equation (24) can be employed to represent the difference between λ^* and λ_f as follows:

$$\left|\lambda^* - \lambda_f\right| = \lambda \cdot \int_{IM_{T_R^*}}^{+\infty} P[\, f \,|\, IM = x \,] \cdot f_{IM}(x) \cdot dx = \lambda \cdot \int_{IM_{T_R^*}}^{+\infty} f_{IM}(x) \cdot dx = \lambda_{IM \geq IM_{T_R^*}} \tag{25}$$

implying that the maximum error corresponds to the annual failure rate $IM_{T_R^*}$.

$$\lambda^* = \lambda \cdot \int_0^{IM_{T_R^*}} P[\, f \,|\, IM = x \,] \cdot f_{IM}(x) \cdot dx + 0.00001 > \lambda_f \tag{26}$$

When computing Annual Rates of Failure, in order to avoid their underestimation, the Equation (26) has been employed leading instead to a slight overestimation. Considering the case studies analysed throughout the present study, the maximum considered return period is 100,000 years, corresponding to an error of 10^{-5}. In this calculation, failure has been assumed for larger intensities by replacing the integral part shown in Equation (25) with the rate of exceedance of $IM_{T_R^*}$, as $\lambda_{IM \geq IM_{T_R^*}} = 0.00001$. This overestimates the failure rate and, in some cases, when the first part of the integral is negligible (compared to 10^{-5}), only allows to state that the annual failure rate is lower than 10^{-5}.

The seismic resilience of models throughout the present doctoral dissertation is presented in terms of Mean Annual Frequencies of Exceeding and of Annual Rates of Failure. The information provided by results for each accelerogram of each IM and by the seismic hazard are combined to plot Annual Frequency of Exceedance curves [Kitayama and Constantinou, 2018], [Kitayama and Constantinou, 2019a], [Baker, 2005]. These curves provide the mean annual rate of exceedance (on the y-axis) and the corresponding specified structural response level (EDP level on the x-axis). The utility of these curves is in providing the failure rate distribution over the analysed IMs taking into account both structural fragility and local hazard. The difference between Mean Annual Frequency of Exceedance curves and punctual Annual rates of Failure is that, curves still depend on the Intensity Measure distribution chosen, so that, curves for different sites or return periods cannot be easily compared. Annual Rates of Failure, instead, do not provide a complete representation of the annual probability of exceedance for each IM, but allow a punctual evaluation of the probability of reaching a certain Limit State and can thus be easily compared. in the body of the present doctoral dissertation annual rates of failure have been computed through the R2R tool [Baraschino et al., 2020] and on the basis of the works of [Iervolino et al. 2018], [Iervolino et al. 2019].

5 Civil use buildings seismic performance

The current Italian code provisions, [NTC 2018] allow engineers to design seismic resistant structures with a certain amount of safety for the attainment of performance levels (e.g., Collapse – CLS – or Life Safety – LLS). Although compliance to the code requirements for the capacity design guarantees a certain level of safety, the designer doesn't have any tool to be able to determine probability that the structure, in its life span, under seismic design intensities, will reach (or even exceed) a given performance level. Moreover, the code does not provide an explicit assurance that different structures designed for the same site, or similar structures at different sites, would be characterized by the same safety margin for a given performance level.

The project RINTC (*Rischio Implicito delle strutture progettate secondo le NTC*, in Italian) conducted the first studies which systematically addressed the issue of estimating such probabilities for several classes of buildings designed according to the current code provisions in Italy [ReLUIS, RINCT Workgroup, 2018], [RINCT Workgroup, 2018a], [RINCT Workgroup, 2018b], [http://www.reluis.it/, ReLUIS]. Different Italian sites have been considered characterized by different levels of seismic hazard. Many different buildings have been designed according to different codes (using Italian updated and outdated ones) for five different structural types: unreinforced masonry, reinforced concrete, precast reinforced concrete, steel, base-isolated reinforced concrete structures [Iervolino et al. 2018] [Ragni et al., 2018] [Ricci et al., 2018] [Cardone et al., 2019] [Iervolino et al. 2019] [Ricci et al., 2019] [Flora et al., 2020] [Ponzo et al., 2020]. These probabilities of failure knowledge would be a good basis for further considerations regarding the acceptability of the safety margin of current-code-conforming structures. It is important to notice that the failure probabilities computed within the RINTC project, do not account for the presence of errors that may sometimes lie in real buildings materials and constructions and for some sources of uncertainty. This implies that the performance level failure for these buildings has been assumed to occur when specific,

deterministically chosen threshold values for the Engineering Demand Parameters (EDPs) chosen to monitor the structural response, are exceeded. Similarly, material and structural elements dimensions uncertainties are neglected. Finally, soil has not been modelled nor its failure accounted for. The defined failure criteria and associated EDP threshold values do not imply that, when exceeded the structure is expected to experience a total collapse. Thus, reaching or even exceeding such values may result in a structure still standing but completely unserving and unrepairable.

The present doctoral dissertation discusses the results of the studies conducted within the RINTC project for DCCSS Base-Isolated (BI) reinforced concrete structures.

5.1 Case Studies

The prototype structure represents typical residential RC-frame buildings located in two different seismicity zones, according to the Italian national hazard map, and is characterised by a regular plan of approximately 240 square meters and 6 stories above ground. The ground level height is 3.4 m while the other stories heights are all 3.05 m, the building includes a staircase, designed with knee beams, and all stories have the same 25 cm-thick slab. Infill panels have been considered as regularly distributed in plan and elevation, with different opening percentages, infills dead loads have been considered in the design process. In the base-isolated configuration, a supplementary RC base slab has been implemented below the ground floor columns.

Eight case studies of base-isolated buildings located in the site of Naples and of L'Aquila (Italy) consisting a new construction (analysed in both the two sites) and six existing buildings have been analysed in this study. The superstructure of the new building ([Ragni et al., 2018] [Cardone et al., 2019] [Flora et al., 2020] [Iervolino et al., 2018] [Ricci et al., 2018]) has been

designed with the minimum spectral acceleration of $S_e = 0.10\,M$, with M being the seismic mass of the superstructure, and medium ductility class (CD "B") according to the Italian Seismic Code [NTC 2018] prescriptions. Figure 5.1 shows a typical elevation and plan view of the new construction structure.

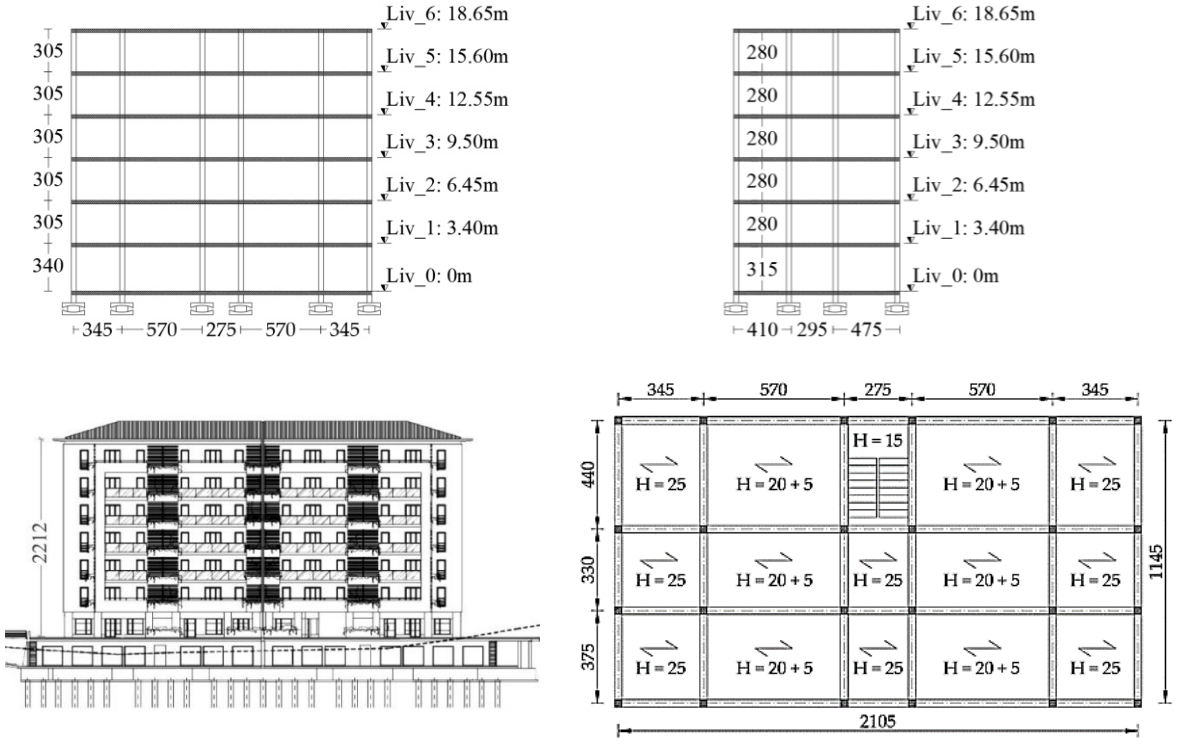

Figure 5.1. New construction isolated buildings: side views and floor plan.

Figure 5.2 shows the typical floor plan of the two groups of archetype existing buildings examined in this study, namely: Seismic Load Design (SLD) buildings (see Figure 5.2a) and Gravity Load Design (GLD) buildings (see Figure 5.2b). The buildings are intended for residential use. They feature 5 x 3 bays and 6 stories above ground. Also in the case of existing buildings, the floor area 240 square meters and interstorey heights are 3.4 m for the 1st and 3.05 m for all the other floors. According to NTC2018, the buildings can be defined as regular, both in plan and in elevation. Each group of buildings includes three case studies differing for construction period (50s-60s, 70s, 80s-90s), hence material characteristics and structural

details. The building configuration is the same for the all the buildings only differing for some structural characteristics, such as the presence (or not) of internal beams in the long direction, the size of beam/column cross sections and the corresponding reinforcement ratios. GLD buildings are supposed to be located in the city of Naples (southern Italy), which is characterized by a medium level of seismic hazard for Italy. SLD buildings are supposed to be located in the city of L'Aquila (central Italy), which is characterized by a high level of seismic hazard for Italy. The buildings have been defined by means of simulated design [Ricci et al., 2019], in accordance with old technical standards. In particular, the buildings located in Naples have been designed for gravity loads only (GLD) according to [D.M. 30/5/1974]. The buildings located in L'Aquila have been defined based on a simulated Seismic Load Design (SLD), considering low seismic force levels, in accordance with older seismic classifications standards [D.M. 14/2/1992] and outdated technical standards [D.M. 24/1/1986].

Table 5.1 Summary of three-dimensional case studies considered.

Site	*Label*	*Construction age*	*Design Codes*
L'AQUILA	S50-60	1950s-60s	[RD 640/1935] – [RD 2229/1939]
	S70	1970s	[L 1684/1962] – [DM 30/05/1972] – [DM 30/05/1974]
	S80-90	1980s-90s	[DM 27/07/1985] – [DM 24/07/1986] – [DM 14/02/1992]
	AQ_New	2018	[NTC 2018]
NAPLES	G50-60	1950s-60s	[RD 2229/1939]
	G70	1970s	[DM 30/05/1972] – [DM 30/05/1974]
	G80-90	1980s-90s	[DM 27/07/1985] – [DM 14/02/1992]
	NA_New	2018	[NTC 2018]

Concerning the structural configuration, the outer beams of all the buildings are deeper than the slab, while internal beams are flat. In GLD buildings, the internal beams are positioned along the short-direction only. All the stories feature the same slab (one way RC slab with hollow

clay bricks), whose total thickness is 25cm. It is worth noting that in base-isolated configurations, a supplementary floor, composed by a grid of RC beams, has been added below the ground storey.

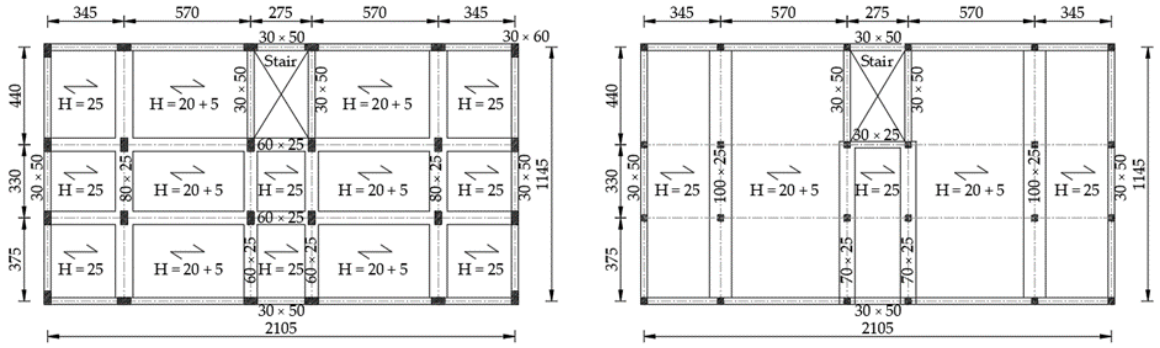

Figure 5.2. Existing buildings prototype plan views for a) Seismic Load Design and b) Gravity Load Design.

According to the technical practice of the design period, masonry infills featuring a double layer of hollow clay bricks (120+80 mm thickness for the 1950s-60s and 70s buildings, 150+80 thickness for the 1980s-90s buildings), with 100 mm (70mm for 1980s-90s buildings) inner cavity, have been considered. Masonry infills are regularly distributed both in plan and in elevation, featuring different percentages of openings in the long direction (in the short direction there are no openings). A good connection of the masonry infill walls with the surrounding RC frame has been assumed for the purpose of the seismic performance assessment of the buildings. More details about the structural details of RC members and masonry infills can be found in [Ricci et al., 2019]. Table 5.1 shows a summary of considered case studies and their relative design code.

5.1.1 Modelling

Structural elements of the superstructure have been modelled via a lumped plasticity model, while elastic beams have been used to model the base floor grid above the isolation system (see Figure 5.3a). The structural model also includes the staircase featuring inclined beams and cantilever steps. The cyclic degrading behaviour of plastic hinges has been described implementing the Ibarra-Medina-Krawinkler [Ibarra and Krawinkler, 2005] [Ibarra et al., 2005] model (*modIMKmodel)* in the OpenSEES framework. In this study, 5% Rayleigh damping is used to model the viscous damping of the superstructure. Previous studies have shown that this approach could result in fictitiously large damping forces in base isolated buildings resulting in underestimation of the first-mode and higher mode responses. Future studies focusing on the topic should also consider alternative approaches proposed in the literature for modeling the viscous damping of the superstructure [Ryan and Polanco, 2008].

The possibility of shear failures arises before or after flexural yielding has been taken into account, thus all hinges have been pre-qualified either as ductile or shear critical. In ductile hinges, the shear failure does not occur and the moment-rotation backbone curve is not modified. For shear critical hinges, shear failure is expected for a certain level of displacement (or rotation), in this case the moment-rotation backbone curve is modified beyond the critical rotation by a softening branch whose slope is derived from the empirical formulation reported in [Aslani and Miranda, 2005]. A more detailed description of these collapse criteria can be found in [Ricci et al. 2018]. Joint panels at beam-columns interfaces have been modelled using the so-called *Scissors model* capable of predicting their experimental behaviour for non-ductile RC frames [De Risi et al., 2017].

The mechanical behaviour of masonry infills has been modelled in a particularly detailed way, as they can significantly affect the seismic response of RC frame buildings (featuring double-layers masonry walls with high slenderness ratio and weak beam-column joints without

adequate shear reinforcement), triggering local failure mechanisms and even threaten human life in case of out-of-plane collapse. The masonry infills In-Plane (IP) behaviour has been modelled with an equivalent compression-only strut. The backbone curve of the diagonal strut has been defined on the basis of a modified version of the Decanini model [Sassun et al., 2016], while the effect of openings has been taken into account through suitable strength/stiffness reduction factors [Decanini et al., 2014].

Both the Out-Of-Plane (OOP) and the IP/OOP interaction effects have been taken into account in the modelling strategy (see Figure 5.3b). Finally, local shear interactions, between masonry infills and adjacent RC columns, have been represented implementing shear springs at the ends of the columns to reproduce their nonlinear shear response triggered and amplified by the action of the adjacent equivalent compression-only diagonal strut. More information about superstructure modelling can be found in [Di Domenico et al., 2021] and [Ricci et al., 2020]. The isolation system *OS_DCCS* (Table 3.3) model has been adopted for all case studies, and the friction coefficient dependency on the axial force and instantaneous velocity variabilities has been considered.

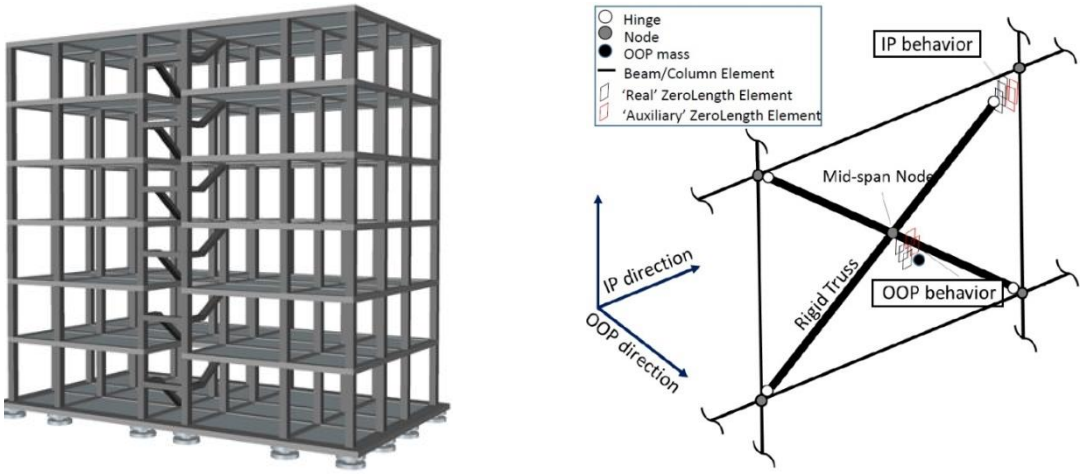

a) b)

Figure 5.3. a) Schematical representation of the base-isolated prototype building and b) IP/OOP infill panels model.

5.1.2 Nonlinear Static Analyses

Once all models of fixed-base prototype buildings have been set up, nonlinear static analyses (Pushover (PO) analyses) have been performed in order to find the elastic limit forces V_e required for isolation systems retrofit design on existing structures. Pushover analyses have been carried out with two different lateral force patterns: "modal" and "uniform". In particular, pushover curves resulting from the uniform force pattern have been considered, assuming a mainly translational deformed shaped for the isolated frames.

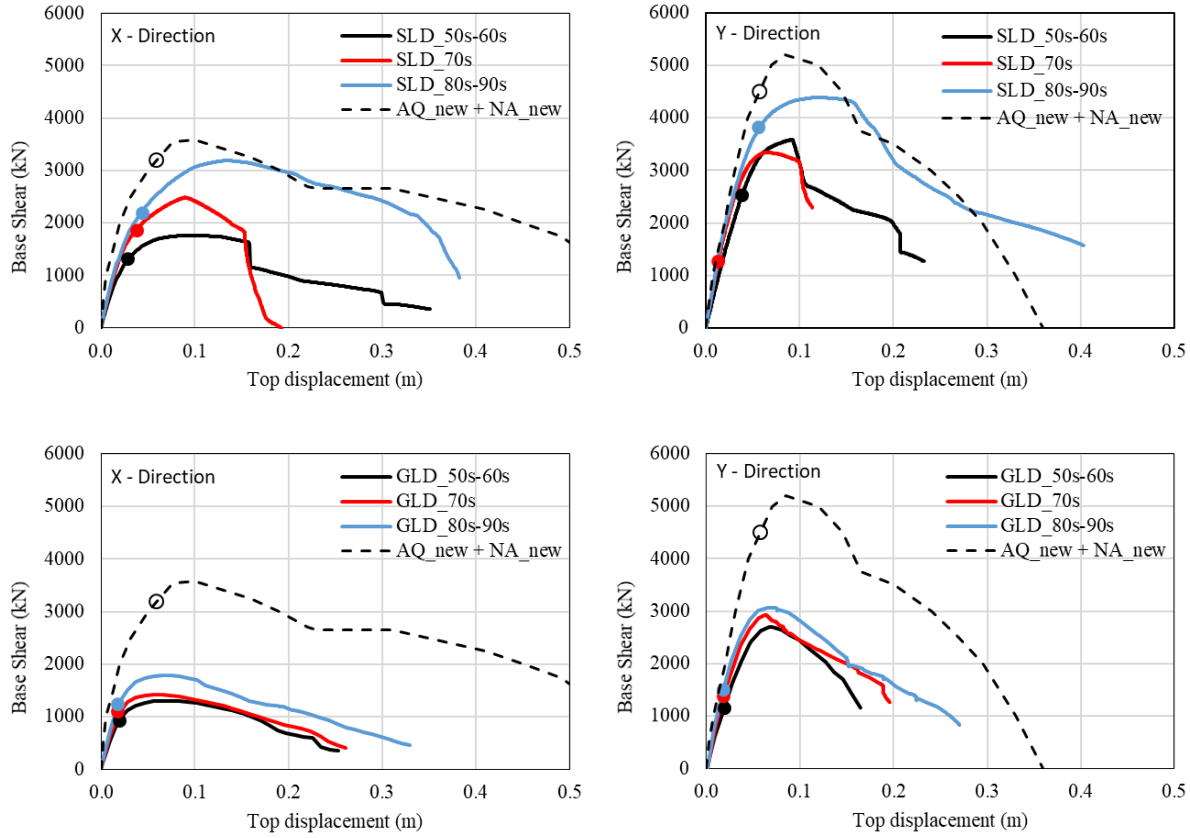

Figure 5.4. Pushover curves and elastic base shear limits for all case studies and for both main horizontal directions (X and Y).

The elastic limit values, in terms of base shear (V_e), of the superstructure (in the fixed-base configuration), have been identified as the force level of the capacity curve corresponding to the occurrence of the first plastic hinge in the weaker direction of the building (i.e. the minimum base shear at the first yielding). In Figure 5.4, for each case analysed, the elastic limit is outlined

by a circle with the same colour of the corresponding capacity curve. It is worth to noting that the identified elastic limits correspond to the first plasticization of all the structural element of the building (beams or columns) excluding those of the staircase, for which a local retrofit has been supposed. This assumption was necessary in order to avoid excessively low elastic limits to lead, in some cases, to unfeasible isol ation systems. Elastic limits are summarized in Table 5.2 in terms of base shear V_e and associated top diplacement $d_{top}(V_e)$.

Table 5.2 Summary of the limits corresponding to the occurrence of the first plastic hinge on PO curves.

Case Study	X – Direction		Y – Direction	
	V_e [kN]	$d_{top}(V_e)$ [m]	V_e [kN]	$d_{top}(V_e)$ [m]
S50-60	1317	0.029	2522	0.039
S70	1852	0.039	1260	0.013
S80-90	2194	0.044	3812	0.056
AQ_New	3188	0.059	4293	0.057
G50-60	922	0.020	1145	0.019
G70	1103	0.018	1367	0.018
G80-90	1239	0.018	1491	0.018
NA_New	3188	0.059	4293	0.057

5.1.3 Isolation system design

The design displacement d_{bd} of isolation systems has been estimated referring to the simplified linear analysis method considering the horizontal dynamic translation of DCCSS bearings, with the superimposition static torsional effect, and assuming the superstructure as a rigid body. It is worth noting that, according to the European Standard [UNI EN 15129 (2009)] the reliability factor for isolator displacements shall be at least 1.2 for buildings, i.e., $d_{Ed} = 1.2\, d_{bd}$, where d_{bd} is the design displacement (at CLS). The main parameters of the linear equivalent model of the isolation system based on DCCSS bearings are the effective stiffness k_{eff}, effective

period T_{eff} and effective damping ξ_{eff} as reported in equations (27). The friction pendulum forces are proportional to the device axial load and the sliding velocity.

$$k_{eff} = N_{Sd}\left(\frac{1}{R_{eff}} + \frac{\mu}{d_{Ed}}\right), \qquad T_{eff} = \pi\sqrt{\frac{1}{g\left(\frac{1}{R_{eff}} + \frac{\mu}{d_{Ed}}\right)}}, \qquad \xi_{eff} = \frac{2}{\pi}\cdot\frac{1}{\frac{d_{Ed}}{\mu \cdot R_{eff}} + 1} \tag{27}$$

The design procedure for the new construction case studies for L'Aquila (AQ_new) and Naples (NA_new) sites is shown in Figure 5.5, in terms of Acceleration-Displacement Response Spectra (ADRS). Isolation system devices have been designed so that the spectral acceleration corresponding to the effective period $S_a\ (T_{eff})$ is below the minimum value of $S_e = 0.10\ g$ required from the italian code NTC18 [NTC2018] (§7.0- §7.10.2). The design displacement d_{bd} at the CLS and the characteristics of designed DCCSS bearings are summed up in the top figures of Figure 5.5.

Table 5.3 Geometric characteristics and main design parameters of the isolation system at the CLS.

Case Study	R_{eff} *[mm]*	μ *[%]*	K_{eff} *[kN/mm]*	T_{eff} *[sec]*	ξ_{eff} *[%]*	d_{bd} *[mm]*	Φ *[mm]*	d_{max} *[mm]*	d_c *[mm]*
S50-60	3700	2.5	0.318	3.14	28	213	200	±300	±330
S70	3700	2.5	0.246	3.09	21.4	238	200	±300	±330
S80-90	3700	2.5	0.296	2.97	26	216	200	±300	±330
AQ_New	3700	2.5	0.357	3.17	21	237	200	±300	±330
G50-60	4500	2.0	0.296	3.28	28	125	165	±250	±275
G70	4500	2.0	0.303	3.01	28	125	165	±250	±275
G80-90	4500	2.0	0.328	2.98	28	125	165	±250	±275
NA_New	2500	2.5	0.560	2.53	23	134	250	±150	±165

The design procedure of the isolation system for existing building case studies starts from the spectral acceleration associated with the occurrence of the first plastic hinge ($S_e^* = V_e/M$) as shown in Figure 5.5 (red dashed lines). The elastic limit of the base shear V_e of the superstructure in the fixed-base configuration has been identified from pushover curves (as shown in Table 5.2). The minimum value of the fundamental period $T_{iso,min}$ of the base-isolated system is then found.

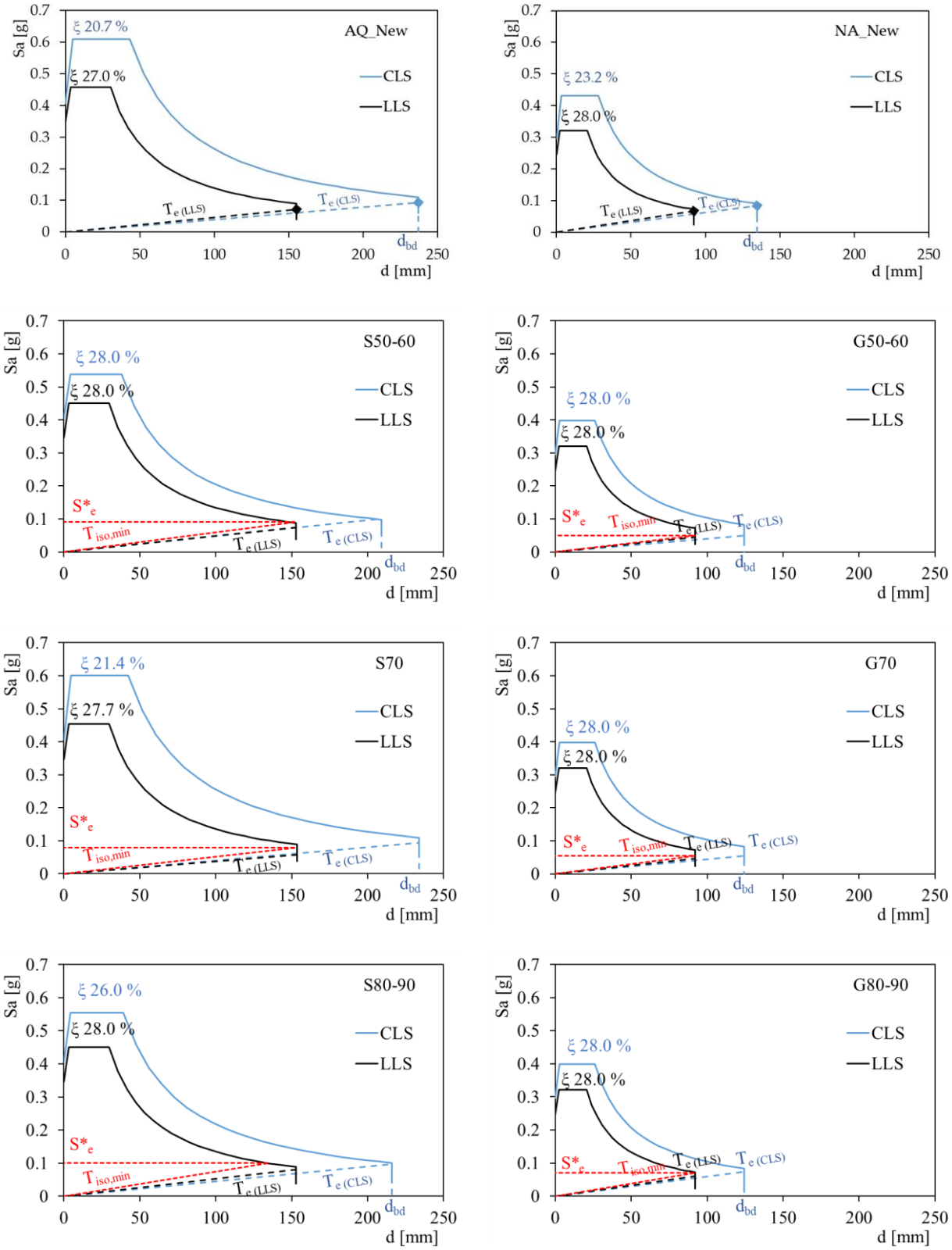

Figure 5.5. Isolation systems design procedure on ADRS Spectra.

All of the isolation systems have been designed considering a unitary structural behaviour factor $q = 1$ [NTC 2018]. The isolation systems characteristics are summarized in Table 5.3. The

maximum manufacturer displacement d_{max} has been assumed by catalogue, taking into account torsional effects, and the geometric capacity displacement d_c has been assumed as $d_c = 1.10 \cdot d_{max}$.

5.2 Seismic input

Multi-stripe non-linear dynamic analyses have been carried out considering 20 ground motions per 10 intensity measure levels (IMs). The estimation procedure is necessarily supported by the assessment of the ground motion hazard at the considered sites of L'Aquila and Naples. In this work, the ITACA record database [http://itaca.mi.ingv.it], which includes accelerograms from Italian earthquakes, has been the main source for ground motion records acquisition. The particular restrictions and conditions imposed by the selection procedure required further records acquisition from the NGAwest2 database [http://ngawest2.berkeley.edu/], which includes accelerograms from earthquakes that occurred in different parts of the world. NGAwest2 records have been especially used for high seismic intensities. The record selection algorithm employed in this study is the Conditional Spectrum (CS) approach proposed by [Baker, 2011], [Jayaram and Baker, 2011] and [Lin et al., 2013]. The CS approach provides the distribution of the spectral acceleration $S_a(T_i)$ at any period T_i, conditioned on a given value of $S_a(T_j)$ where T_j is a fixed period of interest (in this study T_j has been assumed equal to the base-isolated structure fundamental period). For the present study, the CS approach has been used within the Multiple Stripe Analysis (MSA) framework [Jalayer and Cornell, 2002]. The MSA methodology aim is to obtain the distribution of one or more EDPs for many different intensity levels $S_a(T_j)$. Nonlinear Time History Analyses (NTHA) have been carried out for of all the selected levels of $S_a(T_j)$. The used automatic procedure for record selection is the one freely available at [http://web.stanford.edu/~bakerjw/research/conditional_spectrum.html]. The record selecting procedure steps are here briefly described:

a) definition of the distribution of spectral accelerations $S_a(T_i)$ conditioned on $S_a(T_j)$ for any $T_i \neq T_j$;

b) simulation of n response spectra, where n is the target number of records for each stripe, according to the CS;

c) selection of records which can be individually scaled to grant the best fitting values with the simulated spectrum of the CS approach.

This enhanced selection procedure is integrated in a MSA in which ten different Intensity Measures (IM) of $S_a(T_j)$ were considered according to the hazard levels of L'Aquila and Naples. Selected hazard levels correspond to the mean return periods values listed in Table 5.4.

The value of the reference period T_j was selected to be appropriate for the structures whose response will be evaluated. NTHA have been performed using the set of ground motions characterized by a conditioning period equal to $T_j = 3.0s$ for both case studies. For each intensity level, 20 different accelerograms were selected. As reported in Table 5.4 IM2, IM5, and IM6 correspond to the return periods of the DLS, LLS, and CLS. The attenuation law of Akkar and Bommer [Akkar and Bommer, 2010] has been implemented to compute hazard and disaggregation.

Table 5.4 Return Periods T_R [y] and Spectral acceleration $S_a(T = 3\ s)$ expressed in [g] for chosen IMs.

Intensity Measure (IM)	***1***	***2 (DLS)***	***3***	***4***	***5 (LLS)***	***6 (CLS)***	***7***	***8***	***9***	***10***
T_R [y]	***10***	***50***	***100***	***250***	***500***	***1,000***	***2,500***	***5,000***	***10,000***	***100,000***
L'Aquila S_a (T = 3 s) [g]	0.0002	0.011	0.031	0.062	0.110	0.177	0.271	0.384	0.576	1.053
Naples, S_a (T = 3 s) [g]	0.001	0.009	0.026	0.044	0.067	0.093	0.126	0.162	0.216	0.348

As an example, the elastic spectra of seismic inputs for IM5 and IM6, compared with NTC18 [NTC 2018] spectra provided by code respectively for LLS and CLS, are reported in Figure 5.6 for the sites of L'Aquila and Naples, respectively. Figure 5.6 shows how the mean values of

$S_a(T_i)$ for the spectra are slightly (in L'Aquila cases) or much (in Naples cases) different from the acceleration values provided by the Italian code [NTC 2018] anyways, the acceleration value for the target period $S_a(T = 3.0s)$ is always about the same. The earthquake vertical component has been neglected in all analyses.

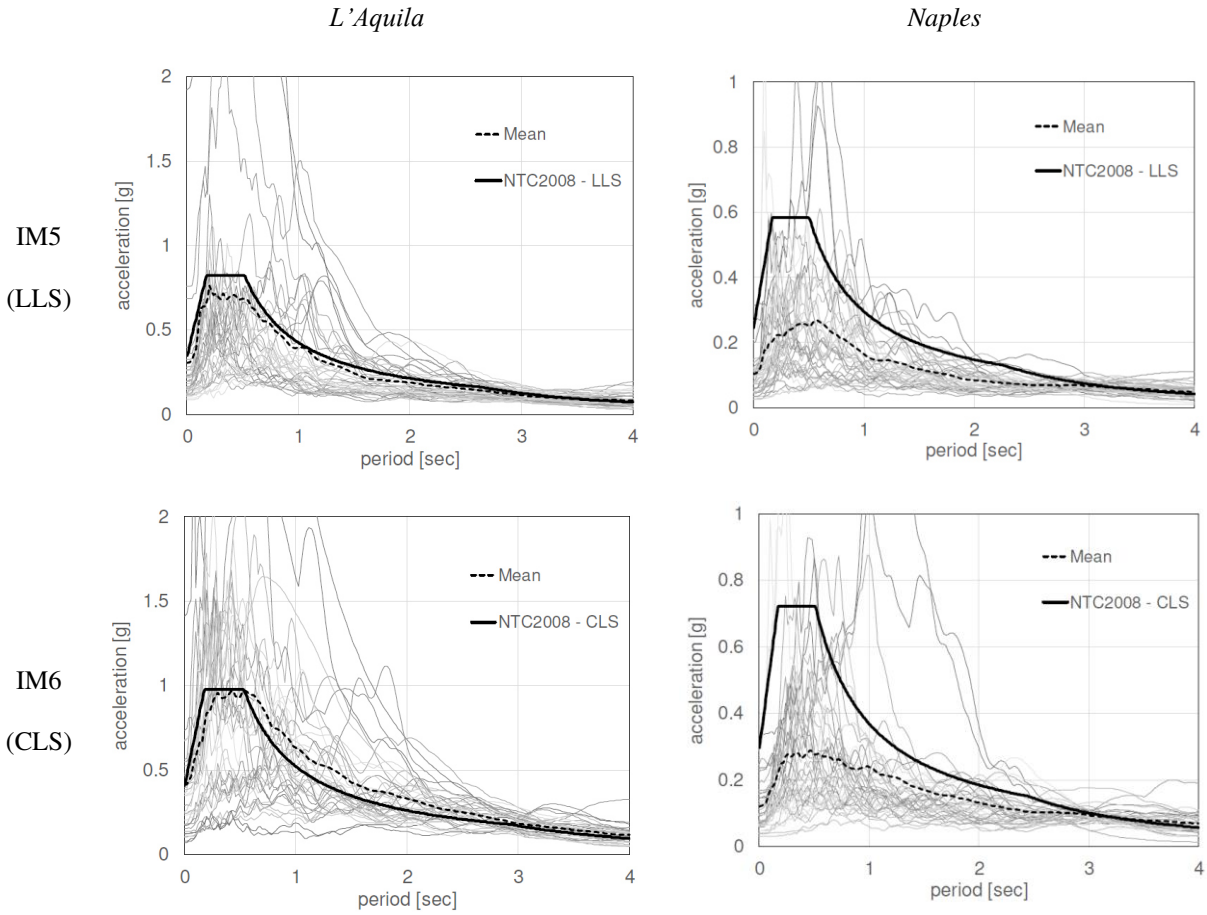

Figure 5.6. Acceleration response spectra of ground motion for IM5 (LLS - $T_R = 500y$) and IM 6 (CLS - $T_R = 1000\ y$) for the sites of L'Aquila and Naples.

5.3 Definition of Performance Levels

The seismic performances of the examined case studies have been evaluated considering two specific performance levels, referred to as: Usability-Preventing Damage (UPD) and Global Collapse (GC) performance level. The two performance levels correspond to the NTC18 DLS and CLS respectively as previously mentioned in section "§1.2 Reference standards" of the

present doctoral dissertation. The occurrence of both performance levels has been assessed following a multi-criteria method, considering differing failure modes and conditions for both superstructure and isolation system. The engineering demand parameters (EDP) defined to control the seismic performance of base-isolated buildings are the superstructure top displacement and the isolation system displacement.

The UPD performance level is associated with interruption of use of the building after short return period seismic events due to either:

a) light-extensive or serious-limited damage to non-structural elements
b) onset of damage in structural elements.

In the proposed case studies, masonry infills and partitions are the main non-structural elements, whose repair costs, after a seismic event, are generally disproportionately high compared to the structural element repair costs. According to the construction practice of the time (see Table 5.1), masonry infills and partitions have been put in contact with the surrounding structural elements without any gap or connection capable to accommodate relative displacements between non-structural elements and RC frame. During an RC frame building construction, masonry infills generally realized on site after the RC has completely hardened, this practice implies that they can be assumed as non-load-bearing elements, and can thus be treated as non-structural components. Anyways, although their structural function is irrelevant, they can still represent a threat to life when out of plane collapse occurs or when their collapse can prevent the safe and easy evacuation of a building. To this scope, both in-plane and out-of-plane behaviours of masonry infills has been considered in the numerical model and in the definition of collapse criteria for the UPD performance level. The most widespread infills configuration is that of a double layer with an inner cavity, and is the same considered for all case studied analysed. An accurate description of the in-plane damage states (DS) of masonry infills (see Figure 5.7) has been described in [Cardone and Perrone, 2015] as follows:

a) DS1 (Light Cracking). At this damage state, the detachment of the masonry panel from the RC frame occurs, at the interface with the upper beam and along the upper part of the columns beside. A light diagonal cracking of the infill (very few cracks with width <1 mm) in both directions may also occur;

b) DS2 (Extensive cracking). At DS2, the cracks developed in the previous DS open further (1 mm<width<2 mm). New diagonal cracks may form in both directions (25-35% of the infill panel surface is assumed to be cracked at DS2), and the failure of single bricks, in the upper corners of the infill may also occur;

c) DS3 (Corner crushing). This damage state involves the detachment of large plaster area and significant sliding in the mortar joints. In addition, about the 30% of the panel area is assumed to be affected by crushing and/or spalling of bricks. The repair costs for the infill panel come very close to the new construction costs, which is, in most of cases, more convenient. At this DS damage of fixture frames is not expected;

d) DS4 (Collapse). DS4 corresponds to the in-plane or out-of-plane (whichever occurs first) global collapse of the wall. Furthermore, fixture frames are damaged and cannot be retrieved or used again.

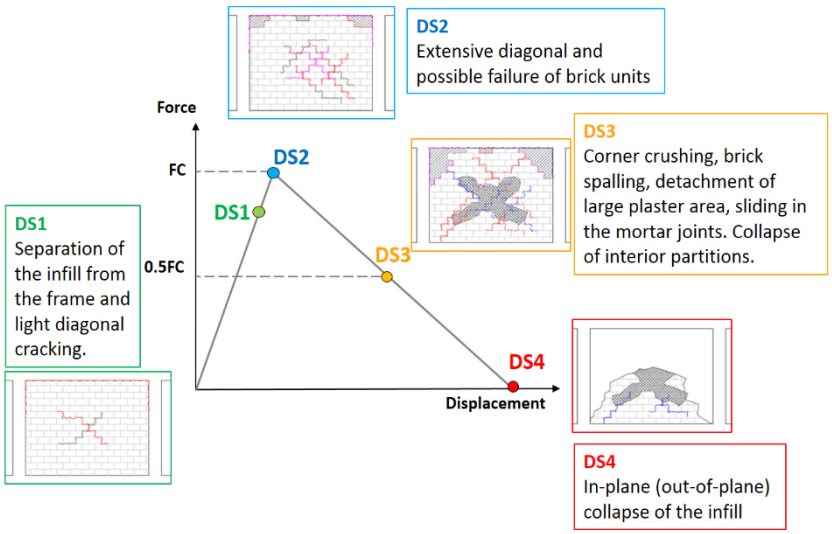

Figure 5.7. Damage states considered for masonry infills in the attainment of the UPD performance level.

A multi-criteria approach has been adopted to define the limit value of the relative global displacement of the building (building top displacement d_{top} minus isolation system displacement in each main horizontal direction) for UPD level combining conditions related to easy non-structural components reparability and no service interruption with the conditions of protecting structural members from damage for frequent earthquakes [Ruggieri and Uva, 2020]. These relative global displacement values have been derived from pushover analysis (Figure 5.4). Different threshold values have been estimated, corresponding to the attainment of different limit conditions for non-structural elements, then, the lowest value has been considered in the nonlinear analyses. The three main limit conditions considered for the UPD definition have been:

a) attainment of a light-widespread damage condition for less than 50% of masonry infills in each main direction, corresponding to the attainment of a maximum lateral force value around the peak strength in the relevant skeleton curves;
b) attainment of a severe damage condition, corresponding to the attainment of 50% strength of the peak strength value, on the post-peak branch, for the relevant skeleton curve for the first masonry infill;
c) attainment of a limit value of base shear corresponding to 95% of the peak strength of the capacity curve from pushover analysis. In this condition only a light structural damage can be observed.
d) the out-of-plane collapse condition for infill panels on any floor has been reached.

For the GC performance level, both the superstructure and the isolation system collapse conditions have been considered. The GC performance level has then been considered if either the superstructure or the isolation system would have failed.

For the superstructure, the GC has been considered reached with the occurrence of the first of the following conditions [Ricci et al., 2018]:

a) attainment of a relative global displacement equal to that associated with a 50% decrease of the lateral strength on the capacity curve of the fixed-base building;
b) loss of axial load bearing capability for an RC column due to shear failure;

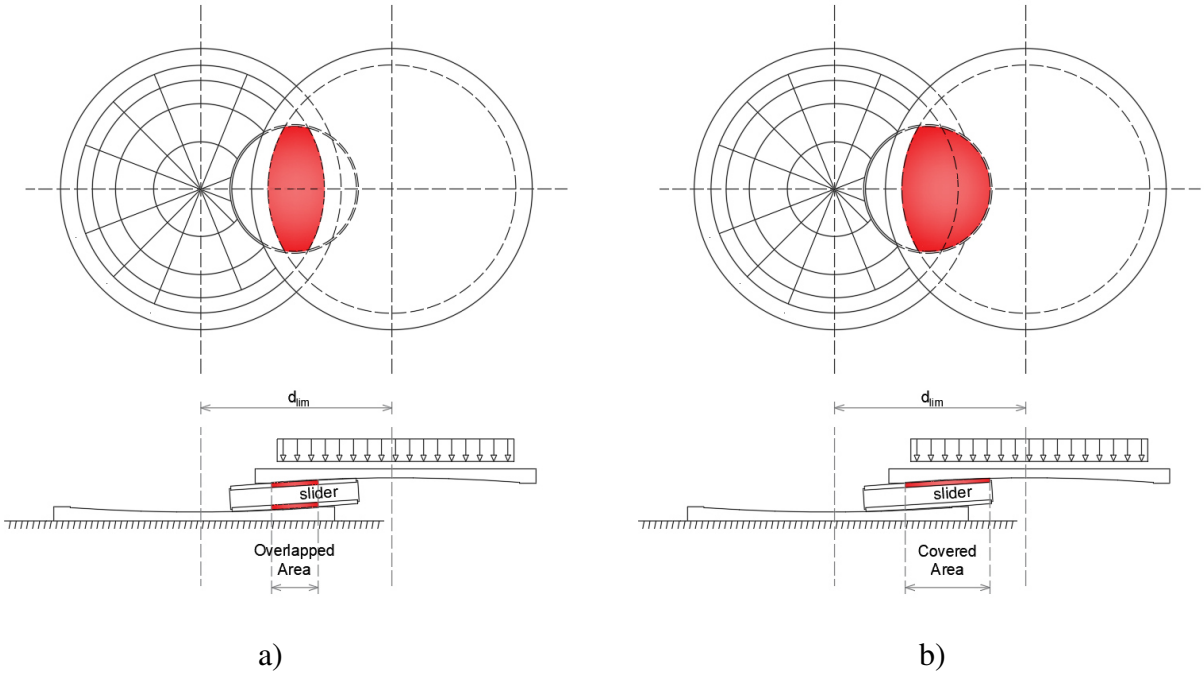

Figure 5.8. a) Overlapped and b) covered area of pressure for DCCSS slider in over-stroke condition.

For the isolation system, the GC is defined as the performance level in which one DCCSS device reaches the limit displacement d_{lim} in the over-stroke regime linked to the attainment of the first of the following conditions:

a) vertical instability: when the DCCSS inner slider runs beyond its geometric capacity displacement d_c in the over-stroke regime, it may undergo a displacement so large that it falls off of the housing plate losing the ability to support vertical loads;
b) limit pressure reached at the interface between inner slider and sliding pads. When the device enters in the over-stroke regime, the contact area between the plates surfaces and

the inner slider reduces and a peak in contact pressure can be reached. For the case studies, a Polytetrafluoroethylene (PTFE)-based sliding material with a maximum contact pressure of 60 MPa has been assumed. Depending on the thickness of the inner slider, the covered area at the sliding interfaces or the overlapped area between the backing plates can be considered for the computation of the average contact pressure: if the thickness is enough to ensure a proper vertical stress distribution (as in the present study) the former can be adopted, otherwise the latter represents a more correct parameter (see Figure 5.8).

c) maximum number of over-stroke cycles. A maximum number of two over-stroke cycles has been allowed in order to take into account the sliding material damage due to the friction coefficient increase in the over-stroke regime.

All failure conditions and limit values are summarised in Table 5.5.

Table 5.5 Summary of performance levels EDP threshold values for the isolated buildings.

Case Study	*UPD d_{top} threshold values*		*GC – Superstructure d_{top} threshold values*		*GC – Isolation system d_{lim} values*
	X [mm]	*Y [mm]*	*X [mm]*	*Y [mm]*	*[mm]*
S50-60	57	66	300	230	418
S70	73	61	160	129	415
S80-90	96	74	370	360	420
AQ_New	59	57	502	273	414
G50-60	39.8	50.5	232	146	344
G70	34.1	47.6	241	132	343
G80-90	41.3	46.0	264	192	345
NA_New	59	57	502	273	290

UPD: threshold values refer to the first limit condition between (i) attainment of a light-widespread damage condition; (ii) attainment of a severe damage condition; (iii) attainment of a limit value of base shear corresponding to 95% of the peak strength of the capacity curve from PO analysis; (iv) the out-of-plane collapse condition for infill panels on any floor has been reached.

GC – Superstructure: threshold values refer to the first limit condition between (i) attainment of a relative global displacement equal to that corresponding to a peak strength reduction of 50% on the negative slope of the PO curve and (ii) loss of axial load bearing capability for an RC column due to shear failure;

GC – Isolation System: threshold values refer to the first limit condition between (i) vertical load instability (ii) the displacement exceeds a limit value related to the maximum contact pressure between sliding interfaces (60 MPa) (iii) the device undergoes more than two over-stroke cycles.

5.4 Nonlinear Time History Analyses

Multi-Stripe non-linear dynamic analyses (NTHA) have been performed to evaluate the seismic performances of the examined case-studies towards GC and UPD performance levels. As mentioned before 20 different bidirectional analyses have been performed for 10 earthquake intensity (IM) levels. Considering that the fundamental periods of the examined case-studies range from 2.5 to 3.5s, a unique conditioning period (T_j) equal to 3.0s has been assumed for the seismic performance assessment. For the GC performance level, the analyses results are provided in terms of number of failures as a function of the IM level. More in detail, the total number of records causing a collapse condition for the examined case-study is reported as a function of the IM level. For the Global Collapse performance level, the first failure has always been recorded at the isolation system level.

For the UPD performance level, diagrams summarizing the demand-capacity ratios (D/C) associated with each ground motion pair, as a function of the earthquake intensity level, are presented (for each direction). In particular, the capacity (C) levels have been summarized in Table 5.5, while, the demand (D) is represented by the maximum top displacement d_{top} of the superstructure (with respect to the isolation system) directly recorded during NTHA.

It is worth noting that, when the isolation system GC anticipates the occurrence of the UPD failure condition during the analysis, the UPD is considered attained for the analysis. Finally for each IM level, the total number of records leading to a failure condition is also provided. An insight on the GC performance level is given by Figure 5.9 where an example of force vs. displacement behaviour and displacement orbit of the corner DCCSS device for the S80-90 case study at IM6 (EarthQuake (EQ) number 2), together with the ultimate displacement (black continuous line) and the displacement capacity (black dashed line). As can be observed from Figure 5.9a the OpenSEES numerical model well describes the over-stroke displacement. The collapse of the DCCSS is attained when isolators displacement $d > d_{lim}$ (see Figure 5.9b).

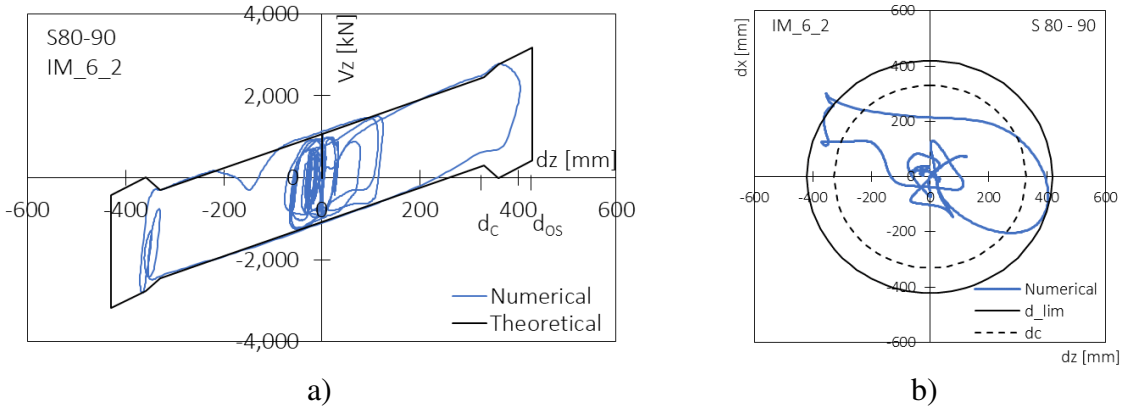

a) b)

Figure 5.9. (a) force vs displacement diagram and (b) plan view of IM_6_2 results of the S80-90 case study.

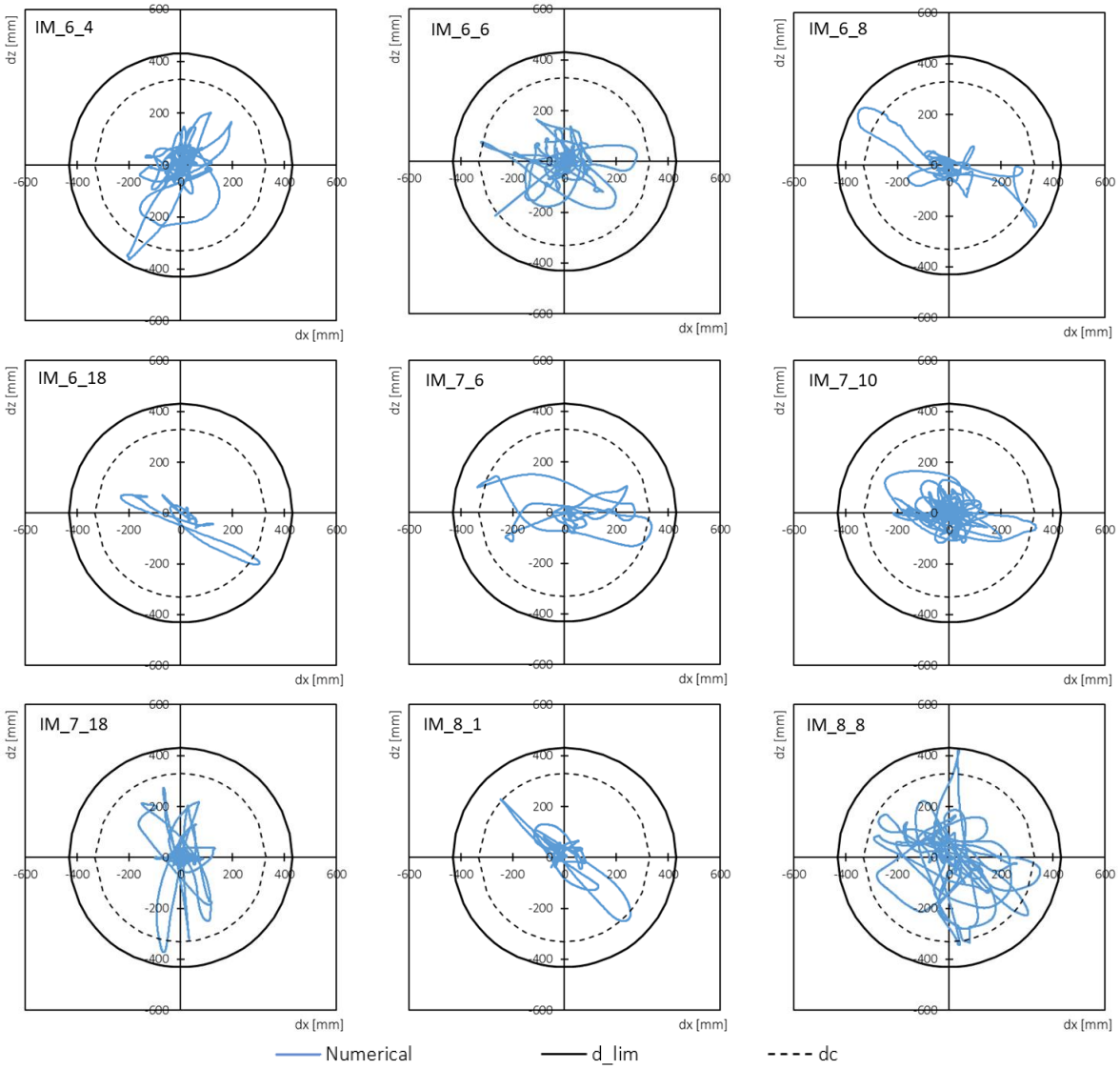

Figure 5.10. Results of the S80-90 case study when the maximum displacement is: $d_c < d < d_{lim}$

Figure 5.10 shows results for the corner DCCSS device of the S80-90 case study for all the accelerograms characterized by a maximum displacement recorded during the analysis $d_c < d < d_{lim}$, providing some examples of record in which the number of cycles could determine the attainment of the GC failure condition.

The GC performance level general insight is provided by Figure 5.11 showing the number of records vs. IM for which the EDP limit is attained. Results show how, for the cases located in the site of L'Aquila, the GC is attained for seismic intensities around the design one (IM6 – CLS), while for Naples cases, this condition is only reached for higher seismic intensities. These results highlight the differences between the two analysed seismic zones. As Figure 5.11 general trend shows, the seismic retrofit of existing structures attains performance levels which are very close to current code design ones for the site of L'Aquila. The seismic performance of buildings located in both the sites of L'Aquila and Naples improves as the age of the design code becomes more recent. It has to be noticed, anyways, how, for buildings located in the site of Naples, the performance fully complies with current codes design standard even for buildings designed with the most outdated codes. For L'Aquila retrofitted buildings the expected seismic performance requirements have not been fully met having some GC cases for the IM 6 intensity. This behaviour is probably linked to the seismic input variability and to the design effective periods which slightly differ from the design target one T=3.0sec as exposed before.

It also has to be noticed how, the general tendence of the performance improvement as the design codes come closer to todays ones, is slightly different for the cases S80-90 and AQ_New. Figure 5.11 shows that the number of GC failures characterizing the AQ_New case study is slightly higher than the S80-90 one. Figure 5.12 shows the ξ_{eff} - damped displacement spectra of the time histories characterized by the GC failure for AQ_New but not for the S80-90 case, the figure also shows the design periods for both cases and the limit displacements. The black and grey dots represent the maximum displacement reached during the analyses respectively

for the S80-90 and the AQ_New case, showing how, only for the latter, the limit displacement d_{lim} has been reached.

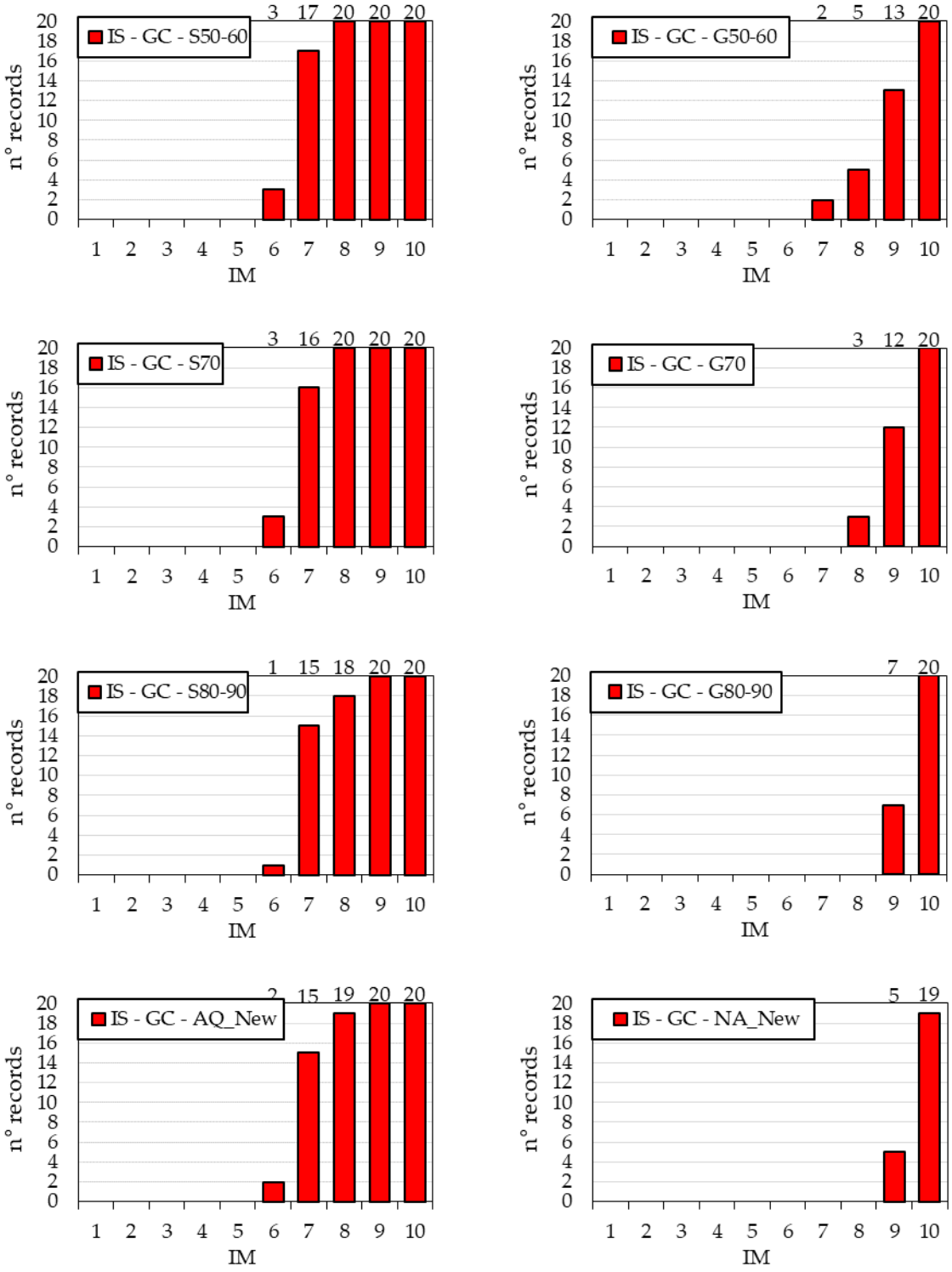

Figure 5.11. GC results for the eight case studies analysed.

Figure 5.12 highlights how, the difference in design parameters (Table 5.3) in GC limits (Table 5.5) and the seismic input variability can be held accountable for the observed differences on the IM6_EQ4 and IM8_EQ8 time histories.

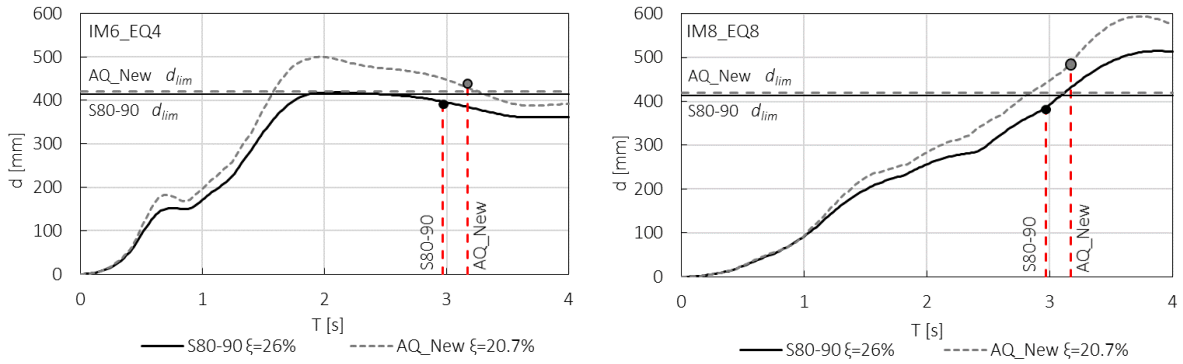

a) b)

Figure 5.12. Displacements spectra for a) IM6_EQ4 and b) IM8_EQ8 time histories with periods and d_{lim} values for S80-90 and AQ_New case studies.

The UPD performance level are reported in Figure 5.13 and Figure 5.14 in terms of D/C ratios vs IM. The total number of failure cases (D/C ≥ 1) is shown on top of the charts. Red dots represent the superstructural UPD failure cases, while crossed dots the cases in which isolation system failure (GC) is registered, for which, the UPD performance level is considered attained regardless of the D/C ratio.

As can be seen, in accordance with the GC results, a significant number of failures is only registered for intensities higher than the IM5 for the case studies S60 and G60, and no cases of UPD failures are recorded for intensities around the Damage Limit State (IM2 – DLS). The only exception is the AQ_New case study, in which 1 failure out of 20 analyses is recorded at IM3, this is probably due to the accurate isolation system and structural design possible for new construction buildings. In fact, 1 failure on 20 corresponds to a 5% probability of attainment

for the UPD level which corresponds to the statistical percentile accepted by current codes [NTC 2018].

The same general trend can be observed for both sites, where the number of failures reduces as the design code comes closer to the current one. For Naples cases, the EDP limit is attained for higher seismic intensities, this effect is due to the lower seismic hazard of the site. In the UPD case, all retrofitted buildings succeed in matching the current codes requirements, showing how the base isolation technique successfully manages to preserve the integrity of non-structural elements. It has to be noticed how Naples cases present a much more different seismic performance in the two horizontal directions than L'Aquila cases. This particular behaviour is probably linked to the difference in horizontal stiffness between the two directions, strongly influenced by beams directions (see Figure 5.2).

In conclusion, results show the isolation systems efficiency in limiting non-structural damage for seismic intensities even higher than the design one and also point out their little margin toward collapse for these intensity levels. The following main considerations can be made:

- In cases of retrofitted buildings, the UPD superstructure failure has shown to be the main failure mode, especially for the case of buildings designed without seismic rules due to the deformability of the structure;
- For the GC, differently, the isolation system failure has always preceded superstructural one for both new and existing base-isolated buildings mainly due to the generally low design margin of isolation devices;
- The influence of different procedures assumed for the design of seismic isolators for new and existing buildings is negligible.
- The probability of reaching the GC limit state significantly reduces when over-stroke capacity is considered, this result is particularly relevant if compared with the results

obtained in other works considering the unlimited elasto-plastic behaviour modelling of isolation systems,

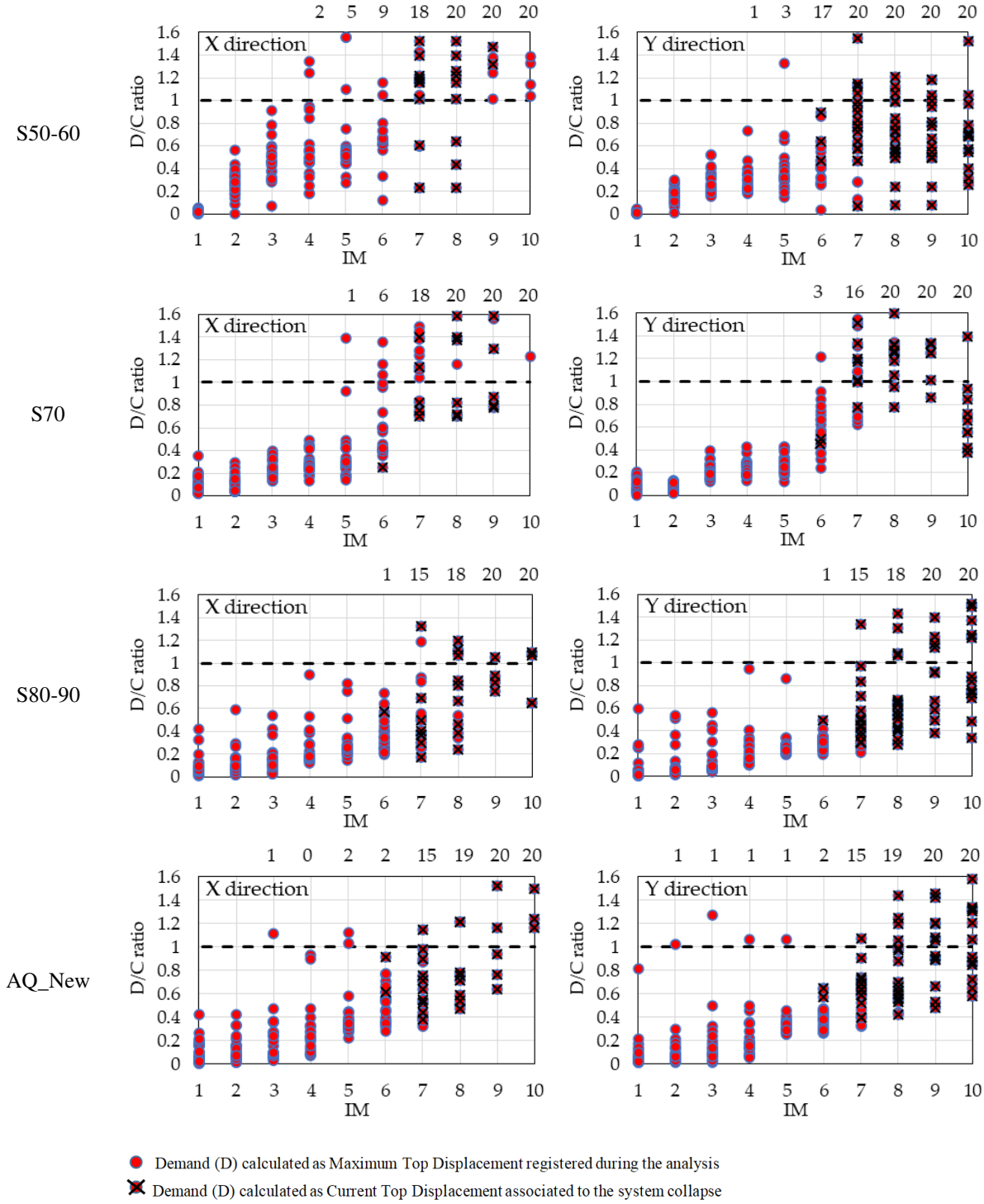

Figure 5.13. Displacement D/C ratios of the superstructure (UPD): L'Aquila cases X and Y directions.

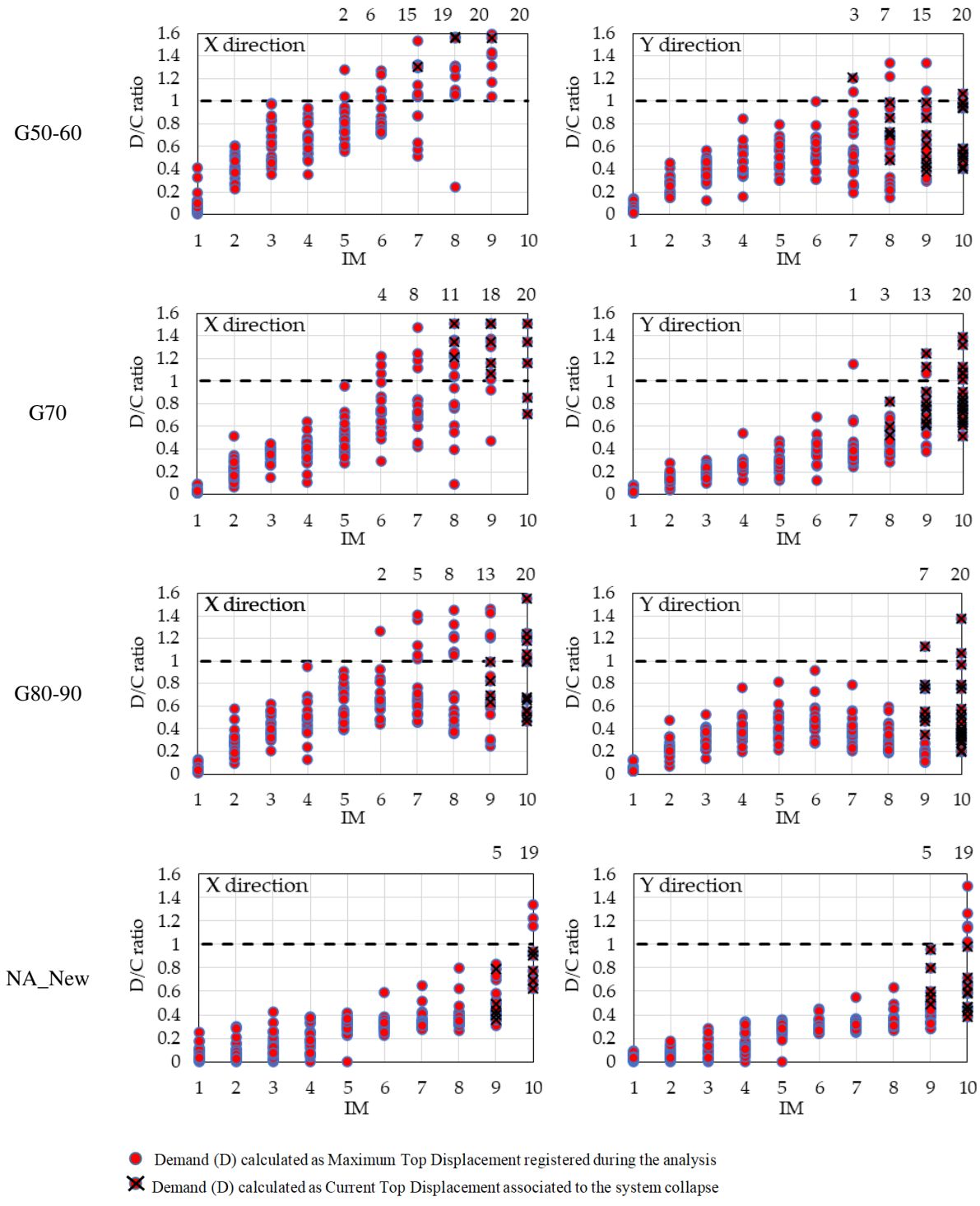

Figure 5.14. Displacement D/C ratios of the superstructure (UPD): Naples cases X and Y directions.

5.4.1 Fragility curves

Results are here presented in terms of fragility curves of UPD leading the superstructure to the drift limit and GC reaching the limit displacement of DCCSS isolators.

Figure 5.15 shows the comparison of the fragility curves evaluated for all the case studies in order to provide a prediction of potential damage during an earthquake higher than the CLS (corresponding to IM6) for the base isolated models. The UPD curves confirm that seismic isolation works effectively in limiting damage on non-structural components for seismic intensities much higher than the design earthquake intensity level DLS (corresponding to IM2). Due to the extra displacement capacity gained in the over-stroke regime, for the "AQ_New" base-isolated building the GC curve associated to the attainment of the DCCSS limit displacement appears almost identical to UPD curve, while, for Naples case "NA_New" they are completely overalpped. For the retrofitted base isolated building the superstructure failure becomes more significant, UPD fragility are characterized by higher probabilities of exceeding for the same seismic intensities, mainly due to the higher deformability of the superstructure. The general trend is in good agreement with results previousely exposed, showing a UPD failure probability which is higher for older buildings and smaller for newer ones. For the GC limit state the trend is the same but is characterized by smaller differences between construction ages. Fragility curves parameters are shown in Table 5.6 in terms of Median (acceleration corresponding to 50% of probability of exceeding the limit of the considered EDP) and log-standard deviation derived adopting the Maximum Likelihood regression method. A final comparison between all case studies fragility curves divided for Limit State and Site, is shown in Figure 5.16.

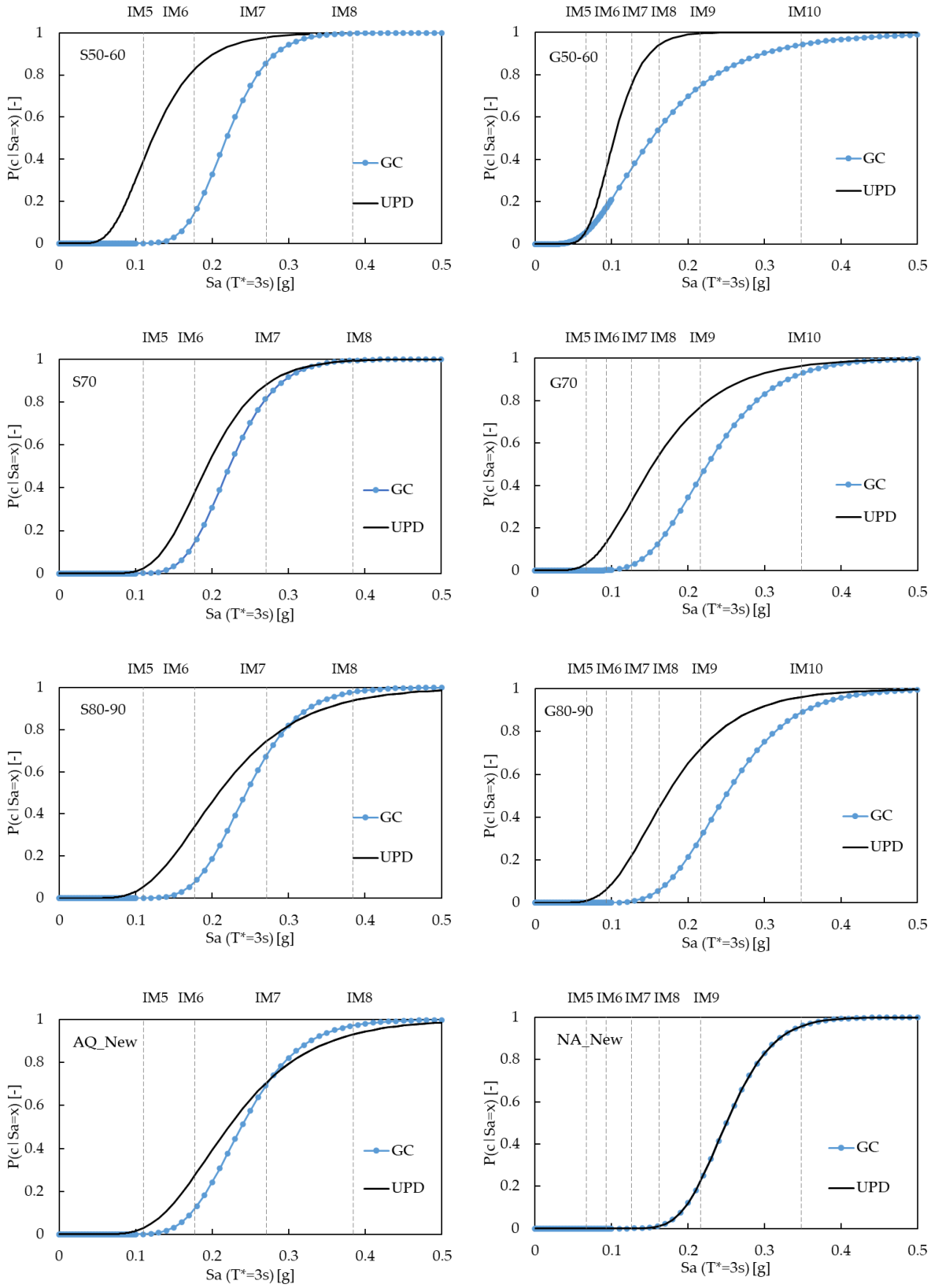

Figure 5.15. Fragility curves for GC and UPD limit states for all the analysed case studies.

Table 5.6 Fragility curves results parameters

Case study	*Limit State*	*Median* θ	*Standard Deviation* β
S50-60	UPD	0.122	0.392
	GC	0.219	0.200
S70	UPD	0.194	0.283
	GC	0.223	0.215
S80-90	UPD	0.122	0.392
	GC	0.219	0.200
AQ_New	UPD	0.194	0.283
	GC	0.223	0.215
G50-60	UPD	0.103	0.287
	GC	0.152	0.525
G70	UPD	0.103	0.287
	GC	0.152	0.525
G80-90	UPD	0.171	0.399
	GC	0.249	0.275
NA_New	UPD	0.240	0.175
	GC	0.250	0.190

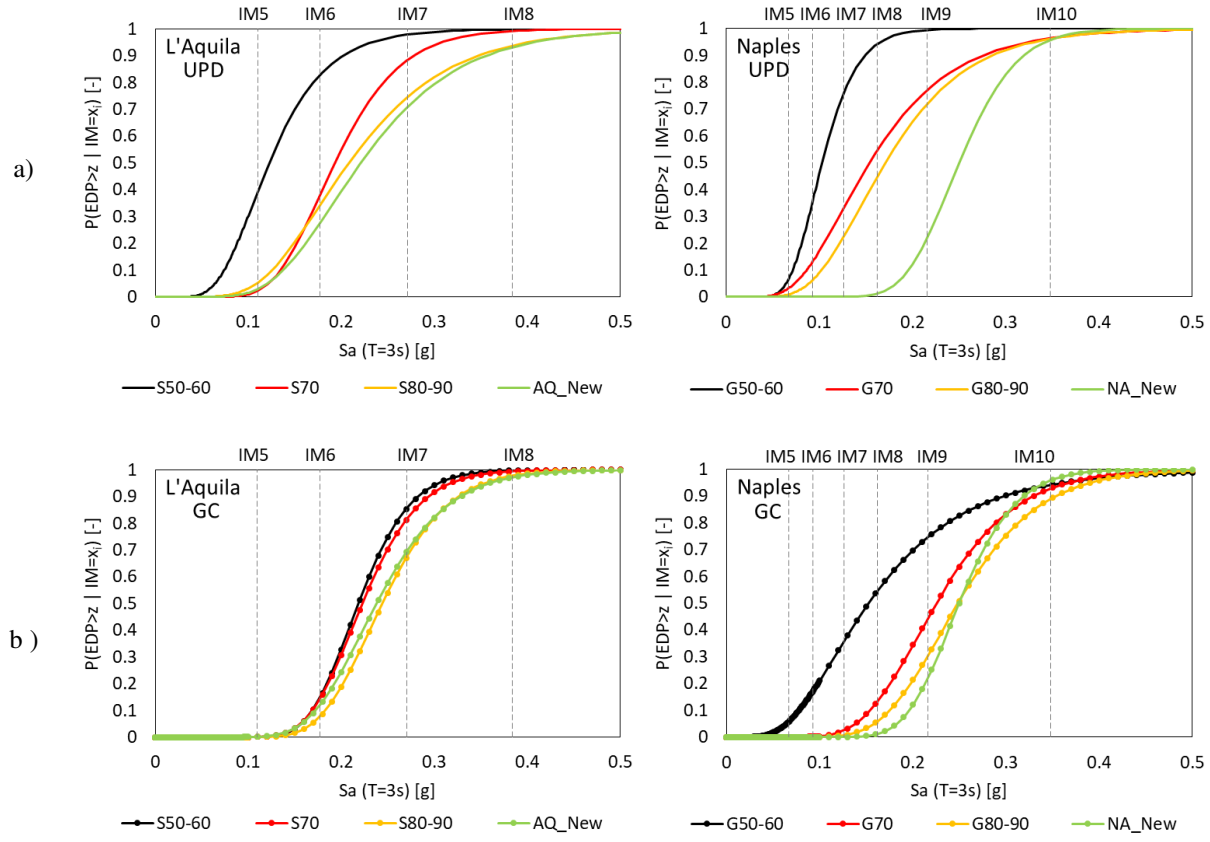

Figure 5.16. Fragility curves for a) UPD and b) GC limit states for all the analysed case studies.

5.4.2 Annual frequency of exceedance

Mean Annual Frequencies of exceedance have been computed to account for the local seismic hazard of the sites of L'Aquila and Naples respectively. Figure 5.17 shows how the general trend highlighted by fragility curves can also be observed for Mean Annual Frequencies of Exceedance. For the sake of legibility, EDP limits have been reported in Figure 5.17 in a compact representation, showing, for the UPD Limit State a mean value of Drift around $\approx$ 0.35%, and for Naples around $\approx 0.25\%$ (d_{top} values in Table 5.5 divided by the structural height $H_{tot} = 18.65m$), and for the GC a single vertical dashed line when the EDP limit values are about the same.

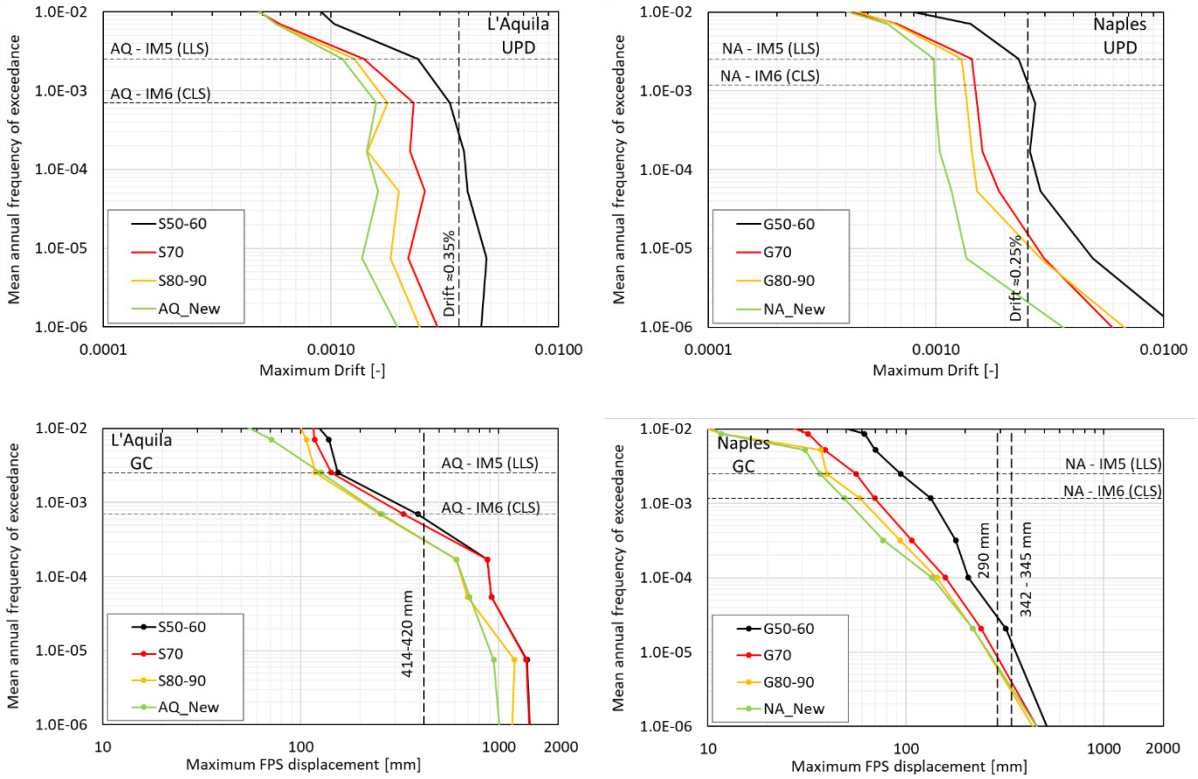

Figure 5.17. Mean annual frequencies of exceeding for the UPD and the GC for all the analysed case studies.

5.4.3 Annual Rates of Failure

Finally annual rates of failure have been computed for all case studies using the R2R Tool [Baraschino et al., 2020] which follows the mathematical procedure illustrated in the relevant section of the present dissertation.

The Annual Rates of Failure are presented in terms of UPD leading the superstructure to the drift limit and GC reaching the limit displacement of DCCSS isolators. Figure 5.18 shows the comparison of the mean annual rates evaluated for all the case studies for the GC (a) and the UPD (b) performance levels, to provide a prediction of potential damage during an earthquake higher than the CLS (corresponding to IM6) for the base-isolated models. Dashed horizontal lines highlight the reference probabilities of exceedance provided by the Italian seismic code NTC18 [NTC 2018], i.e., 1.00×10^{-3} for GC and 1.26×10^{-2} for UPD.

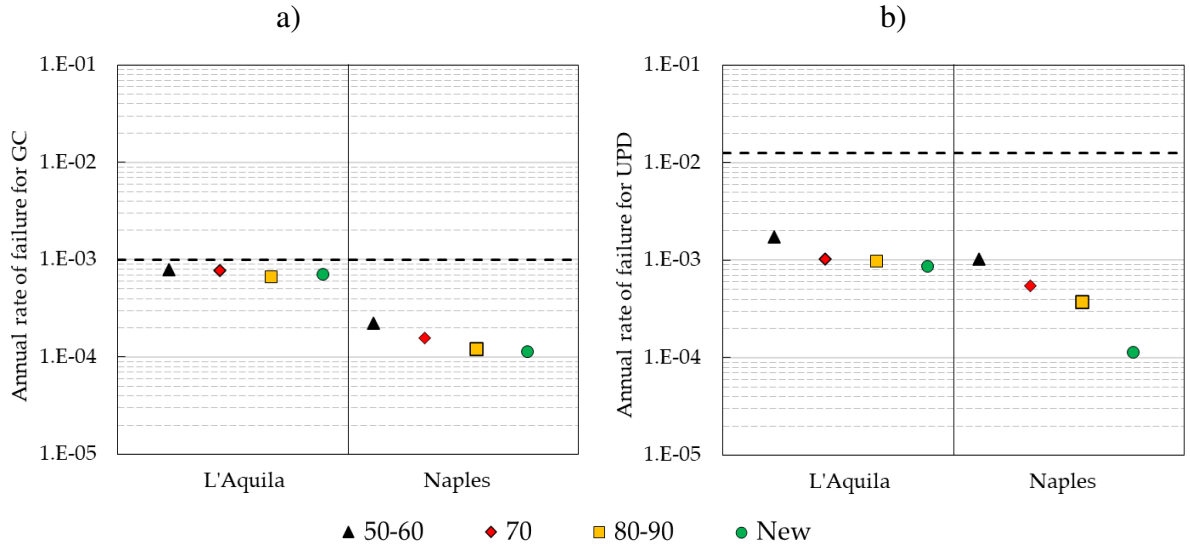

Figure 5.18. Annual rates of failure for the analysed base-isolated case studies, for the GC (a) and the UPD (b) performance levels.

Due to the extra displacement capacity gained in the over-stroke regime, for the AQ_New base-isolated building the GC rates associated with the attainment of the DCCSS limit displacement appear almost identical to UPD ones, and are the same values for the NA_New case. For the

retrofitted base-isolated building (*50-60*, *70*, *80-90* both SLD and GLD) the superstructure failure becomes more significant, UPD rates are linked to higher probabilities of exceeding than the GC ones, mainly due to the higher deformability of the superstructure. The values of the annual rates of failure derived at UPD and GC limit states for the examined case studies are reported in Table 5.7. Few differences between values for both the UPD and the GC can be observed for L'Aquila cases showing how superstructural differences have a negligible influence onto isolation systems collapse, while their performance still affects the UPD limit state attainment. For Naples cases, superstructures have limited influence in the GC attainmente while they play a crucial role in terms of UPD damage, where significantly higher annual rates of failure can be observed for older superstructures.

Table 5.7 Annual rates of failure for the analysed cases.

Case ID	*Limit State*	*Annual Rate of Failure* λ_f
S50-60	UPD	1.745E-03
	GC	7.946E-04
S70	UPD	1.021E-03
	GC	7.746E-04
S80-90	UPD	9.802E-04
	GC	6.633E-04
AQ_New	UPD	8.703E-04
	GC	7.052E-04
G50-60	UPD	1.039E-03
	GC	2.243E-04
G70	UPD	5.416E-04
	GC	1.568E-04
G80-90	UPD	3.755E-04
	GC	1.233E-04
NA_New	UPD	1.137E-04
	GC	1.138E-04

6 Retaining elements influence on structural seismic performance

As previously discussed, DCCSSs implementing low-friction sliding materials has been proven to be an effective solution for the protection of strategic buildings, like hospitals, that are characterized by a significant presence of non-structural components and valuable technological content [Gandelli et al., 2018]. However, this solution usually results in large displacements of the isolation system that, in some cases, cannot be accepted due to the presence of architectural constraints. The use of auxiliary devices could be relevant in order to reduce the maximum displacement of the isolation system. While the performance of DCCSS has been widely validated under different levels of ground motion, there have been very few experimental studies on these devices behavior when the displacement limit is reached. Recent studies consider the isolation system failure that may occur when the actual isolator displacement capacity d_c is exceeded, such as when earthquakes stronger than the design one happen [Kitayama and Constantinou, 2018] [Kitayama and Constantinou, 2019b]. Such studies discuss the significance of the stiffening behavior of the patented Triple pendulum isolators, showing a failure condition similar to DCCSSs when the inner slider exceeds the displacement capacity [Sarlis and Constantinou, 2013].

Recent shake table test campaigns described in [Bao et al., 2018] [Furinghetti et al., 2020] [Yang 2020] have been conducted to analyse the isolators behaviour beyond their geometrical displacement capacity. Bao, Becker et. al [Bao et al., 2018a] using 1:3.5 scaled DCCSS, demonstrated that restraining rim bearings have a strong influence on the structural behavior while flat rim bearings were associated with the lowest values of peak axial forces, shear forces and floor response spectra among four types of tested specimens. In [Yang 2020] details of different failure conditions are described, even though the tested scaled bearings have limited strength. Results also show how flat rim scaled specimens can achieve displacements up to 155% of their own nominal capacity before damaging and becoming non-functional. Bao,

Becker et al. in 2018 [Bao and Becker, 2018] [Bao et al., 2018b] analysed a moment resistant frame and a braced frame under extreme conditions, both isolated with sliding bearings in the configuration with and without restraining ring. Results are then compared and show a larger collapse margin ratio in both the configurations without restraining rings having a consistent improvement in the structure resilience, especially for the braced frame. Similarly, Yang [Yang, 2020] and Furinghetti [Furinghetti et al., 2020] have conducted experimental tests on a series of full-scale DCCSS bearings, commonly used in Europe, under several input motions and have proposed a numerical model representing the device behavior when displacements exceeding the maximum displacement capacity are reached. Results show how the over-stroke behaviour is affected by the sliding material and the manufacturing of the housing plate border. Accurate studies to assess the consequences of impacts on the superstructure of seismically isolated buildings under strong ground motions, including pounding against a flexible moat wall, were carried out by [Masroor and Mosqueda, 2012] [Masroor and Mosqueda, 2013] [Ragni et al., 2018].

In this section, the resilience of DCCSS isolated buildings with and without over-stroke displacement and with and without retaining elements is analysed. The effects of the over-stroke displacement and the presence of retaining elements on isolated structures have been investigated considering two simple bi-dimensional frames as case studies of residential use buildings.

6.1 Case studies

The assessment of the influence of isolation system displacement retaining elements is based on the study of two bi-dimensional Moment Resistant bare Frames (MRF) as shown in Figure 6.1.

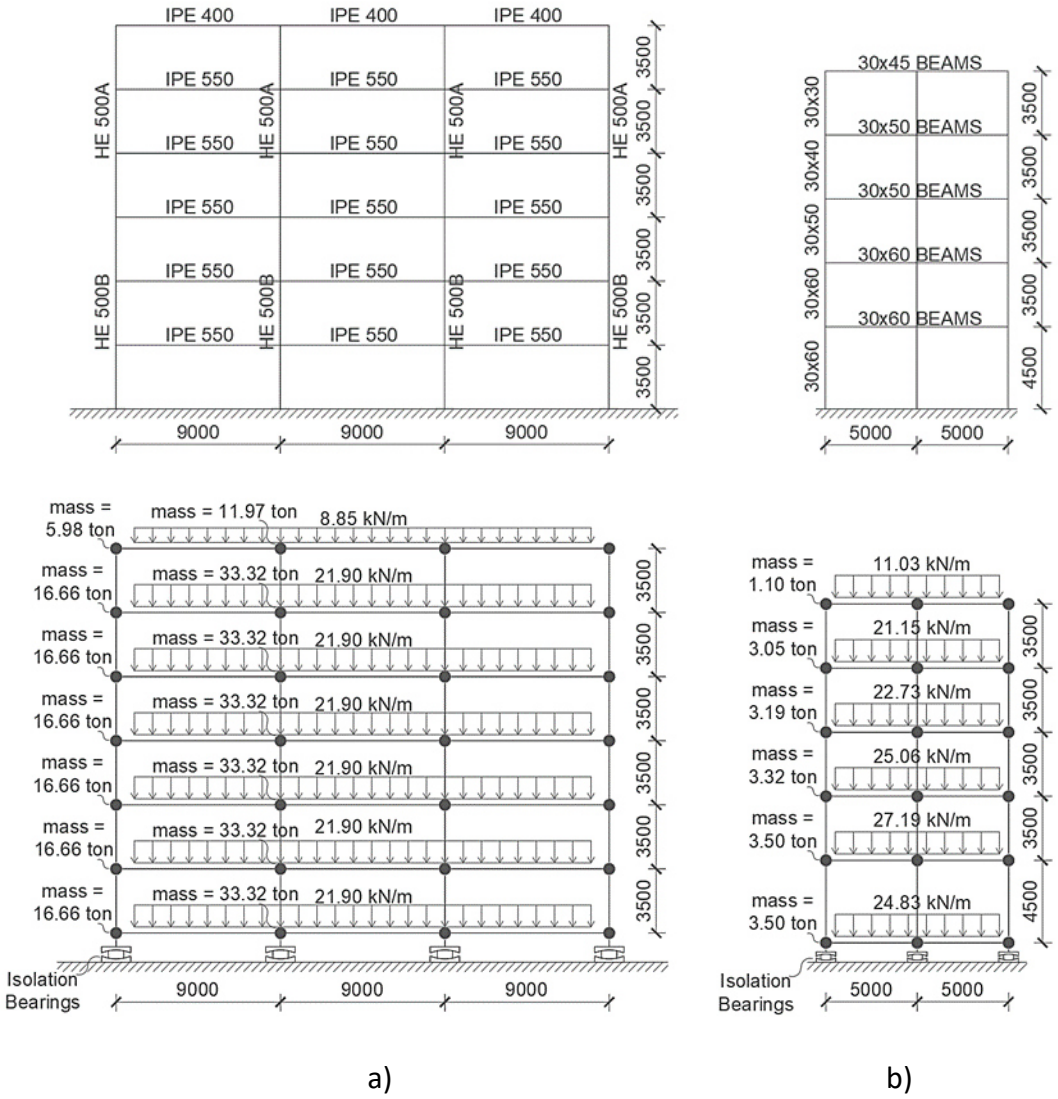

Figure 6.1. a) Steel and b) Reinforced Concrete MRF structural elements of the fixed-base superstructures and representation of gravity loads for in the base-isolated configuration.

One is a 6-story steel 2D Moment Resistant Frame (MRF), considered as a case study in [Kitayama and Constantinou, 2019b], [Ponzo et al., 2020] and [Di Cesare et al., 2021] designed according to the Italian seismic code NTC18 [NTC 2018].

The second one is the prototype of a 5-story reinforced concrete (RC) moment resistant 2D frame considered as a case study in [Mazza and Vulcano, 2012] and [Ponzo et al., 2020], designed according to Eurocode 8 [CEN, Eurocode 8 – Part 1, 2004] and satisfying prescriptions imposed by NTC08 [NTC 2018].

6.1.1 Modelling

Both structures, classified as ordinary with an importance factor $c_u = 1$, have been designed for a location in the city of L'Aquila, central Italy, and medium soil class C. Beam and Column elements have been modelled with a lumped plasticity approach for the superstructure, whereas elastic beams have been used for the base floor grid above the isolation system. For the Steel Frame, member capacities have been calculated using the expected yield strength of the steel material 275 MPa and panel zones have been modelled with rigid-elastic elements by using a *TwoNodeLink* element with length equal to half of the section depth as shown in Figure 6.2a. For the RC Frame model, plastic hinges in the joints have been represented using *zero-length TwoNodeLink* elements as shown in Figure 6.2b. Second order effects have not been taken into account. For both structures, the modified Ibarra-Medina-Krawinkler deterioration model (IMK) [Ibarra et al., 2005] calibrated on the basis of more than 350 experimental data of steel beam-to-column connections has been used for plastic hinges modelling. The model parameters are the effective yield strength and rotation (M_y and θ_y) and the effective stiffness $K_e = M_y/\theta_y$, the capping strength and the associated rotation for monotonic loading M_c and θ_c, the pre-capping, the post-capping and the ultimate rotational capacities θ_p, θ_{pc} and θ_u, and the residual strength $M_r = \kappa\, M_y$ (see Figure 6.2c).

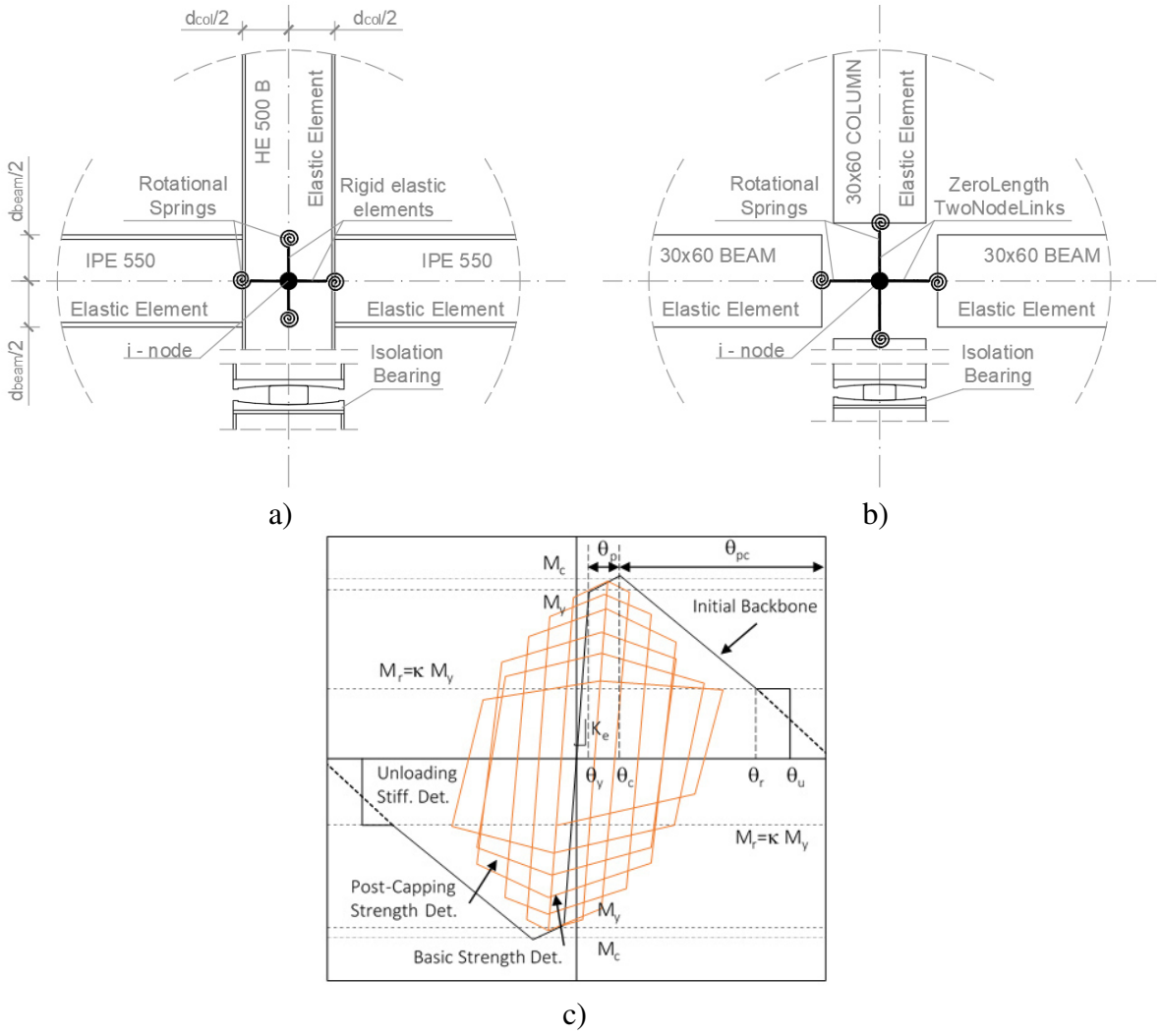

Figure 6.2. Model of beam-column joints of the superstructure of the a) Steel MRF and the b) RC MRF case studies; c) cyclic deterioration of the IMK model

The Steel Moment Resistant bare Frame (MRF) has been designed for gravity loads only respecting minimum criteria required by Eurocode and considering low ductility class for structural details. Seismic weights W_i and masses M_i of each floor, are listed in Table 6.1. The total seismic weight W of the base-isolated frame is about $5000kN$ and the vertical load on the internal isolators is $N_{Sd} = 1680kN$.

The Reinforced Concrete case study, analysed, as well as the Steel-MRF, in the configuration of Bare Frame (BF), has been designed according to Eurocode 8 assuming the gravity loads

combined with either the horizontal seismic loads or the horizontal and vertical seismic loads. A grid of beams is modelled at the base of the superstructure on the DCCSS layer. The seismic weights W_i and masses M_i of each floor, are listed in Table 6.1 and summarized in Figure 6.1. The total seismic weight W of the base-isolated frame is about $1320kN$ and the vertical load on the internal isolator is $N_{Sd} = 670kN$.

Table 6.1 Gravity and seismic loads and masses of the moment resistant steel frame.

Floor	*STEEL*		*RC*	
	Weighs W_i [kN]	*Masses M_i [ton]*	*Weighs W_i [kN]*	*Masses M_i [ton]*
Base	970	99	248	25.3
1st	980	100	272	27.7
2nd	980	100	251	25.5
3rd	980	100	227	23.2
4th	980	100	212	21.6
5th	980	100	110	11.2
6th	350	36	-	-
Total	*6220*	*634*	*1320*	*135*

The superstructure stiffness, in the not-isolated configuration, has been computed using the information gained by linear-dynamic analyses about the mass participation factors in the first vibration mode. The single structural element stiffness has been considered in a "shear-type" configuration, and, for floor stiffness, all structural elements were considered in parallel, the first vibration period T and the superstructure stiffness K_{str} are listed in Table 6.2.

Table 6.2 Superstructures main period and global stiffness.

BF Model	***T [s]***	***K_{str} [kN/mm]***
Steel Frame	0.78	1165
RC Frame	0.43	368

6.1.2 Isolation system design

The isolation system consists of DCCSS isolators placed below each column. Isolation systems have been designed using the CLS ξ_{eff} damped spectrum according to the Italian seismic code [NTC 18] for the location of the city of L'Aquila, central Italy, and medium soil class C as shown in Figure 6.4.

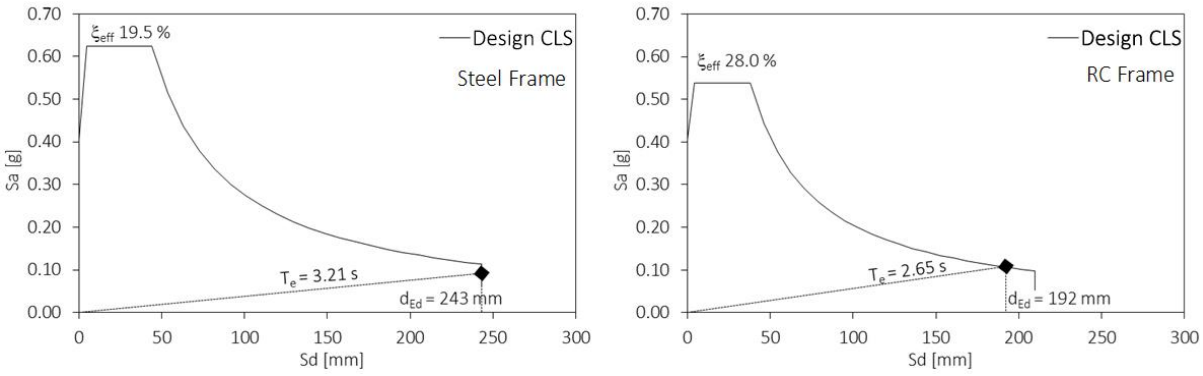

a) b)

Figure 6.3. Design of isolation systems for the Steel Frame (a) and the reinforced Concrete Frame (b).

Considering the discretization of geometrical dimensions of commercial bearings, a maximum displacement capacity $d_c > d_{Ed}$ has been chosen, design parameters of the isolation system are reported in Table 6.3.

Table 6.3 Isolation system design parameters.

BI Model	R_e [mm]	N_{sd} [kN]	N_{Ed} [kN]	μ [%]	K_i [kN/m]	K_e [kN/m]	T_e [s]	ξ_{eff} [%]	d_{Ed} [mm]	d_c [mm]
Steel frame	3700	2080	2500	2.9	5000	653	3.21	19.5	243	± 300
RC Frame	3100	670	1000	2.5	5000	261	2.65	28	208	± 250

6.2 Seismic input

In order to adequately reproduce the behaviour of the isolation system in the actual range of deformations and velocities, the seismic response of base isolated models has been evaluated by means of nonlinear time-history analyses. According to the PEER-like modular approach and performance-based earthquake engineering (PBEE) approach [Porter, 2003], the study here focused on the estimation of the effects of displacement restrainers on base isolated structures by considering several real ground motions and adopting appropriate intensity measures (IM). The record-to-record variability is taken into account through two sets of 200 natural seismic records (composed of 20 sets of motions for the 10 selected intensities each) selected from national and international databases supported by the assessment of the ground motion hazard at the site of L'Aquila (Italian site) as described before. The Intensity Measure (IM) selected to represent the earthquake intensity levels is the spectral acceleration (5%-damped) corresponding to a reference period (conditioning period) chosen as close as possible to the design value of the fundamental period of vibration of T = 3 sec for the base-isolated structures, of T = 1 sec for the not-isolated steel frame and of T = 0.5 sec for the not-isolated RC-frame (see Table 6.4).

Table 6.4 Return Periods T_R [y] and Spectral acceleration $S_a(T)$ expressed in [g] for chosen IMs.

Case	***Intensity Measure (IM)***	***1***	***2***	***3***	***4***	***5***	***6***	***7***	***8***	***9***	***10***
			(DLS)			*(LLS)*	*(CLS)*				
	T_R [y]	***10***	***50***	***100***	***250***	***500***	***1,000***	***2,500***	***5,000***	***10,000***	***100,000***
RC	*S_a(T=0.5s) [g]*	0.077	0.181	0.322	0.503	**0.754**	1.129	1.733	2.481	3.810	7.639
Steel	*S_a(T=1s) [g]*	0.029	0.073	0.139	0.232	**0.365**	0.558	0.855	1.217	1.837	3.520
Base Isolated	*S_a(T=3s) [g]*	0.0002	0.011	0.031	0.062	0.110	**0.177**	0.271	0.384	0.576	1.053

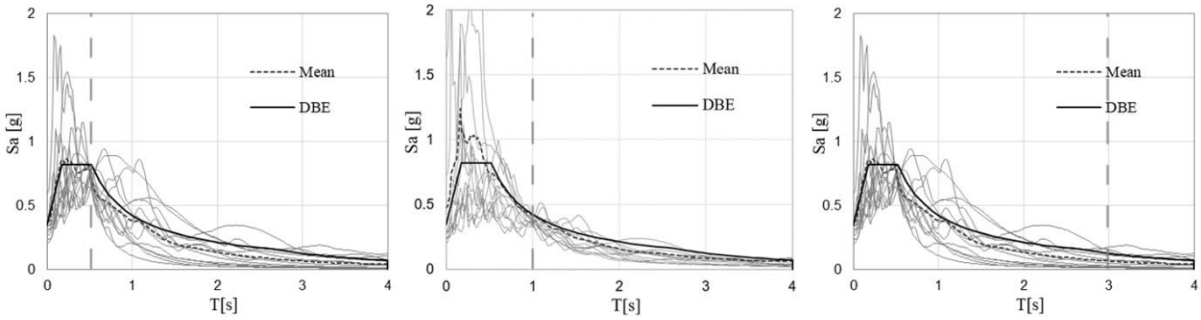

Figure 6.4. Elastic response spectra of seismic inputs fitted for a) T=0.5sec, b) T=1.0sec and c) T=3.0 sec.

As an example, the elastic spectra of 20 seismic inputs for the intensity measure level IM6 corresponding to the isolated structures CLS (corresponding to the so-called Maximum Considered Earthquake (MCE) for Eurocode 8 [CEN, Eurocode 8 – Part 1 2004]) is reported in Figure 6.4c and for the intensity measure level IM5 corresponding to not-isolated models LLS (corresponding to the so-called Design Basis Earthquake (DBE) for Eurocode 8) are reported in Figure 6.4a and b. The earthquake vertical component has been neglected in all analyses.

6.3 Unlimited stiffness retaining elements - Parametric Analysis

A first parametric analysis has been performed onto the Steel MRF base-isolated structure considering retaining elements with unlimited stiffness and four basic model types for the DCCSS bearing behaviour, with and without over-stroke effects and end stops in the configurations:

a) basic isolation model (*SingleFPBearing* Table 3.3) with displacement capacity $d_c = 1.25$ and unlimited elasto-plastic behavior (Case ID "BI 1.25");
b) the previous isolation model with restraining ring (*Ring_DCCSS* Table 3.3) (Case ID "BI 1.25_Stop");
c) basic isolation model with over-stroke displacement (*OS_DCCSS* Table 3.3) $d_{lim} = 2.00\ d_c$ and unlimited elasto-plastic behavior (Case ID "BI 1.25_Over-Stroke");
d) the previous isolation model with retaining wall (*Wall_DCCSS* Table 3.3) (Case ID "BI 1.25_Over-Stroke_2.00_Stop").

The parametric analysis has been carried out considering the following deterministic parameters with appropriate ranges of variation: the isolation capacity displacement d_c compared to the seismic maximum displacement d_{Ed} varying their ratio from 1 to 1.50; the limit displacement d_{lim} varying the d_{lim}/d_c ratio from 1.25 to 2.00; the presence of the seismic stopper in both the Base Isolated (BI) and the Base Isolated with Over-Stroke (BI – OS) models. It derives that thirty 2D systems have been properly defined, Table 6.5 shows the cases ID and the corresponding base displacement limit.

Table 6.5 Isolation system models and maximum base displacement considered.

d_c / d_{Ed}	d_{lim} / d_c	end-stop	OpenSEES model (from Table 3.3)	Case ID	*Displacement limit [mm]*
1.00	1.00	w/o	*SingleFPBearing*	*BI 1.00*	*243.0*
		with	*Ring_DCCSS*	*BI 1.00_Stop*	*243.0*
	1.25	w/o	*OS_DCCSS*	*BI 1.00_Over-Stroke 1.25*	*303.8*
		with	*Wall_DCCSS*	*BI 1.00_Over-Stroke*	*303.8*
	1.50	w/o	*OS_DCCSS*	*BI 1.00_Over-Stroke 1.50*	*364.5*
		with	*Wall_DCCSS*	*BI 1.00_Over-Stroke*	*364.5*
	1.75	w/o	*OS_DCCSS*	*BI 1.00_Over-Stroke 1.75*	*425.3*
		with	*Wall_DCCSS*	*BI 1.00_Over-Stroke*	*425.3*
	2.00	w/o	*OS_DCCSS*	*BI 1.00_Over-Stroke 2.00*	*486.0*
		with	*Wall_DCCSS*	*BI 1.00_Over-Stroke*	*486.0*
1.25	1.00	w/o	*SingleFPBearing*	*BI 1.25*	*303.8*
		with	*Ring_DCCSS*	*BI 1.25_Stop*	*303.8*
	1.25	w/o	*OS_DCCSS*	*BI 1.25_Over-Stroke 1.25*	*379.7*
		with	*Wall_DCCSS*	*BI 1.25_Over-Stroke*	*379.7*
	1.50	w/o	*OS_DCCSS*	*BI 1.25_Over-Stroke 1.50*	*455.6*
		with	*Wall_DCCSS*	*BI 1.25_Over-Stroke*	*455.6*
	1.75	w/o	*OS_DCCSS*	*BI 1.25_Over-Stroke 1.75*	*531.6*
		with	*Wall_DCCSS*	*BI 1.25_Over-Stroke*	*531.6*
	2.00	w/o	*OS_DCCSS*	*BI 1.25_Over-Stroke 2.00*	*607.5*
		with	*Wall_DCCSS*	*BI 1.25_Over-Stroke*	*607.5*
1.50	1.00	w/o	*SingleFPBearing*	*BI 1.50*	*364.5*
		with	*Ring_DCCSS*	*BI 1.50_Stop*	*364.5*
	1.25	w/o	*OS_DCCSS*	*BI 1.50_Over-Stroke 1.25*	*455.6*
		with	*Wall_DCCSS*	*BI 1.50_Over-Stroke*	*455.6*
	1.50	w/o	*OS_DCCSS*	*BI 1.50_Over-Stroke 1.50*	*546.8*
		with	*Wall_DCCSS*	*BI 1.50_Over-Stroke*	*546.8*
	1.75	w/o	*OS_DCCSS*	*BI 1.50_Over-Stroke 1.75*	*637.9*
		with	*Wall_DCCSS*	*BI 1.50_Over-Stroke*	*637.9*
	2.00	w/o	*OS_DCCSS*	*BI 1.50_Over-Stroke 2.00*	*729.0*
		with	*Wall_DCCSS*	*BI 1.50_Over-Stroke*	*729.0*

6.3.1 Nonlinear Static Analyses

Non-linear static (Pushover) analyses have been carried out as described by codes [FEMA P-695, 2009], [FEMA-356, 2000] and in the studies of [Kitayama and Constantinou, 2018], [Ponzo et al., 2020], [Di Cesare et al., 2021]. Some examples of pushover curves for the thirty case studies of base isolated frames and the not-isolated frame case are presented in Figure 6.5. A distribution of lateral forces proportional to the floor masses has been used in the analyses. The red circled point at the global drift ratio (Roof displacement/Height) of 1% is the yield drift

of the not-isolated frame (black line) corresponding to the end of the elastic branch. The red dashed line in pushover curves of base isolated frames show the base shear of 1915 kN corresponding to the superstructure global drift of 1% as well. Pushover curves of isolated buildings show a reduction of the maximum base-shear force after the elastic branch (see Figure 6.5) due to the flexural deformability of the base beam layer added to base isolated "BI" models.

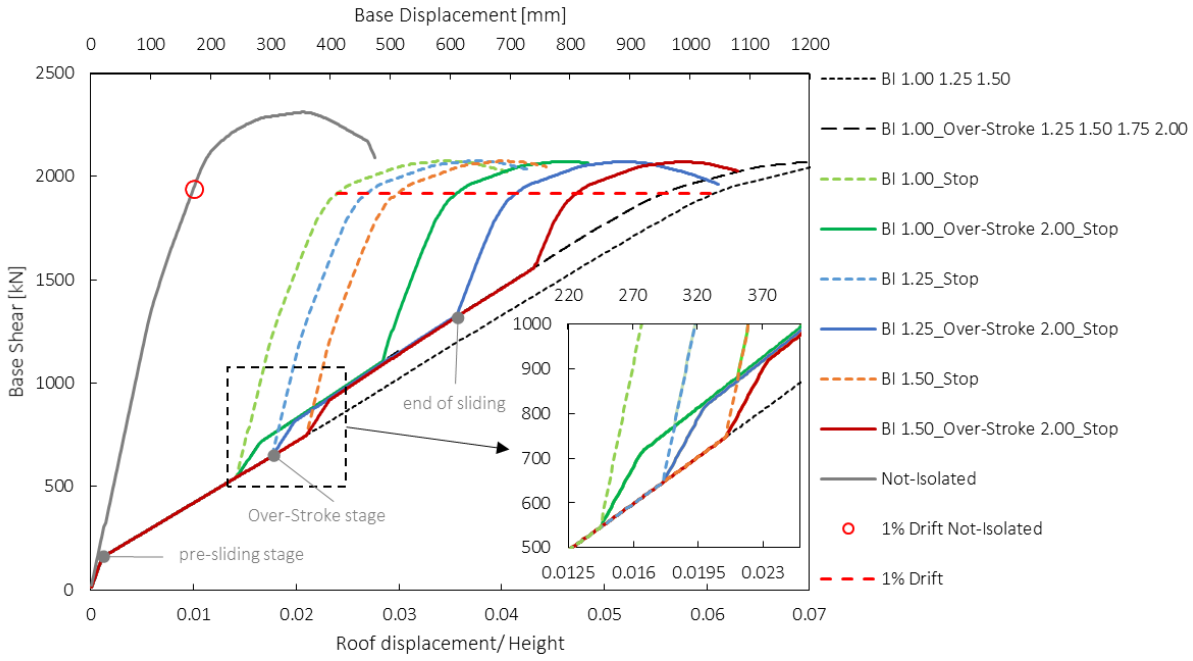

Figure 6.5. Pushover curves of fixed base model and of representative cases of isolation systems.

The pushover curve of the case featuring isolators with unlimited stroke displacement (*SingleFPBearing* model) ($d_c/d_{Ed} = 1.00, 1.25, 1.50$), denoted as Case ID "BI 1.00_1.25_1.50" (black dotted line) shows the basic behaviour. The pushover curve of isolators with unlimited over-stroke displacement (*OS_DCCSS* model) ($d_u/d_c = 1.25, 1.50, 1.75, 2.00$), denoted as Case ID "BI 1.00_Overstroke 1.25_1.50_1.75_2.00" (black dashed line) shows the modified behaviour of isolators beyond the isolator end-stroke.

A brief description of Figure 6.5 is here given providing two characteristic pushover examples. The isolation system model with geometric displacement capacity $d_c/d_{Ed} = 1.25$ and with

restraining ring at $d_{lim}/d_c = 1$, denoted as Case ID "BI 1.25_Stop" (blue dashed line), shows a first branch characterized by the isolators quasi-rigid behaviour (pre-sliding stage), then a second branch primarily accounting for isolators restoring stiffness, finally, when the base displacement reaches d_c, the curve shows a superstructural response similar to that of the not-isolated frame. The isolation system model with geometric displacement capacity $d_c/d_{Ed} = 1.25$, with over-stroke displacement capacity $d_{lim}/d_c = 2.00$ and end-over-stroke, denoted as Case ID "BI 1.25_Over-Stroke 2.00_Stop" (dark blue curve), perfectly overlaps the previous one for the first two branches, then, when the geometric capacity displacement is reached, the isolation system enters in the over-stroke stage (see zooming box in Figure 6.5) with a third branch with increased stiffness and friction force, and finally, when the end-over-stroke is reached (end of sliding), the superstructure pushover curve is shown again. For this Case ID, the different transitional stages of motion have been labelled in Figure 6.5.

The possibility to perform nonlinear static pushover analyses on base-isolated structures is granted by [FEMA P-695, 2009], [FEMA-356, 2000]. It is possible to observe that the shape of the pushover curve of isolated structures cannot be approximated by an elastoplastic representation. This means that pushover curves could not always be used in the application of the simplified procedure for spectral shape effect estimation. Base-isolated models with end stops assume that shear forces of retaining elements are consistent with the superstructure strength.

6.3.2 Nonlinear Time History Analyses

As previously discussed, a set of accelerograms organized in 20 bidirectional records for 10 Intensity Measures have been used to perform 200 NTHA on each of the 30 models presented in Table 6.5, for a total number of 6000 analyses within the parametric study. The Engineering

Demand Parameters (EDPs) chosen for the superstructure are the global drift limit of 1% and the base shear limit of 1915 kN (corresponding to a 1% drift) (see Figure 6.5).

Such a complex parametric analysis required an effective and clear exposition of results, capable of providing a global glance on numerical outcomes tendencies. For this scope, results have been processed using fragility curves.

6.3.3 Fragility curves

Fragility curves are established to provide a prediction of potential damage during an earthquake higher than the CLS (corresponding to IM6) for the base-isolated models. Figure 6.6a show fragility curves for the superstructure drift that exceed the drift limit 1% for base-isolated cases. For high-intensity ground motions levels, the presence of the isolator displacement retaining element has proven to have a strong influence on the performance of the superstructure, when end stops are present, the over-stroke capacity increases the seismic performance of the superstructure. Figure 6.6b show fragility curves for the superstructure base shear when exceeding the limit corresponding to the superstructure yield drift for all isolation system cases.

The influence of seismic stops is well shown in Figure 6.6 where models without stop (black dashed lines) always turn out to have a probability of exceedance lower than all models with retaining elements (end stops). As an example, the superstructure presents 55% probability of exceeding the drift limit for IM8 (middle diagram of Figure 6.6a) in the case of the model without over-stroke “BI 1.25_Stop” (blue dashed line) and 25% probability for the same intensity measure in the case of the model with maximum over-stroke capacity “BI 1.25_Over-Stroke 2.00_Stop” (dark blue line).

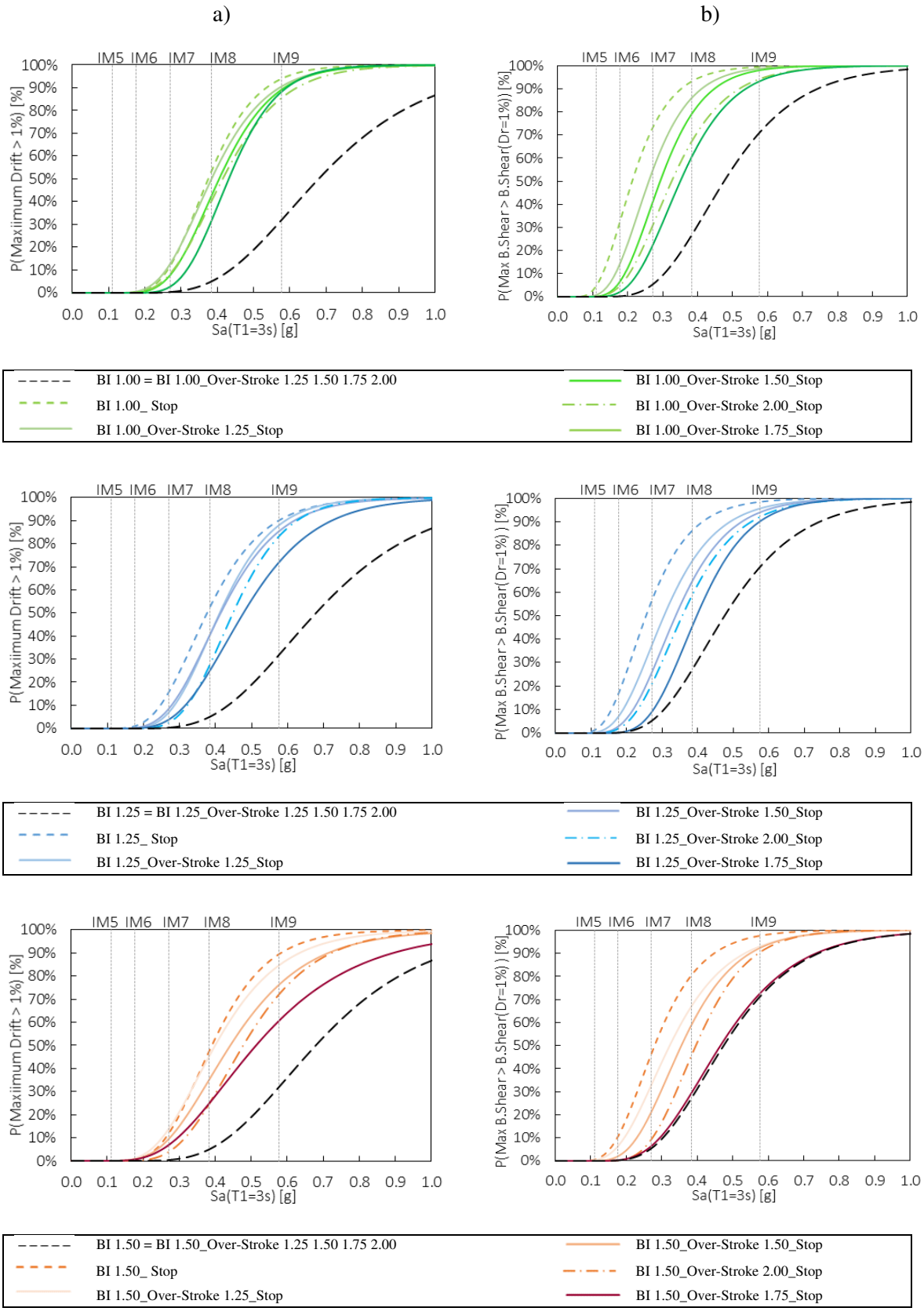

Figure 6.6. Fragility Curves for a) the superstructure drift limit and b) the base shear limit.

This gap grows larger by increasing the d_c/d_{Ed} ratio (lower diagram of Figure 6.6a) and reduces when the d_c/d_{Ed} ratio decreases (top diagram of Figure 6.6a), pointing out the retaining elements strong influence on the superstructure seismic response. Figure 6.6b shows that the base shear limit has the same general trend with higher values of exceeding probabilities than the drift limit.

Borderline fragility curves for the superstructure drift and base shear (EDPs) are shown in Figure 6.7 considering the lower and upper bound models. In Figure 6.7a, superstructure drift fragility curves comparison highlights how the over-stroke capacity (d_{lim}/d_c ratio) affects the superstructure behavior more than the design parameter (d_c/d_{Ed} ratio). This means that the over-stroke capacity (continuous line) increases the superstructure resilience compared to isolators with the same geometric dimensions and with restraining ring (dashed line). Fragility curves for the base shear are presented in Figure 6.7b showing how the absence of retaining elements generally increases the superstructure resilience.

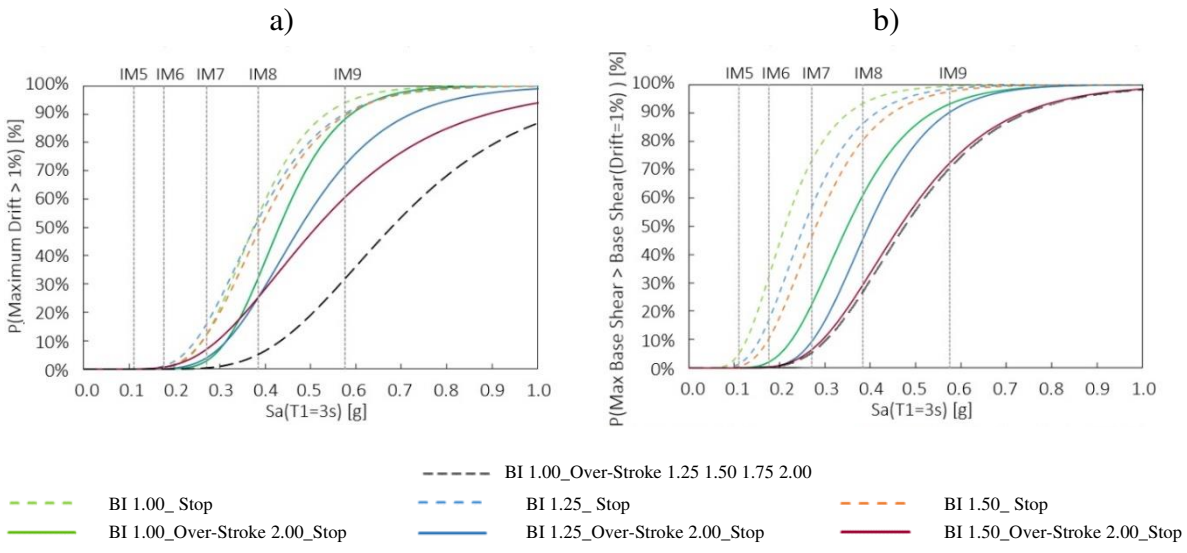

Figure 6.7. Borderline fragility curves for: a) the superstructure drift; b) the base shear.

Superstructure fragility curves, for Drift and Base Shear EDPs, are merged in Figure 6.8 for the three geometric conditions ($d_c/d_{Ed} = 1.00, 1.25, 1.50$). Fragility curves show a consistently

higher exceeding rate for the base shear threshold value than the assumed drift limit, in fact, the structural system DCCSS-moment resistant frame successfully reduces relative displacements but undergoes strong shear increases when contact with retaining element is made.

a)

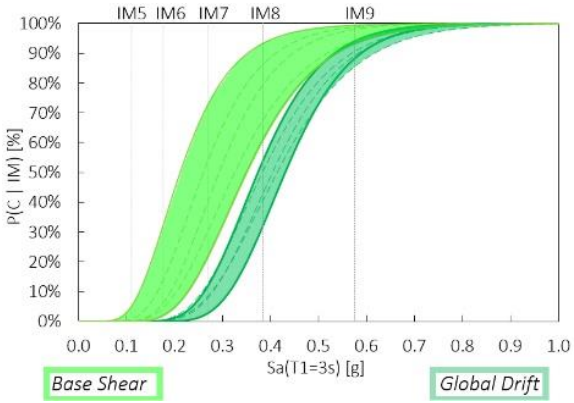

b)

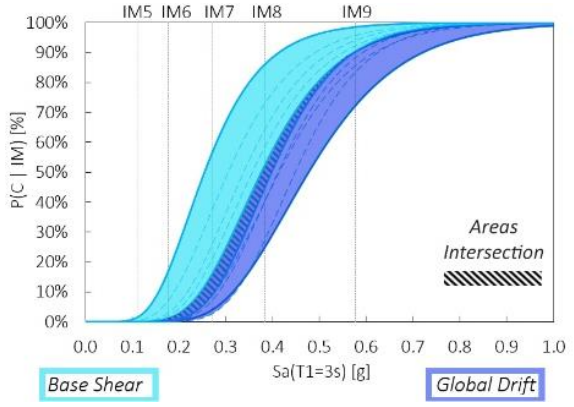

c)

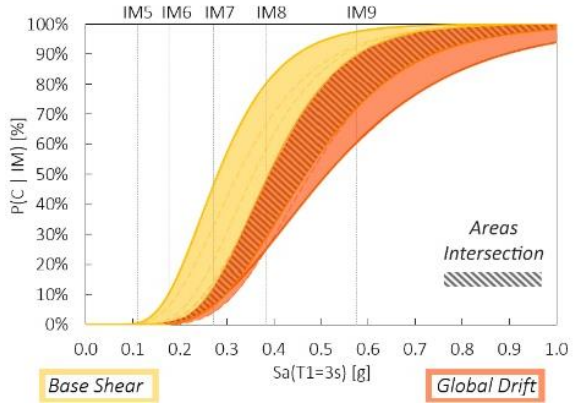

Figure 6.8. Superstructure fragility curves considering Base Shear and Drift EDPs for: a) $d_c/d_{Ed} = 1.00$ *models; b)* $d_c/d_{Ed} = 1.25$ *models; c)* $d_c/d_{Ed} = 1.50$ *models.*

In Figure 6.8a there is no crossing between fragility curves, meaning that the exceeding event of the base shear limit always occurs before the superstructure reaches the deformation limit.

For models with displacement capacity $d_c/d_{Ed} > 1.00$ (Figure 6.8b, c) there are intersection areas between fragility curves families when over-stroke displacement is $d_{lim}/d_c \geq 1.75$.

This means that, regardless of the isolation system failure condition, the over-stroke displacement ensures an overall ductile behavior with a suitable plastic mechanism and avoids brittle failure modes due to the dynamic effects of the slider impact against the restraining ring.

To provide a more accurate and quick comparison, Table 6.6 summarizes the median and the Standard Deviation parameters for the borderline fragility curves (see Figure 6.7) and for each Engineering Demand Parameter (EDP) considered.

Table 6.6 Fragility curves results parameters

Case study	*EDP*	*Median* θ	*Standard Deviation* β
BI 1.00_Stop	Drift	0.374	0.278
	Base Shear	0.212	0.396
BI 1.00_Over-Stroke 2.00_Stop	Drift	0.430	0.245
	Base Shear	0.350	0.335
BI 1.25_Stop	Drift	0.376	0.329
	Base Shear	0.254	0.379
BI 1.25_Over-Stroke 2.00_Stop	Drift	0.477	0.323
	Base Shear	0.397	0.287
BI 1.50_Stop	Drift	0.389	0.311
	Base Shear	0.281	0.366
BI 1.50_Over-Stroke 2.00_Stop	Drift	0.512	0.432
	Base Shear	0.466	0.356
BI 1.00_Over-Stroke 1.25 1.50 1.75 2.00	Drift	0.678	0.348
	Base Shear	0.475	0.349

6.3.4 Annual frequency of exceedance

The seismic resilience of considered models is probabilistically assessed in terms of mean annual frequency of exceeding the superstructure yield drift limit over the lifetime as made by Kitayama and Constantinou [Kitayama and Constantinou, 2018] [Kitayama and Constantinou, 2019a]. Results from the not-isolated and from the base-isolated models are analyzed in terms

of median response (see Figure 6.9) and then combined with the site ground motion hazard representing the probability of exceedance of spectral acceleration [Baker et al., 2005]. Mean annual frequency of exceeding curves for the 1% of drift ratio are presented in Figure 6.9b for the borderline cases (see Figure 6.7). In particular, Figure 6.9b shows a mean annual frequency of exceedance for the maximum drift of 1% which is between the seismic intensities IM5 (LLS) and IM6 (CLS) for the not-isolated structure, and higher than IM8 for all base isolated cases.

For the base isolated cases, the over-stroke behavior significantly reduces the annual frequencies of exceeding improving the seismic resilience of the isolated frame. In particular, buildings isolated using devices with end-stroke regardless of their displacement capacity, have higher mean annual frequencies of exceeding the global drift ratio limit for seismic intensities higher than IM5 (LLS). The use of end-over-strokes generally leads to lower frequencies of exceedance, showing how, a wider displacement in the over-stroke stage ($d_c/d_{Ed} = 1.25$ or 1.50) produces results which are comparable with those of the isolation system without any restraining elements, also for high seismic intensities.

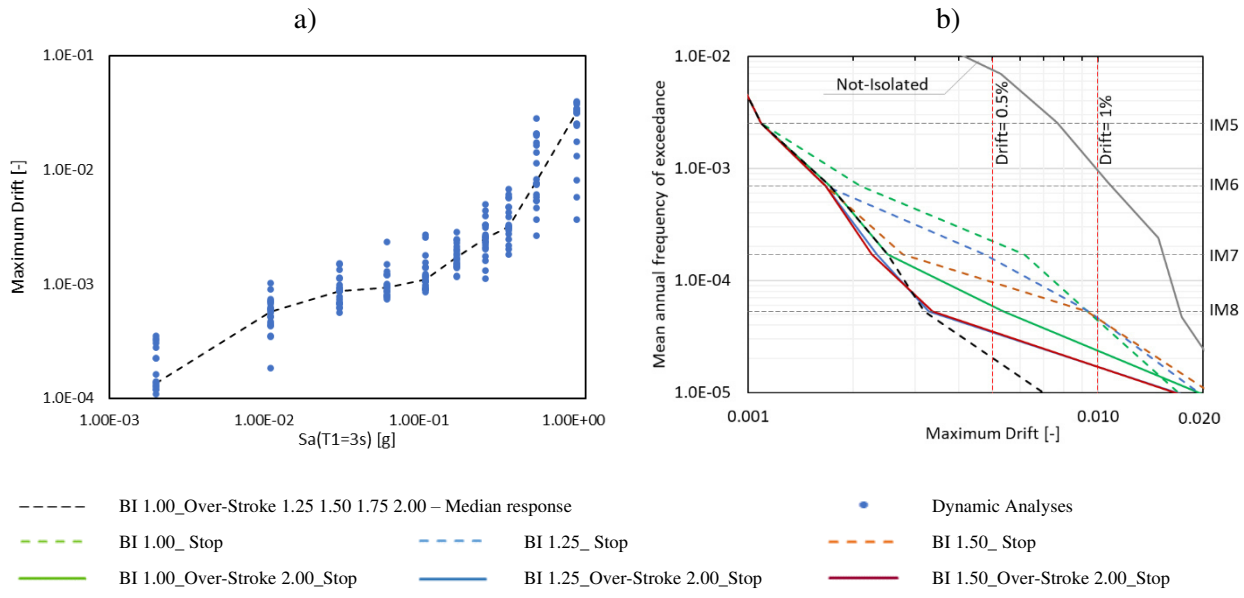

Figure 6.9. a) Median structural drift response versus spectral acceleration at T=3s, b) mean annual frequencies of exceeding for the Drift EDP.

6.3.5 Annual Rates of Failure

Annual rates of Failure for the analysed cases are shown in Figure 6.10 and listed in Table 6.7. Figure 6.10 also shows, with a dashed horizontal line, the reference probability of exceedance for the CLS provided by the current Italian code i.e., 1.00×10^{-3}. This plot provides a global insight onto the structural performances of the analysed cases, showing how the limit Base Shear attainment is, in all cases, the first collapse mode. Annual rates of failure also confirm how the presence of the over-stroke behaviour, although with a retaining element, grants a structural response which is almost the same of the ideal behaviour represented by the cases labelled as "*BI 1.00_Over-Stroke 1.25 1.50 1.75 2.00*" (Figure 6.10 b).

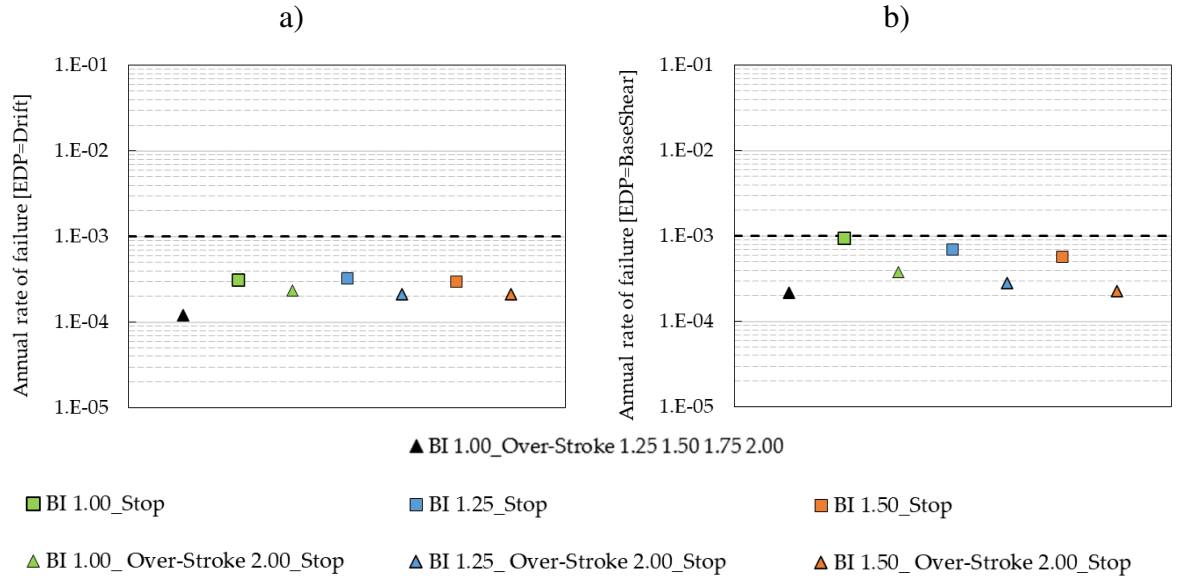

Figure 6.10. Annual rates of failure for the analysed base-isolated case studies, for the Drift (a) and the Base Shear (b) EDPs.

All analysed base-isolated structures are anyways characterized by Annual Rates of failure lower than the CLS one confirming how the DCCSS isolation system is capable of granting the design performance regardless of retaining elements. The case which is characterized by the closest annual rate of failure to the CLS one is the "*BI 1.00_Stop*" confirming how the presence

of a restraining ring positioned at the geometric displacement capacity d_c results in the worst structural performance, yet, in the most perdictable one according to the code design procedures.

Table 6.7 Annual rates of failure for the analysed cases.

Case ID	*EDP*	*Annual Rate of Failure* λf
BI 1.00_Over-Stroke 1.25 1.50 1.75 2.00	Drift	1.205E-04
	Base Shear	2.190E-04
BI 1.00_Stop	Drift	3.123E-04
	Base Shear	9.505E-04
BI 1.00_ Over-Stroke 2.00_Stop	Drift	2.338E-04
	Base Shear	3.757E-04
BI 1.25_Stop	Drift	3.277E-04
	Base Shear	6.955E-04
BI 1.25_ Over-Stroke 2.00_Stop	Drift	2.124E-04
	Base Shear	2.824E-04
BI 1.50_Stop	Drift	3.002E-04
	Base Shear	5.783E-04
BI 1.50_ Over-Stroke 2.00_Stop	Drift	2.151E-04
	Base Shear	2.297E-04

6.4 Finite stiffness retaining elements - Parametric Analysis

A second parametric analysis has been performed onto the Steel and the RC MRF base-isolated structures considering retaining elements with finite stiffness. In particular, the gap element of the *Ring_DCCSS* model (Table 3.3) has been provided with different values of elastic stiffness $K_{gap} = \%K_{str}$ where K_{str} is the superstructural horizontal stiffness. The analysed cases of isolation systems with restraining rings can be listed as follows:

a) infinitely rigid restraining ring ("*Rigid*" case), $K_{gap} = \infty$;

b) infinitely elastic restraining ring ("*Stiff*" case), $K_{gap} = 0.25\%\ K_{str}$;

c) infinitely elastic restraining ring ("*Flexible*" case), $K_{gap} = 0.10\%\ K_{str}$;

d) no restraining ring ("*No_Gap*" case), $K_{gap} = 0$, using the *SingleFPBearing* isolator model (Table 3.3).

It derives that eight 2-dimensional systems are defined, four for each structure, Figure 6.11 shows the cases ID and the corresponding gap stiffness.

Case	K_{gap}	OpenSEES model (from Table 3.3)
Rigid	Unlimited	*Ring_DCCSS*
Stiff	0.25 % K_{str}	*Ring_DCCSS*
Flexible	0.10 % K_{str}	*Ring_DCCSS*
No Gap	Null	*SingleFPBearing*

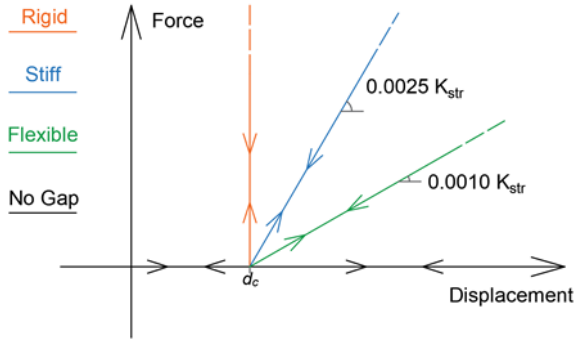

Figure 6.11. Parametric analysis model characteristics of the restraint elements.

6.4.1 Nonlinear Static Analyses

Pushover analyses for case studies of base-isolated and not-isolated frames are presented in Figure 6.12 for the Steel (a) and the Reinforced Concrete (b) model. A distribution of lateral forces proportional to the floor masses was used in the analyses. The red circled points at the

global drift ratios of 1% and 0.3% are the yield drift limits. Pushover curves of the Steel isolated building show a reduction of the maximum base-shear force after the elastic branch linked to the major flexural deformability of the base beam layer added.

Pushover curves of models without displacement restraints (black lines) show the basic behaviour. Curves associated to models with displacement restraint show a first branch until the isolators quasi-rigid behaviour (pre-sliding stage), then a second branch primarily accounting for the isolators restoring stiffness, finally, when the maximum base displacement capacity d_c is reached, curves show a superstructure response similar the not-isolated one. Models with flexible displacement restraints show a less sloping curve after the d_c displacement consistently with the gap stiffness K_{gap} but tend to show the same maximum base-shear force.

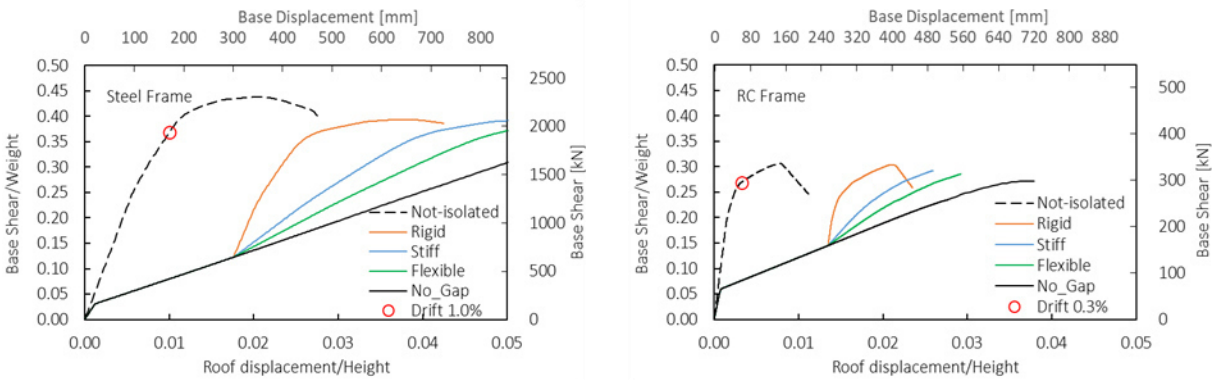

a) b)

Figure 6.12. Non-linear static analyses in fixed-base and base-isolated configurations for the Steel Frame (a) and the RC Frame (b).

6.4.2 Nonlinear Time History Analyses

The seismic performance of the case-study buildings has been analysed using the OpenSEES framework. The study here focused on estimating the effects of different displacement restrainers on base isolated structures by considering several natural ground motions with

different IM. As described in previous sections, a set of 200 accelerograms has been employed to perform MSA on each model, for a total number of 1600 analyses.

The Engineering Demand Parameters (EDP) limit conditions are summarized in Table 6.8. For the superstructures, the same global simplified collapse criterion has been chosen as previously discussed. In particular, the superstructure Global Drift Limit has been related to the end of the elastic branch on the curve. The isolation system EDP considered is the device displacement which limit has been set to the maximum geometric displacement capacity d_c.

Table 6.8 Engineering Demand Parameters reference values.

BI Model	*Superstructure global drift limit* d_{rift} *[%]*	*Maximum base displacement capacity* d_c *[mm]*
Steel Frame	1.0%	± 300 mm
RC Frame	0.3%	± 250 mm

6.4.3 Fragility curves

As a first result, in Figure 6.13 models' Base displacements (a) and Drift (b) response vs time are presented for the steel (left) and the RC (right) frames. Figure 6.13 shows how the "Flexible" cases responses are half-ways between the two borderline cases "Rigid" and "No_Gap". Moreover, results show how a flexible displacement restraint successfully dampens the seismic action resulting in minor superstructural accelerations and displacements preventing impulsive phenomena.

Figure 6.14 shows fragility curves for the superstructure Global Drift on Steel (a) and Reinforced Concrete (b) models. A fragility function is a mathematical relationship that indicates the probability that a structure or part of it will experience damage at or above a specific seismic intensity.

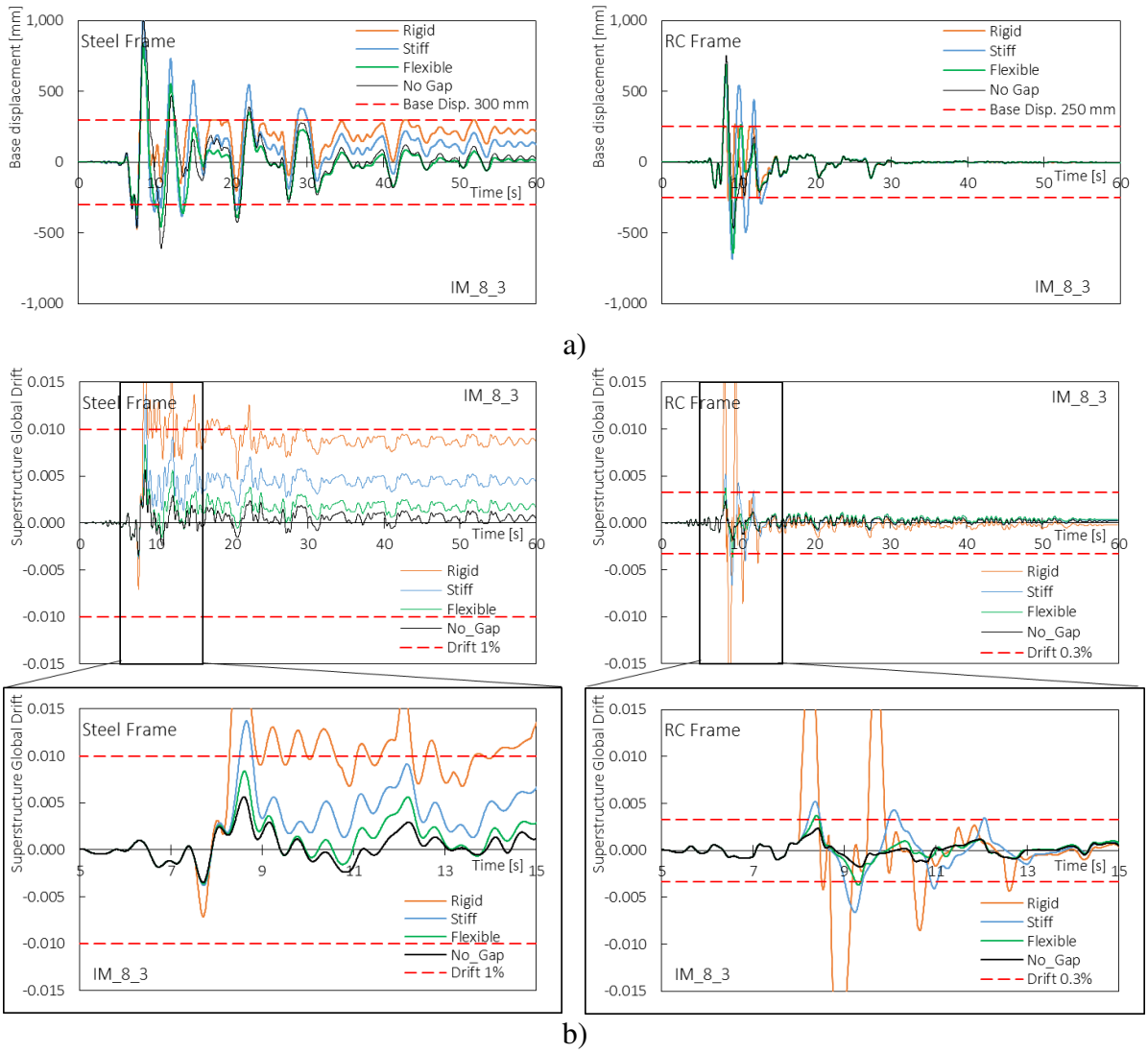

Figure 6.13. Base displacement (a) and Drift (b) time histories for the Steel Frame (left) and the RC Frame (right) for the example accelerogram IM8 - EQ3

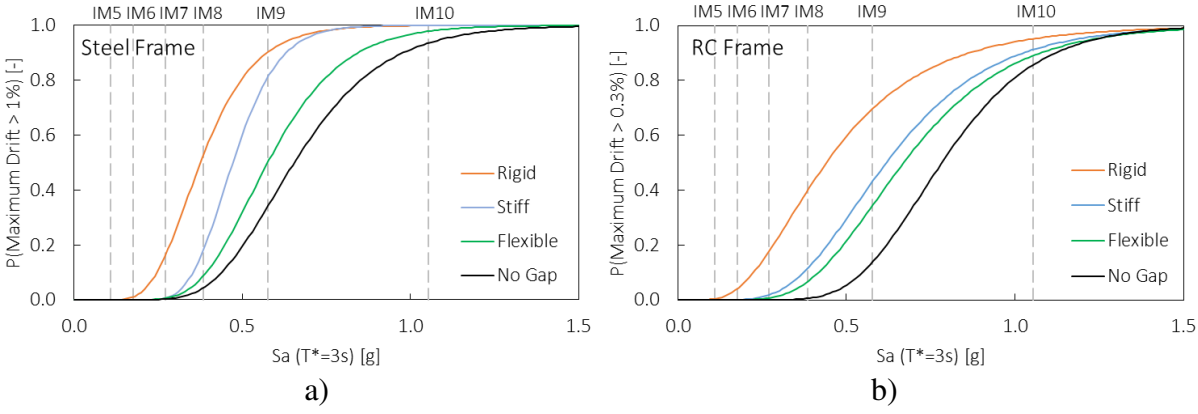

Figure 6.14. Fragility curves for the Drift limit of (a) 1% Steel Frame and (b) 0.33% for the RC Frame.

Despite different construction materials, dimensions and masses, the two structures show the same global tendency. The main comments about exposed results are here listed:

- Fragility Curves associated with "Stiff" and "Flexible" cases are half-ways between the "Rigid" and the "No_Gap" cases showing how a more flexible retaining element leads to lower probabilities of exceeding for the same seismic intensity;
- for the "Flexible" case , fragility curves and Drift time histories show how a deformable retaining element can improve the superstructural seismic performance preventing impulsive phenomena while keeping the design dimensions of the devices;
- both "Stiff" and "Flexible" cases for the RC Frame are characterized by slight differences meaning that the presence of a retaining element, whatever its stiffness is, can strongly affect the superstructural response depending on the construction layout and materials;
- pushover curves show how the effects of a lower initial stiffness for the Steel superstructure tend to increase the gap between the "Stiff" and "Flexible" fragility curves for high seismic intensities compared to the Reinforced Concrete Frame.

Generally speaking, results outline that, the retaining elements stiffness can significantly affect the seismic performance of structures for seismic intensities higher than the design one. Finally, Table 6.9 reports the Median and Standard Deviation Parameters for the analysed case studies.

Table 6.9 Fragility curves results parameters

Case study	*Gap Model*	*Median* θ	*Standard Deviation* β
Steel Frame	Rigid	0.376	0.329
	Stiff	0.472	0.225
	Flexible	0.576	0.298
	No_Gap	0.655	0.313
RC Frame	Rigid	0.440	0.526
	Stiff	0.618	0.394
	Flexible	0.669	0.370
	No_Gap	0.783	0.279

6.4.4 Annual frequency of exceedance

In order to provide a prediction of the probabilities of failure for both the superstructures accounting for the local seismic hazard of design sites, the annual frequencies of exceedance have been computed and the relative curves are shown in Figure 6.15. Mean annual frequency of exceedance curves show, in good accordance with fragility curves presented in Figure 6.14, how, as a general trend, on both structures, the presence of a stiffer retaining element results in higher frequencies of exceedance. The "Rigid" and the "No_Gap" cases outline once more a region in which the "Stiff" and "Flexible" cases curves are. The "Not-isolated" case curve is only reported for the sake of completeness and it has to be noticed how, for these cases, the Intensity Measure scale is different as already shown in Table 6.4. Results are in line with the ones presented in Figure 6.9b proving how retaining elements have a strong influence onto superstructures, enlarging the accelerations on floors when the Over-Stroke displacement is not allowed and when very stiff retaining elements are chosen.

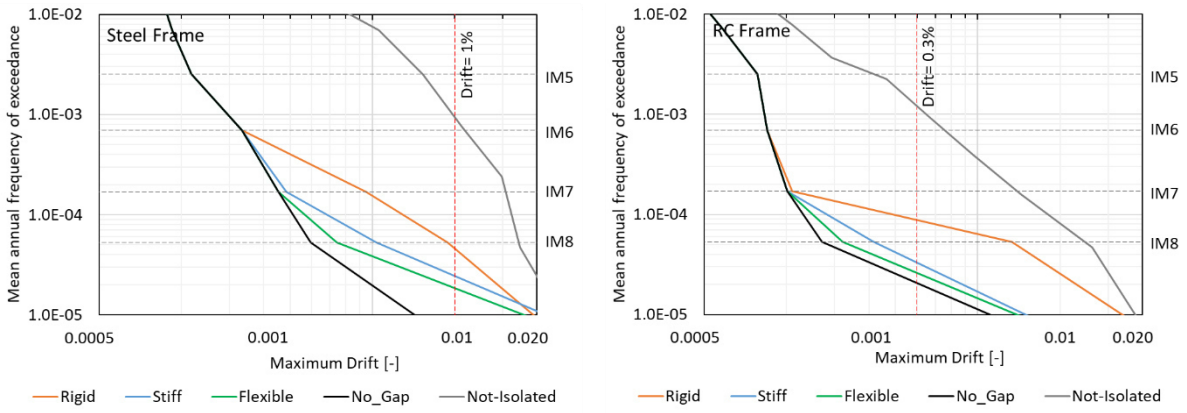

a) b)

Figure 6.15. Mean annual frequencies of exceeding for the Drift EDP.

6.4.5 Annual Rates of Failure

Figure 6.16 shows the annual rates of failure which are also listed, for the sake of completeness, in Table 6.10. Annual Rates of Failure confirm the previously elaborated tendencies showing of lower probabilities correspond to more deformable retaining elements (or to their absence, "*No_Gap*" cases) and vice-versa. The structural performances of cases without retaining elements are about the same of cases with very deformable ones, which, instead, show major differences from cases featuring very rigid displacement restrainers.

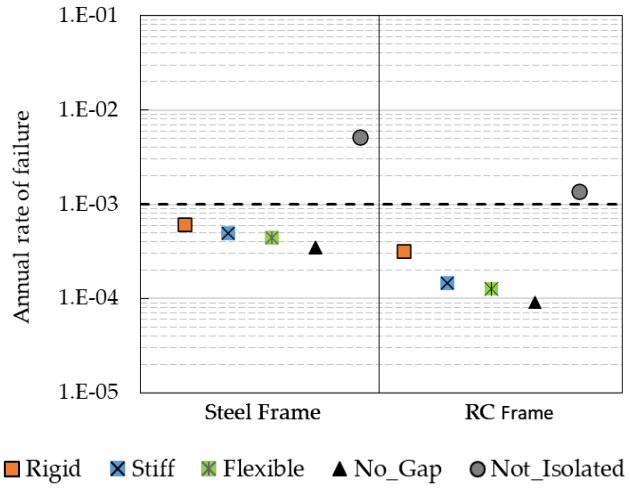

Figure 6.16. Annual rates of failure for the analysed case studies.

Table 6.10 Annual rates of failure for the analysed cases.

Superstructure	*Case ID*	*Annual Rate of Failure* λf
Steel Frame	Rigid	6.176E-04
	Stiff	4.938E-04
	Flexible	4.417E-04
	No_Gap	3.481E-04
	Not_Isolated	5.150E-03
RC Frame	Rigid	3.225E-04
	Stiff	1.478E-04
	Flexible	1.256E-04
	No_Gap	9.075E-05
	Not_Isolated	1.365E-03

7 Algebraic solution development

In previous sections, the mechanical model of DCCSS in standard sliding conditions and the derived algebraic solutions have been described based on the available scientific literature. The focus in this section is on the development of a mechanical model based on the fundamental mechanical principles of physics to describe the over-stroke behaviour of DCCSS devices and to derive proper algebraic solutions for the force vs displacement relationship and their actual limit displacements. The objective is to propose an easy tool to predict the limit displacement and the corresponding shear force starting from the geometrical and mechanical characteristics of the devices. Following [Bao et al. 2017], the envisioned mode of behaviour in the over-stroke regime and the corresponding multi-body kinematic is calibrated on the ad-hoc experimental tests previously described, conducted on devices pushing the horizontal displacement beyond the geometrical capability and revealing how the displacement limit increases preserving the ability to support vertical loads [https://www.fipmec.it/], [Furinghetti et al. 2021]. In the case of DCCSS bearings with flat rim without restraining elements, the limit displacement d_{lim} could correspond to the slider overturning around its barycenter (d_{ot} displacement) beyond the geometrical capacity $d_c = 2u$ if the failure for maximum contact pressure is avoided (d_p displacement), see Figure 7.3c.

Considering the case of a DCCSS slider with the same radii of curvature and coefficients of friction ($R_1 = R_2$ and $\mu_1 = \mu_2$) the sliding occurs simultaneously on both surfaces avoiding rotations along any axes. Two main sliding regimes have been considered for horizontal displacement d:

- within the geometric capacity (*Regime I*): $0 < |d| < d_c$, see Equation (8);
- in the over-stroke condition (*Regime II*): $d_c \leq |d| \leq d_{lim} = min\{d_{ot}; d_p\}$.

The maximum shear force developed by the device and transferred from the superstructure to the foundation is defined as the force $F_{lim} = F(d_{lim})$at the limit displacement d_{lim}, see Equation (37).

7.1 Mechanical model and algebraic derivation

In order to describe the over-stroke behaviour, the mechanical model has been conceived similarly to what described in [Sarlis and Constantinou, 2013]. Considerations on the mechanics of a generic DCCSS have been made on the basis of the schemes reported in Figure 7.1.

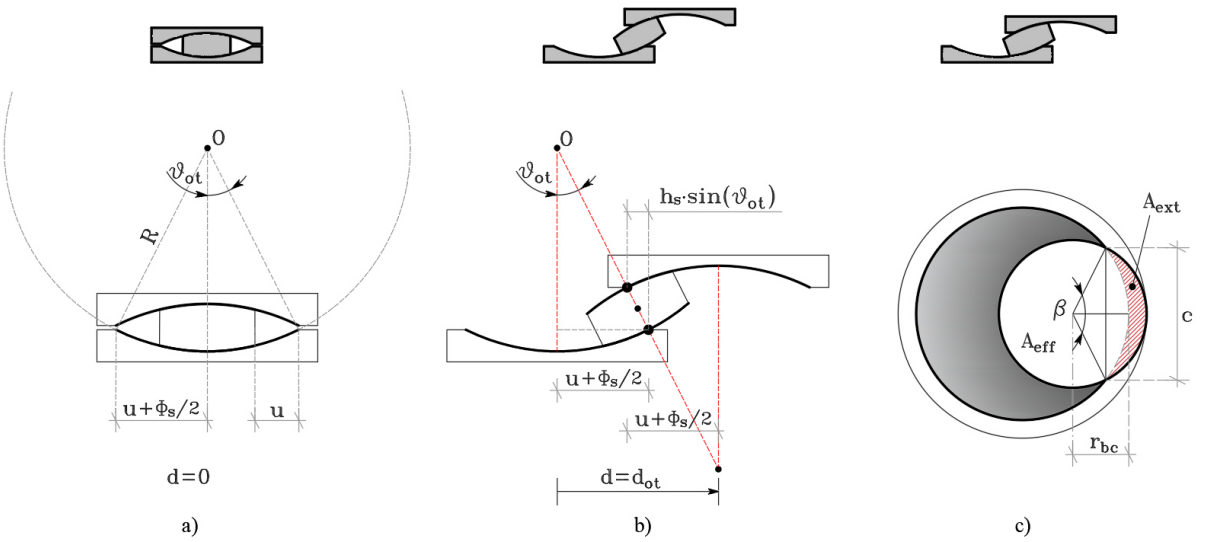

Figure 7.1. Cross-section of the DCCSS in: a) static conditions and b) the Over-Stroke regime; c) planar view of the rigid slider and the housing plate in over-stroke regime.

In the over-stroke stage of motion (Regime II) the previously exposed Equation (8) can be properly modified considering an increased friction coefficient $\mu_2 = \mu + \Delta\mu$:

$$F = W\left(2\frac{\mu_2 R}{R_{eff}}\right) + W\frac{d}{R_{eff}} \tag{28}$$

Theoretically, in the over-stroke regime, the failure mechanism linked to the bearing kinematics occurs when an overturning displacement d_{ot} is reached (position 3 of Figure 7.3a and black

dashed line in Figure 7.3b. Referring to Figure 7.1 the d_{ot} is identified as the displacement corresponding to the alignment of the TCP and the BCP opposite housing plate edges with the barycenter of the slider and with the centres of curvature of both plates (Figure 7.1b) defined by the overturning angle ϑ_{ot} and expressed as follows:

$$\vartheta_{ot} = arcsin\left(\left(u + \frac{\Phi_s}{2}\right)/R\right) \tag{29}$$

$$d_{ot} = 2u + \Phi_s - h_s \cdot sin\,(\vartheta_{ot}) \tag{30}$$

Then, substituting the geometric capacity displacement $d_c = 2u$ and Equation (29) in Equation (30) the final expression for the overturning displacement can be written as follows:

$$d_{ot} = \frac{R_{eff}}{2R}(d_c + \Phi_s) \tag{31}$$

It has to be noticed that the overturning displacement is often not implemented as a failure condition for DCCSSs because the failure linked to the attainment of the maximum contact pressure on the reduced slider area occurs for a generally shorter displacement $d_p < d_{ot}$. The displacement d_p associated with the attainment of the limit contact pressure $\sigma_a = W/A_{eff}$ on the sliding interface between the rigid slider and concave plate is shown in the scheme of Figure 7.1c, where A_{eff} is the effective contact area between slider and housing plate equal to the slider surface reduced by the area of the slider external to the sliding pad A_{ext}.

$$A_{eff} = \pi\left(\frac{\Phi_s}{2}\right)^2 - A_{ext} \tag{32}$$

The external area A_{ext} formulation can be found, using simple geometric considerations, to be:

$$A_{ext} = \frac{1}{2}\left(\frac{\Phi_s}{2}\right)^2 \beta - \left(c \cdot \frac{r_{bc}}{2}\right) \tag{33}$$

where β is the angle described by connecting the intersection point between the slider and the sliding pad circumferences, c is the circumference chord which connects these intersection points and r_{bc} is the distance between the sliding pad border and the slider centre (see Figure 7.1c), represented as follows:

$$\beta = 2 * arcsin\left(\frac{c/2}{\Phi_s/2}\right) \tag{34}$$

$$c = 2\sqrt{\left(\frac{\Phi_s}{2}\right)^2 - (r_{bc})^2} \tag{35}$$

$$r_{bc} = d_c + \frac{\Phi_s}{2} - d \tag{36}$$

Substituting Equations (32) to (35) in Equation (36) and remembering that $\sigma = \frac{W}{A_{eff}}$, the displacement $d_p = d(\sigma = \sigma_a)$ associated to the limit contact pressure is expressed as:

$$d_p = \frac{2\,W}{c\,\sigma_a} - \frac{2}{c}\left(\frac{\Phi_s}{2}\right)^2\left(\pi - arcsin\left(\frac{c}{\Phi_s}\right)\right) + \left(\frac{\Phi_s}{2} + d_c\right) \tag{37}$$

Table 7.1 shows a summary of the proposed analytical formulations and Figure 7.2 provides the backbone curve of the force-displacement relationship based on them.

Table 7.1 Summary of the over-stroke behaviour of DCCSS bearing.

Regime	Description	Equation	Domain
I	General sliding condition on concave surfaces	$F = \mu\frac{2\,R}{R_{eff}}W + W\frac{d}{R_{eff}}$	$0 < \lvert d\rvert \le d_c$
II	Sliding in the Over-stroke regime	$F = \mu_2\frac{2\,R}{R_{eff}}W + W\frac{d}{R_{eff}}$	$d_c < \lvert d\rvert \le d_{lim}$ $d_{lim} = min\{d_{ot}; d_p\}$

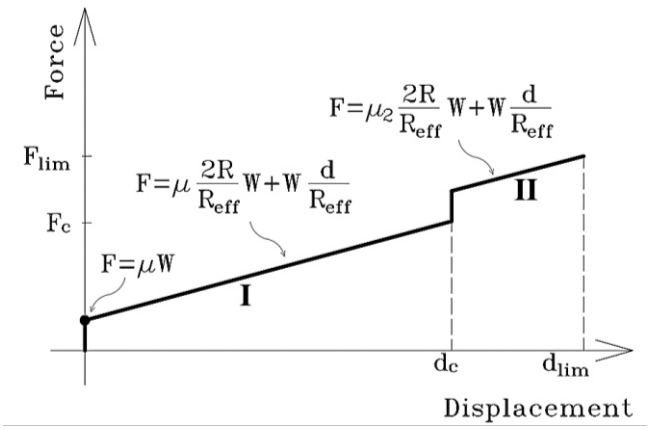

Figure 7.2. Force-displacement backbone curve for the over-stroke behaviour of DCCSS bearing.

7.2 Experimental results comparison

The prevoiusly introduced controlled displacement test performed by [https://www.fipmec.it/], has here been used to validate the proposed mechanical model and algebraic solution Table 7.2. Experimental results show that when the rigid slider overcomes the concave sliding surface edge (position 1 of Figure 7.3a) it can move up to a half of its diameter (position 3 Figure 7.3a), resulting in a slight increase in force (black line in Figure 7.3b). In loading and unloading phases of the first cycle, the DCCSS over-stroke behaviour is characterized by a "sloping dog bone" shape, preserving the re-centring capability and the ability to support gravity load. A sudden increase of the horizontal force and of the local equivalent stiffness occurs as the sliding pad travels beyond the housing plate edge (Figure 7.3a). From a mechanics point of view, this behaviour could be represented by an increase of the friction coefficient $\Delta\mu = 0.015$ that occurs as the sliding pad comes in contact with the small edge of the housing plate sliding material (counterbore gap material). The test was stopped to a displacement d_p when the maximum contact pressure of the sliding material was reached (Figure 7.3c), this limit has been set to an allowable contact pressure of $\sigma_a = 60$ MPa for polytetrafluoroethylene (PTFE)-based sliding material.

Table 7.2 Main characteristics of DCCSS specimen and of over-stroke experimental test.

	Sliding regime					**Over-stroke regime**			
	W *[kN]*	R_{eff} *[mm]*	μ *[-]*	Φ_s *[mm]*	d_c *[mm]*	$\Delta\mu$ *[-]*	d_p *[mm]*	d_{ot} *[mm]*	F_{lim} *[kN]*
Experimental [https://www.fipmec.it/]	2500	2500	0.04	310	±136	0.015	±298	±425	474.34

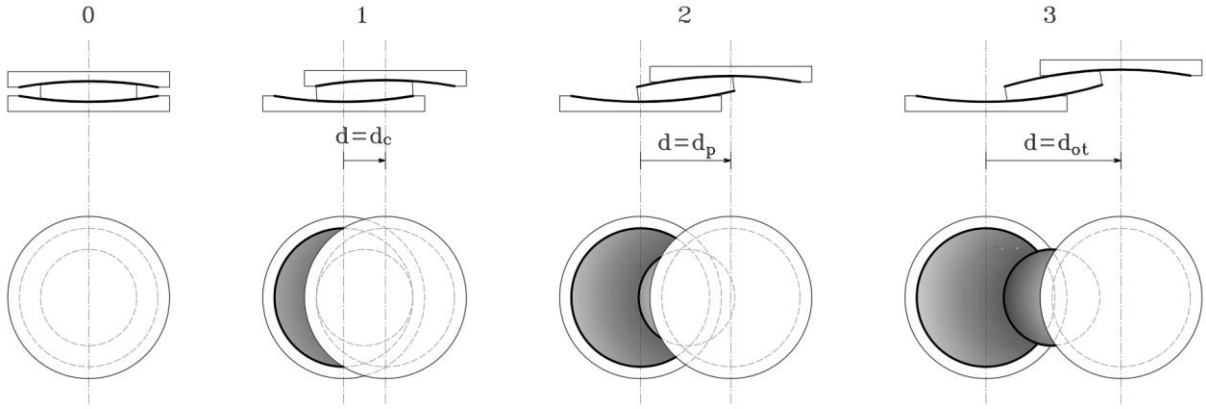

a)

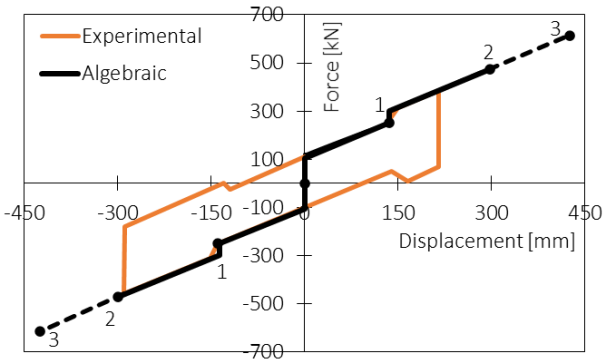

b)

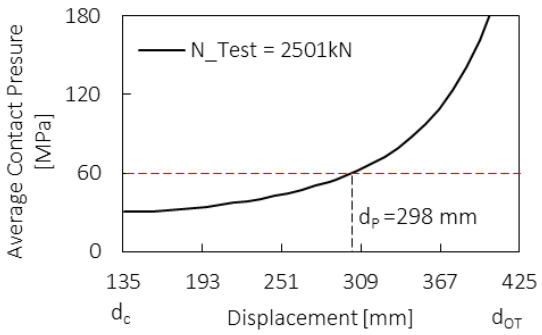

c)

Figure 7.3. Cross-sections and planar views of the DCCSS test specimen in static condition and in three main deformed stages a), test diagrams of: force b) and average contact pressure c) vs displacement.

As Figure 7.3b provided a good, in order to have a more solid experimental base, the algebraic solution has been implemented and compared for the displacement-controlled over-stroke tests carried out by [Furinghetti et al. 2021]. The experimental results show that in the over-stroke regime, the friction coefficient increases of $\Delta\mu = 0.015$ for all tests. Experimental force-displacement results have been replicated using the proposed formulation, Figure 7.4 shows that the algebraic solution is capable of representing DCCSSs behaviour during tests with a significantly good approximation. For the experimental cases of [Furinghetti et al. 2021], the

limit displacement can be calculated using the proposed formulation $d_{\text{lim}} = min\{d_{ot} = 515\ mm;\ d_p = 415\ mm\}$.

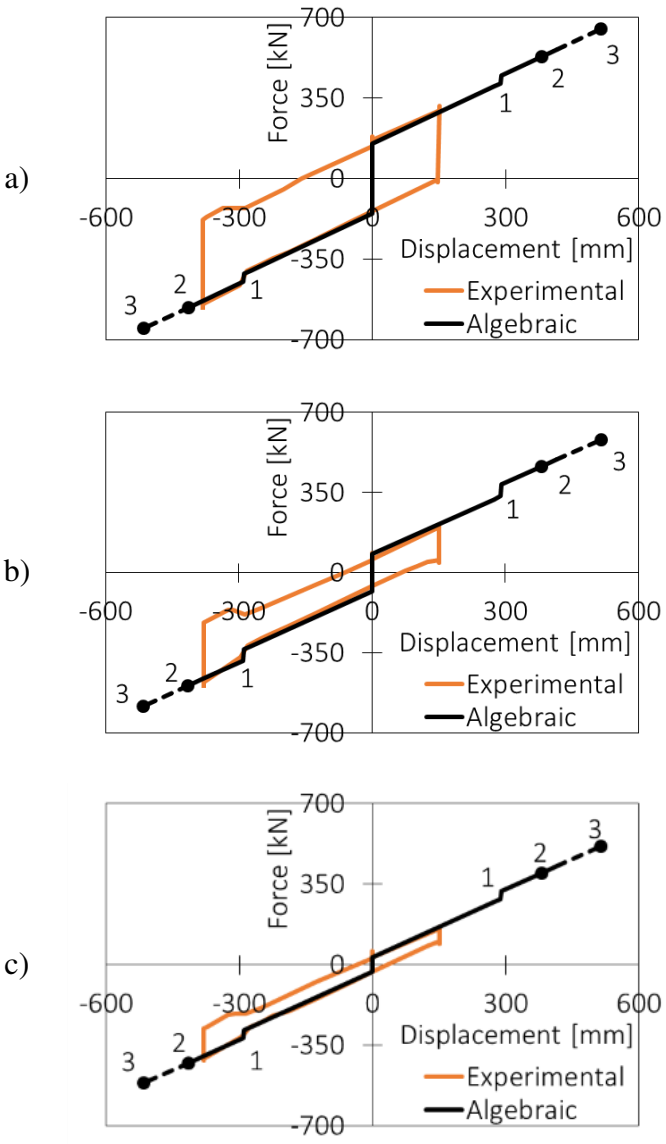

Figure 7.4. Force - displacement test results by [Furinghetti et al. 2021] compared with the proposed algebraic solution.

7.3 Case study

The case study prototype structure labelled as "S80-90" in the present doctoral dissertation has been considered for an example application of the proposed algebraic solution. The geometrical and mechanical parameters of the isolation system previously designed (see Table 5.3) are used

in the proposed algebraic solution in order to define the displcements d_p and d_{ot}, the limit displacement d_{lim} and the shear force limit F_{lim}. Results are exposed in Table 7.3 and the designed DCCS isolator and the force-displacement law employed in the study are shown in Figure 7.5.

Table 7.3 Main characteristics of DCCSS for the case study.

	Standard sliding regime								Over-stroke regime			
	W	R_{eff}	μ	Φ_s	T_{eq}	ξ_{eq}	d_{bd}	d_c	$\Delta\mu$	d_p	d_{ot}	F_{lim}
	[kN]	[mm]	[-]	*[mm]*	[sec]	[%]	[mm]	[mm]	*[-]*	*[mm]*	*[mm]*	*[kN]*
Numerical	1133	3700	0.05	200	2.97	26	216	±330	0.015	420	516	189.68

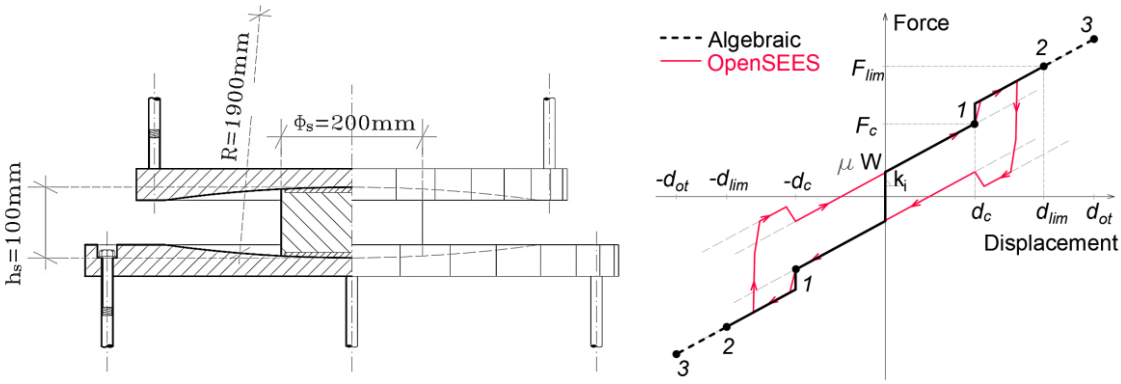

a) b)

Figure 7.5. a) DCCSS case study isolator and relative b) sloping dog bone shape constitutive law used for the study.

Nonlinear time history analyses results, have been considered, in this case, for the 3 intensity levels IM5-6-7 whose return periods are respectively $T_R = 500y$, corresponding to the LLS, $1000y$ corresponding to the CLS and $2500y$ corresponding to the highest return period from the Italian code [NTC 2018]. The elastic spectra of the 20 selected earthquakes for each return period, for both the main horizontal directions (X and Y), are shown in Figure 7.6 with their relative mean spectrum.. Detailed information about the ground motion selection can be found in [Iervolino et al. 2018] and [Iervolino et al. 2011].

The comparison between the mean spectra at the different return period and the design spectrum is shown in Figure 7.7 in terms of pseudo-acceleration and pseudo-displacement. Figure 7.7

also shows for each return period the mean value of the spectral acceleration Sa(T) correspondig to a vibration period of T=3.0 sec. Due to the record-to-record variability, Figure 7.6 and Figure 7.7 highlight how the selected earthquakes cover a wide range of spectral acceleration (Figure 7.7a) and displacements (Figure 7.7b) around the design spectrum.

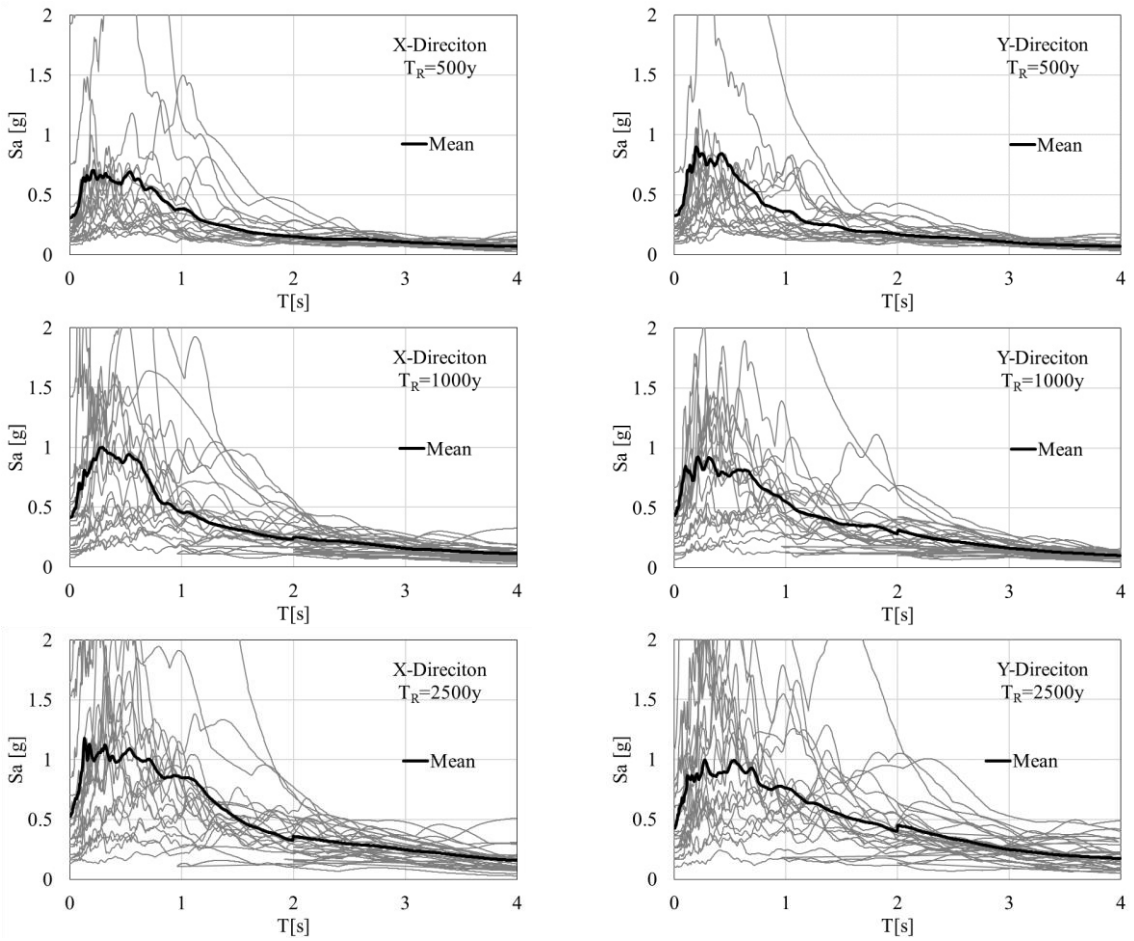

Figure 7.6. Acceleration Spectra for the 20 chosen record in X and Y directions for the selected return Periods.

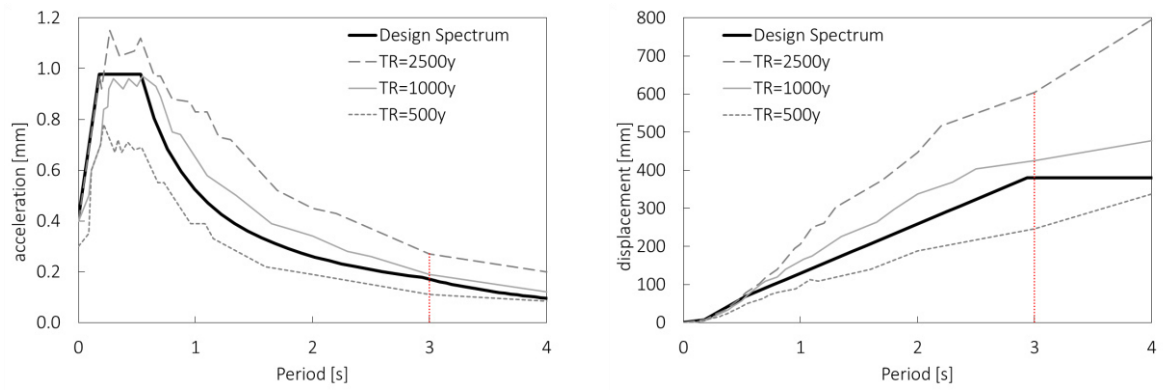

a) b)

Figure 7.7. Design and mean spectra of seismic inputs: a) acceleration and b) displacement.

7.4 Results

Figure 7.8 shows the comparison between the proposed algebraic solution (see equations in Table 7.1) and results of NTHA for the records which reached the limit displacement d_{lim}. It is worth noting that for all of the seismic intensities, 16 cases out of 60 reach the limit displacement d_{lim}.

In particular, for the cases with a return period of $T_R = 500y$, all records showed a maximum displacement lower than the capacity displacement d_c of the devices. For the $T_R = 1000y$ cases, 4 records out of 20 reached the capacity displacement d_c one of which also reached the limit displacement d_{lim}. For the high seismic intensity cases $T_R = 2500y$, the displacement d_c has been exceeded by 17 records while the d_{lim} by 15, as shown in Figure 7.8.

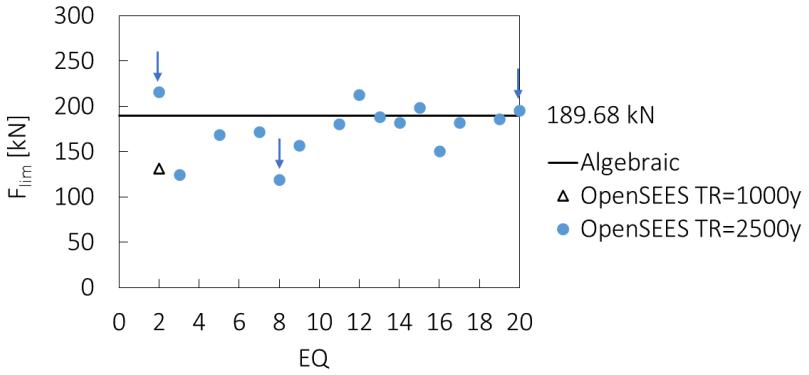

Figure 7.8. Isolation bearing limit shear forces from NTHA compared with the algebraic solution F_{lim}.

The F_{lim} value can be considered as the maximum shear force acting on DCCSS, it is useful to properly design the device and their connections to the structure and to the foundation. These connections shall be designed to transfer the forces developed in the device without failure, granting the ability to support gravity loads even after strong seismic events. Without a proper design procedure backened on the proposed parameters values, the design process may lead to oversized connection systems resulting in significantly higher construction costs.

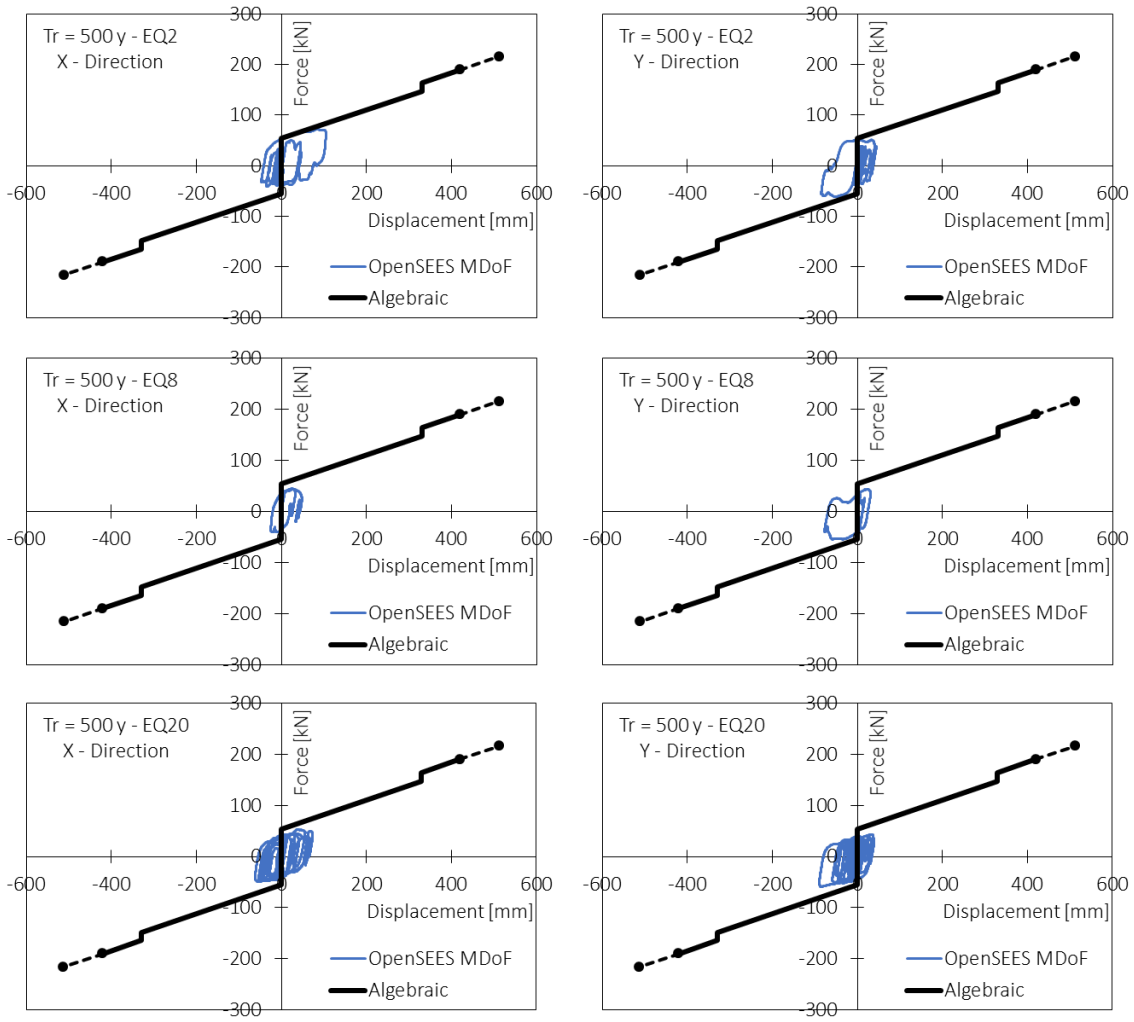

Figure 7.9. Single DCCSS bearing force vs displacement relationship in X and Y directions for three example earthquakes (EQ2; EQ8; EQ20) of Return Period 500 years.

The black continuous line represents the algebraic solution for the bearing force F_{lim} correspondng to a limit displacement d_{lim} (see Table 7.3). Values recorded by the OpenSEES software range around the F_{lim} algebraic force with some deviation due to the friction coefficient dependency on the axial force and instantaneous velocity variabilities. Among the 16 cases which reached d_{lim} (1 for $T_R = 1000y$ and 15 for $T_R = 2500y$) the recorded values of F_{lim} are: minimum 118.88 kN, mean 172,83 kN and maximum 215.79 kN. Just 3 cases out of 16 show a value of force higher than the predicted by the algebraic solution, resulting in a 19% probability of a not conservative solution.

More detailed insight on the analyses results are given from Figure 7.9 to Figure 7.11 where the comparison between the algebraic solution and the MDoF model forces vs displacement behaviour of a DCCSS bearing located in the central position, considering three example earthquakes for each return period (EQ2, EQ8, EQ20) indicated in Figure 7.9, is shown.

Intensities corresponding to the design force (CLS, $T_R = 1000y$), characterized by few cases of over-stroke displacement, stand out as the best fitted by the proposed analytical formulation (Figure 7.10). Figure 7.9an Figure 7.10 show the differences between the MDoF model and the Regime I algebraic solution proposed in basic theories for seismic intensities lower and equal to the design one.

Some differences between the numerical and the algebraic results can be observed for high seismic intensities ($T_R = 2500y$) when the over-stroke is activated (Figure 7.11) linked to the axial force and the velocity variabilities strong influence on the shape of the force-displacement law. For the case study, results have shown a good approximation of the frictional shear force estimation provided by the algebraic solution.

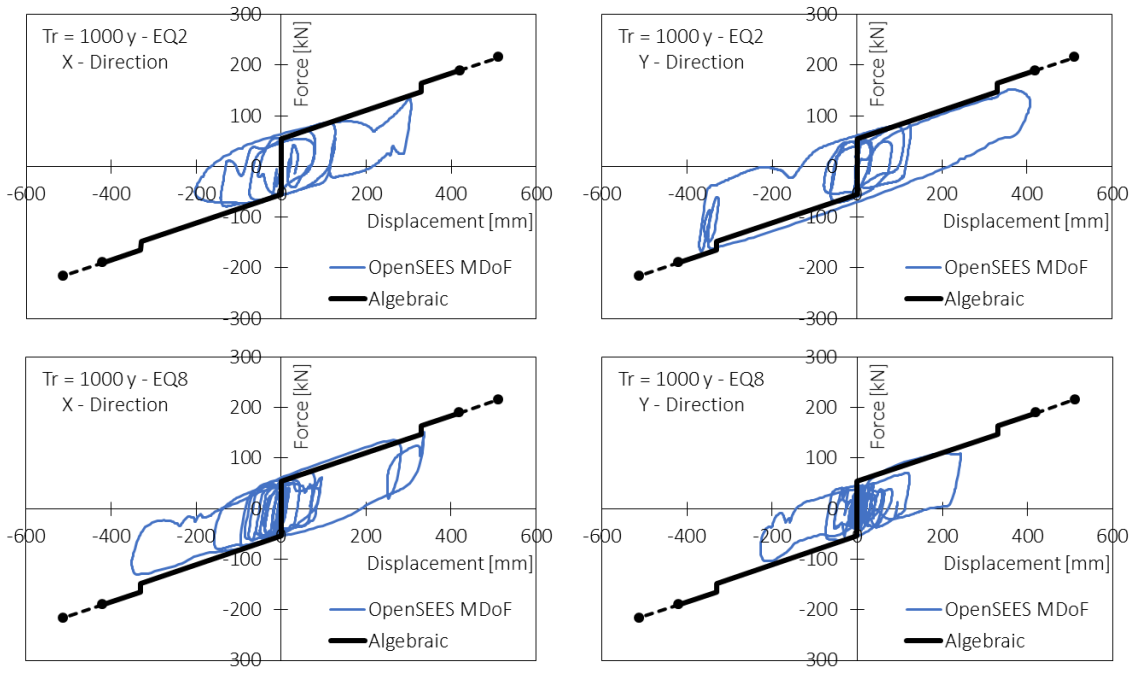

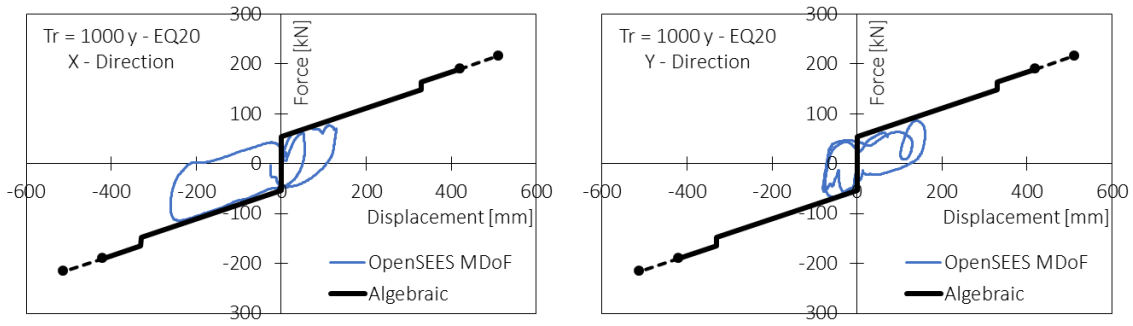

Figure 7.10. Single DCCSS bearing force vs displacement relationship in X and Y directions for three example earthquakes (EQ2; EQ8; EQ20) of Return Period 1000 years.

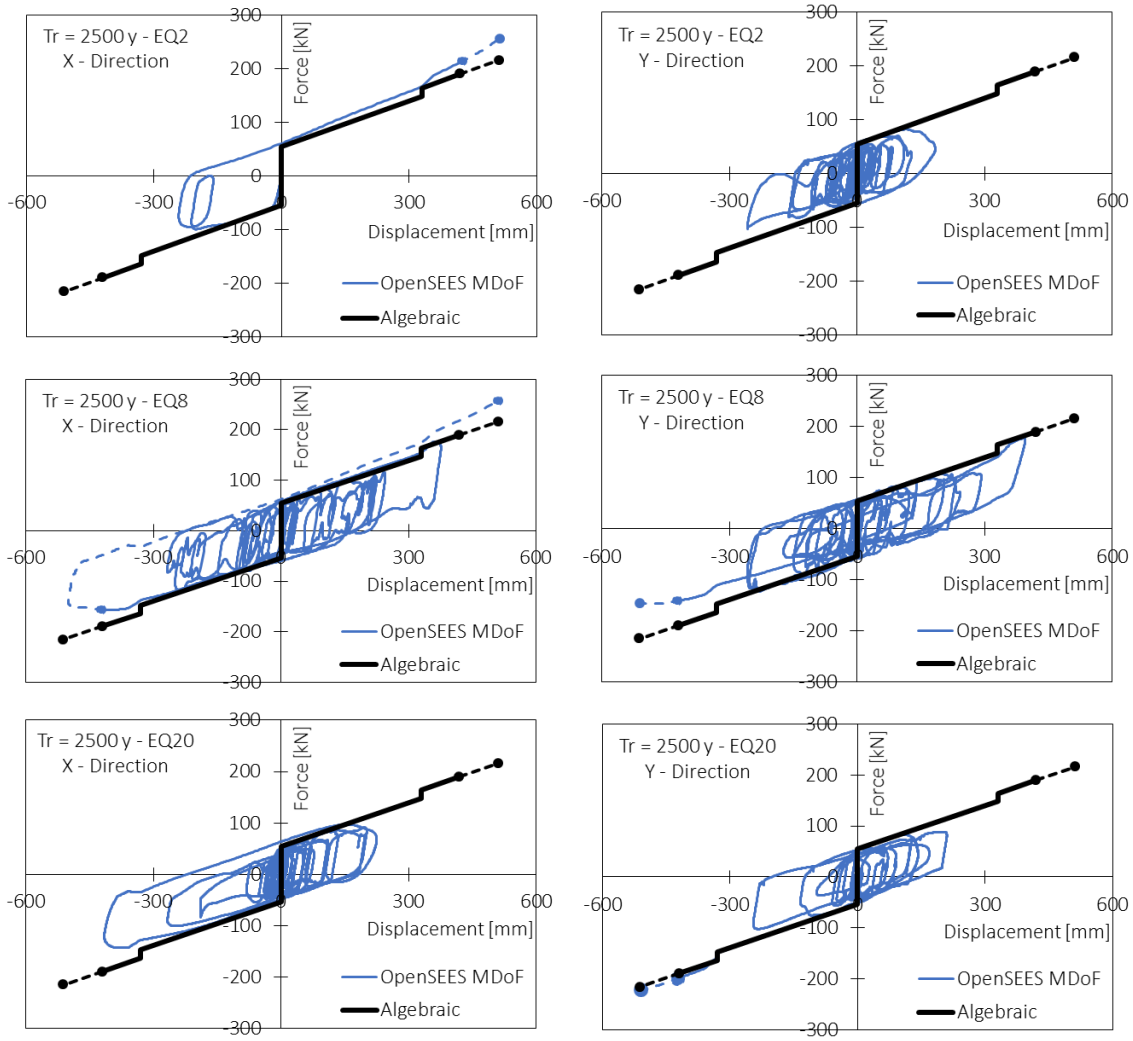

Figure 7.11. Single DCCSS bearing force vs displacement relationship in X and Y directions for three example earthquakes (EQ2; EQ8; EQ20) of Return Period 2500 years.

7.5 Matlab script

In order to provide a simple and independent tool capable of computing the limit displacements, representing the dynamic response in both sliding regimes of a DCCSS bearing and providing an easily implementable routine also for more complex analyses in both sliding regimes, a MatLAB [Mathworks, 2018] script has been set up. For the sake of simplicity, the script has been developed for a SDoF model featuring a DCCSS bearing with a mass positioned on the Top Concave Plate. The Matlab script has been set up to require a time history as input and to provide, as output, the Force-Displacement relationship of a SDoF [Tazarv, 20201] system featuring a DCCSS bearing. The Matlab script has been fully reported in the **Appendix A** of the present doctoral dissertation. The script starts with an acquisition phase in which the SDoF DCCSS system input parameters are required. The limit displacements and the associated limit force F_{lim} are computed according to Equations (31) (for the d_{ot}) and (37) (for the d_p). An "error" message is shown if the limit pressure displacement d_p is reached for static conditions. This condition happens when an equivalent system is analysed considering the global superstructure vertical load W onto the equivalent isolator. In this condition, the value of W to be exclusively employed in the d_p calculation, should be referred to the axial load on the most loaded bearing of the whole isolation system. The script also checks whether the displacement d_p is lower or not than d_{ot}, and plots the respective values. The Equations Of Motion (EOM) Newmark integration is then performed changing the system coefficient of friction and stiffness from k_p and k_i when required. Finally found displacements are used to determine frictional forces for both Sliding regimes according to equations provided in Table 7.1.

7.5.1 Equation of Motion Integration

Newmark's EOM integration method, [Newmark, 1959], allows the direct solution of a second-order differential equation or a system of second-order differential equations without the need for the transformation to a pair of simultaneous first-order differential equations [Daniel, 2001]. The method may be applied in various fields of engineering, in particular to dynamic response systems. The Equation of Motion is expressed by the following second-order differential Equation (38):

$$M\ddot{u} + C\dot{u} + Ku = f(t) \tag{38}$$

where M is the mass matrix, C is the damping matrix and K is the stiffness matrix. In the case of SDoF M, C and K are the mass, damping and stiffness values computed for the system. It has to be noticed that, in general if M, C, T are arrays of constant coefficients, and the function $f(t)$ is a function of time only, then the equations deriving from Equation (38) are linear differential equations, otherwise they are non-linear. The present study only required the solution of linear differential equations deriving from the aforementioned EOM. In this case the Newmark method begins by employing the mean value theorem for the displacement u, and implies the existence of a scalar β such that:

$$u(t + \Delta t) - u(t) = \dot{u}(t + \beta\Delta t)\Delta t \tag{39}$$

where Δt is time step considered in the analysis. The Newmark method then uses the standard Taylor series expansion for the term $u(t + \Delta t)$ of Equation (39) and of the function $\dot{u}(t + \Delta t)$, up to the third-order derivative of u. Denoting $u(t + \Delta t)$ by u_{n+1} and $u(t)$ by u_n, these are given by:

$$u_{n+1} = u_n + \dot{u}_n\Delta t + \ddot{u}_n\frac{(\Delta t)^2}{2!} + \dddot{u}_n\frac{(\Delta t)^3}{3!} + \cdots \tag{40.I}$$

$$\dot{u}_{n+1} = \dot{u}_n + \ddot{u}_n\Delta t + \dddot{u}_n\frac{(\Delta t)^2}{2!} + \cdots \tag{40.II}$$

Applying the generalized mean theorem, and supposing the existence of a scalar Υ, Equations (40) may be re-arranged as follows:

$$u_{n+1} = u_n + \dot{u}_n \Delta t + \ddot{u}_n \frac{(\Delta t)^2}{2!} + \beta\, \dddot{u}_n (\Delta t)^3 + \cdots \tag{41.I}$$

$$\dot{u}_{n+1} = \dot{u}_n + \ddot{u}_n \Delta t + \Upsilon\, \dddot{u}_n (\Delta t)^2 + \cdots \tag{41.II}$$

where scalars values need to respect the conditions $0 \leq \{\Upsilon; \beta\} \leq 1$ so that Equations (41) are true, and the third derivative $\dddot{u}_n$, if linear, may be written as $\dddot{u}_n = (\ddot{u}_{n+1} - \ddot{u}_n)/\Delta t$. Substituting this value into Equations (41) and composing them, the displacement formula is obtained:

$$u_{n+1} = u_n + \dot{u}_n \Delta t + (1 - 2\beta)\ddot{u}_n \frac{(\Delta t)^2}{2!} + \beta\, \ddot{u}_{n+1} (\Delta t)^2 + \cdots \tag{42}$$

From Equation (42), the acceleration formula is provided by Equation (38):

$$\ddot{u}_{n+1} = M^{-1}(f(t_{n+1}) - C\dot{u}_{n+1} - K u_{n+1}) \tag{43}$$

Equations (43), (42) and (41.II) respectively provide the formulae for accelerations, displacements and velocities, anyways, their form is implicit, and must be rearranged to obtain the expressions for the updated values knowing values at the integration step n. Reformulating the displacement expression, the acceleration $\ddot{u}_{n+1}$ can be expressed as follows:

$$\ddot{u}_{n+1} = \frac{u_{n+1} - u_n}{\beta\, \Delta t^2} - \frac{\dot{u}_n}{\beta\, \Delta t} - \left(\frac{1}{2\beta} - 1\right)\ddot{u}_n \tag{44}$$

Composing Equation (43) in (41.II) the following expression of velocity is obtained:

$$\dot{u}_{n+1} = \Upsilon \frac{u_{n+1} - u_n}{\beta\, \Delta t} - \dot{u}_n \left(1 - \frac{\Upsilon}{\beta}\right) - \Delta t \left(1 - \frac{\Upsilon}{2\beta}\right)\ddot{u}_n \tag{45}$$

Finally, the explicit formulae for velocity (Equation (45)) and acceleration (Equation (44)) can be combined in Equation (38) to obtain:

$$M\left[\frac{u_{n+1} - u_n}{\beta\, \Delta t^2} - \frac{\dot{u}_n}{\beta\, \Delta t} - \left(\frac{1}{2\beta} - 1\right)\ddot{u}_n\right] + C\left[\Upsilon \frac{u_{n+1} - u_n}{\beta\, \Delta t} - \dot{u}_n \left(1 - \frac{\Upsilon}{\beta}\right) - \Delta t \left(1 - \frac{\Upsilon}{2\beta}\right)\ddot{u}_n\right] + K u_{n+1} = f(t_{n+1}) \tag{46}$$

Where substituting:

$$A = \frac{M}{\beta\, \Delta t^2} + \frac{\Upsilon C}{\beta\, \Delta t} + K \tag{47.I}$$

$$B_n = f(t_{n+1}) + M\left[\frac{u_n}{\beta\,\Delta t^2} + \frac{\dot{u}_n}{\beta\,\Delta t} + \left(\frac{1}{2\beta} - 1\right)\ddot{u}_n\right] + C\left[\Upsilon\frac{u_n}{\beta\,\Delta t} - \dot{u}_n\left(1 - \frac{\Upsilon}{\beta}\right) - \Delta t\left(1 - \frac{\Upsilon}{2\beta}\right)\ddot{u}_n\right] \quad (47.\text{II})$$

in Equation (46) the following simple solution is found:

$$A \cdot u_{n+1} = B_n \quad (48)$$

Equation (48) is the explicit form for the EOM solution which also provides the explicit expression for the displacement $u_{n+1} = A^{-1}B_n$. It has to be noticed that if β and Δt are given specific values, A is a constant values array, while B_n changes for each iteration. Having determined u_{n+1} Equations (44) and (45) can be used to determine $\ddot{u}_{n+1}$ and $\dot{u}_{n+1}$. Knowing $\ddot{u}_{n+1}$ the value of $\dot{u}_{n+1}$ can be determined and the iterative process can continue. values for γ and β can be chosen for each specific case. An undamped system (that is $C = 0$) is conditionally stable if $\gamma \geq \frac{1}{2}$, and unconditionally stable if $\gamma \geq \frac{1}{2}$ and $\beta \geq \frac{1}{4}\left(\gamma + \frac{1}{2}\right)^2$. However, $\gamma > \frac{1}{2}$ introduces artificial damping into the solution, and so standard values chosen by Newmark [Newmark, 1959] are $\gamma = \frac{1}{2}$ and $\beta = \frac{1}{4}$. This is sometimes referred to as the *average acceleration method* and it is *unconditionally stable*, meaning that the method will converge for all time increments. If $\beta = \frac{1}{6}$ is chosen, the method is called the linear acceleration method, which is *conditionally stable*. It is important to consider the stability of Newmark's method, i.e., the conditions under which the algorithm will converge to the correct solution. In certain circumstances Newmark's method is *unconditionally stable*, this means that the method will converge for all time increments. This is the case if the following condition is satisfied:

$$2\beta \geq \gamma \geq \frac{1}{2} \quad (49)$$

An example of values satisfying this condition is $\beta = \gamma = 1/2$. Anyways, it is important to note that certain γ values introduce significant errors in the computational process.

7.5.2 Validation

The compiled Matlab script employs the Newmark EOM integration method and the Equations from Table 7.1, to determine the force vs displacement relationship of a DCCSS bearing. The script validation has been made according to available over-stroke tests.

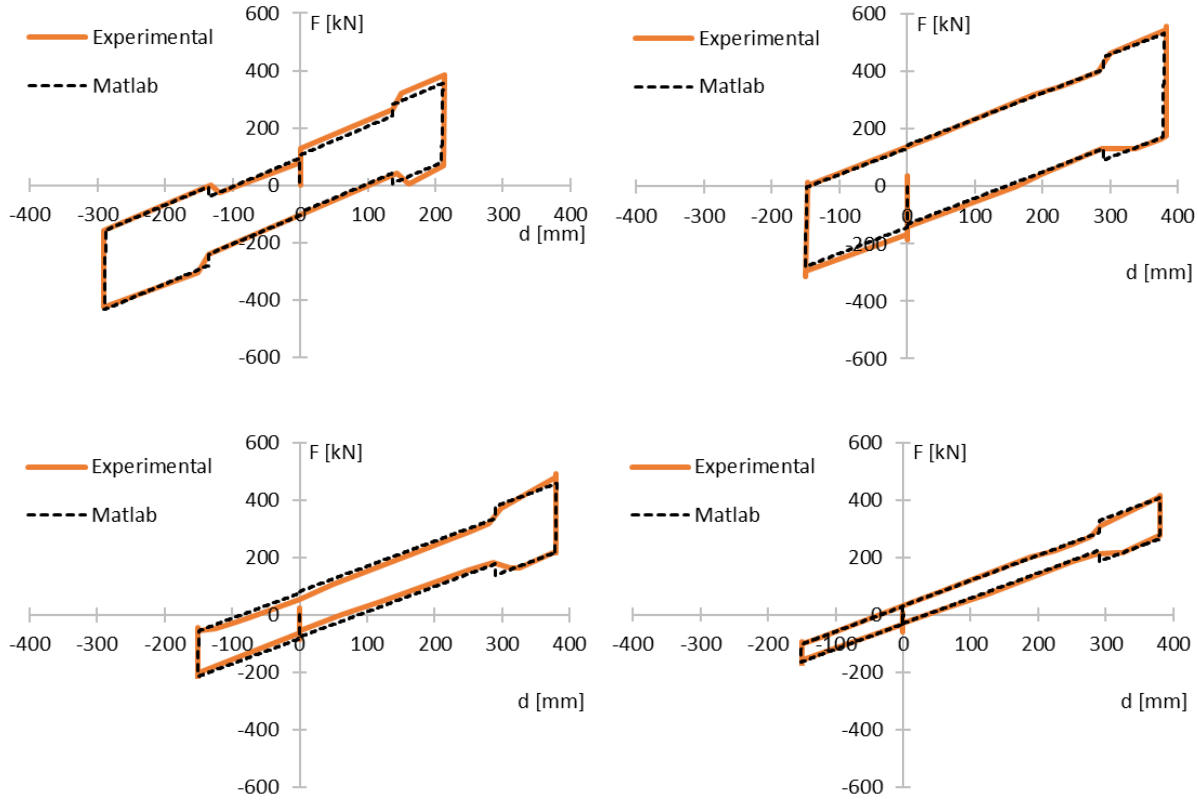

Figure 7.12. Comparison between experimental tests outcome and Matlab script results.

As seen in previous sections (**§ 3.2 Modelling**) for the numerical model, in Figure 7.12 a comparison between the experimental outcome and results provided by the Matlab script subjected to same external forces is provided. Figure 7.12 shows how the proposed script provides a good representation of the considered experimental outcome. It has to be noticed how, when the d_c displacement is reached, the script is characterized by an instantaneous increment in friction coefficient and force, while results show a different behaviour, characterized by the previously shown stiffness $k_2 + k_p$ (Figure 3.6). This behaviour has been

analysed in detail by [Furinghetti et al., 2021] providing also an algebraic equation describing the friction coefficient variation as the displacement increases beyond the d_c capacity. Anyways, the formulation presented by [Furinghetti et al., 2021] has not been implemented in the proposed script, considering the transition between the two sliding regimes as instantaneous (as already shown in Figure 7.2) and considering the effects of the $k_2 + k_p$ stiffness negligible. Although the modelling of the transition between the sliding regimes has been neglected in order to speed up calculation times, the proposed script easily allows its implementation.

7.5.3 Example application

For the purpose of showing the script response, some analyses have performed on the SDoF equivalent model of the isolation system from the case study S80-90 (already discussed and described in detail in the section **§5.1 Case Studies** of the present dissertation). The analyses have been performed employing the Coulomb friction model [Mostaghel and Davis 1997] and considering the seismic input used for L'Aquila site. For the sake of comparison, in Figure 7.13 and Figure 7.14 the force vs displacement relationships for three sample accelerograms (EQ 2-8-20) from intensity measures characterized by the return periods of 1000 and 2500 years are shown. The Matlab script outputs show a good general consistency with the consolidated OpenSEES model results providing reliable values of forces and displacements also in the Over Stroke sliding regime. The script, as already mentioned, computes limit displacements d_p, d_{ot}, the user can either choose to automatically interrupt the analysis when one of them is reached, or not, as in this case, in order to show the ideal response of the isolator.

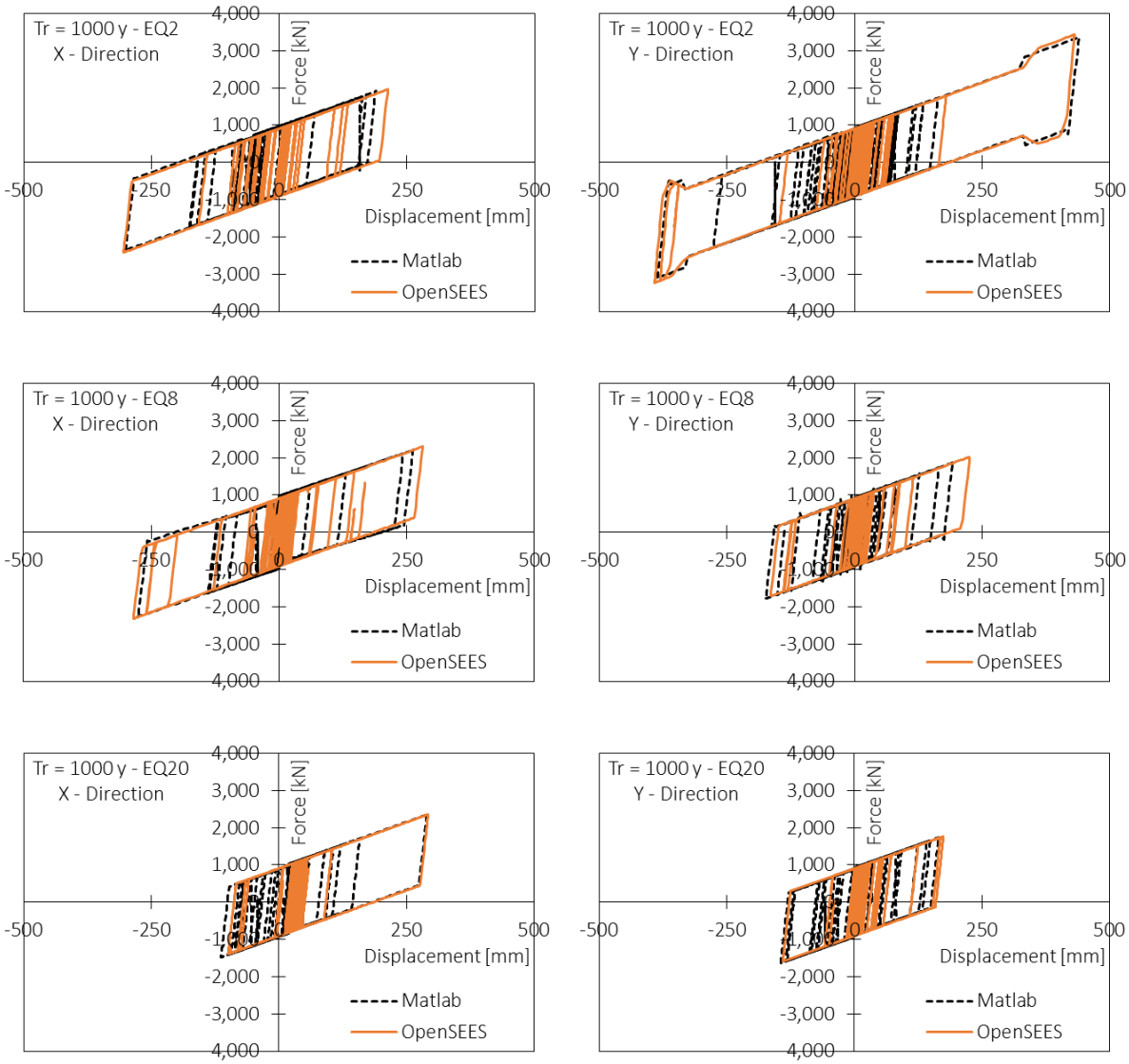

Figure 7.13. SDoF DCCSS bearing force vs displacement relationship in X and Y directions for three example earthquakes (EQ2; EQ8; EQ20) of Return Period 1000 years.

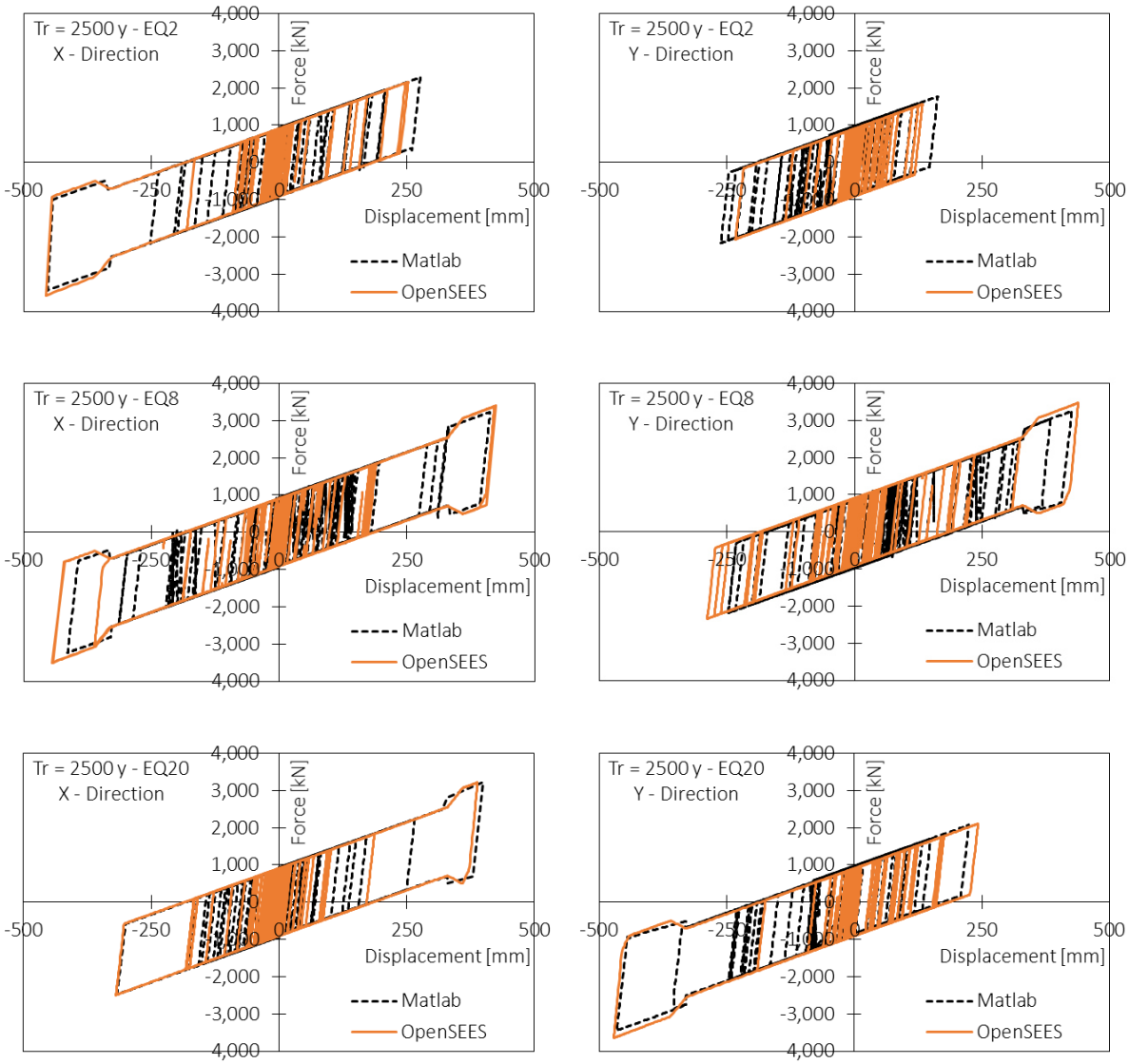

Figure 7.14. SDoF DCCSS bearing force vs displacement relationship in X and Y directions for three example earthquakes (EQ2; EQ8; EQ20) of Return Period 1000 years.

8 Summary and conclusions

The numerical campaigns performed at University of Basilicata on base-isolated structures with Double Concave Curved Surface Sliders (DCCSS) allowed a detailed study on many parameters which influence the seismic response of these buildings under many different superstructural and isolation system conditions finalized at providing a contribution to the seismic isolation field. The research covered a large number of case study structures analysed employing both complex and simplified models.

The main focus of the present doctoral dissertation was the investigation of the behaviour of DCCSS bearings related to the Over-Stroke displacement regime and to the presence of displacement retaining elements. The research work is backened by four ad-hoc experimental tests conducted on DCCSS specimens featuring an over-stroke displacement. The first experimental test has been performed by FIP MEC [https://www.fipmec.it/] while the others have been performed by Furinghetti, Yang, Calvi and Pavese [Furinghetti et al. 2021]. All tests have been conducted with the controlled-displacement approach, constant vertical load and very low velocity in order to provide a good control on the test apparatus and prevent vertical instability. Experimental tests were fundamental in order to validate numerical and algebraic models and to provide accurate and truthful results. More than 10,000 Nonlinear Time History Analyses (NTHA) have been performed within this research work considering a wide range of seismic intensities around the design ones. Results from all the analyses pointed out the fundamental role of the over-stroke displacement behaviour of DCCSS bearings in providing a larger displacement capacity and, in general, in improving the seismic performance of the structures.

The main findings and conclusions drawn from this work are here summarized.

Civil use DCCSS base-isolated buildings seismic performance investigation.

The analysed case studies comprise eight archetype residential RC buildings differing for construction periods (1950s-60s, 1970s, 1980s-90s, 2018) and design approach (Gravity Load Design, GLD, and Seismic Load Design, SLD, based on old technical standards, performance-based design for the current seismic code). The analyses have been performed within the RINTC research project on existing RC buildings retrofitted with DCCSS seismic isolators according to the Italian minimum code requirements.

GLD buildings are supposed to be located in the city of Naples (characterized by medium seismic hazard for Italy), SLD buildings are supposed to be located in the city of L'Aquila (characterized by high seismic hazard for Italy) and a new-construction building has been considered as located in both sites. Isolation systems have been designed to avoid any superstructural damage up to the Life safety Limit State (LLS), in accordance with the current Italian Seismic Code. All case studies have been assessed by means of Multi Stripe nonlinear time history Analysis (MSA), computing the annual failure rates for two performance levels, namely Global Collapse (GC) and Usability Preventing Damage (UPD). As base-isolated buildings are in-series systems (being composed by the isolation system and the superstructure) and isolation devices can undergo different failure modes, a multi-criteria approach has been followed for the definition of the aforesaid performance levels. The most advanced numerical models have been used to simulate the behaviour of the isolation devices. The OpenSEES *SingleFPBearing* element has been modified in order to simulate the over-stroke behaviour of the bearings implementing three zero-length parallel hinges.

The results referred to the GC limit state show that existing RC buildings retrofitted by seismic isolation work effectively in limiting damage to the superstructure, the first collapse mode is, in fact, always referred to the isolation system as observed for New Construction buildings. The

seismic performance, furthermore, has been observed to improve with the age of design, even though, the failure rates tend to be around the same values and below the code-provisioned limit. A notable result has been provided by the isolation system failure cases recorded for design seismic intensities even considering the increased device displacement capacity in the over-stroke regime. Thus, as a final remark, the analyses campaign highlighted how current design codes should provide more detailed and specific indications about the safety margins to be assumed for base-isolated buildings in order to avoid poor performance for earthquake intensity levels equal or greater than design. The indications should be tailored for different base-isolation systems (as studied within the RINTC research work) and should be different for low, medium and high seismic zones in order to get homogeneous reliability levels.

Retaining elements influence on base-isolated structural performance.

For DCCSS bearings, the use of end-stroke restraints (end stops) such as restraining rings is admitted by American standards [ASCE/SEI 7-10, 2013] [ASCE, A. 2010]. The European Standard [UNI EN 15129 (2009)], instead, does not allow the presence of any mechanical element that serves as restrainer and that can be damaged by the impact under seismic excitations. However, the European Standard allows the use of ground retaining walls, or specific devices such as rubber bumpers attached to the walls, that can be used as over-stroke displacement restrainers. The effects of the over-stroke displacement and the presence of retaining elements on isolated structures have been investigated considering two simple bi-dimensional frames, a Steel and a RC one, as case studies of residential use buildings.

Two parametric analyses have been performed considering retaining elements with unlimited and finite stiffness.

The first parametric analysis has been performed considering the 2D moment resistant Steel Frame and a total number of thirty base-isolated models set up considering the configurations with and without over-stroke effects and with and without end stops. Analyses have been considered referring to the Engineering Demand Parameters (EDP) of superstructure global Drift and Base Shear.

Results showed how the superstructural response has not been affected by the increase of isolator displacement capacity when retaining elements have not been employed, the reason is that by removing seismic stops, the inelastic action on the superstructure are delayed in all cases. Furthermore, models with an adequate margin on the design displacement and over-stroke capacity, proved delay the attainment of Base Shear limit forces leading to higher superstructure relative displacement and to the global drift failure mechanism to occur first. This particular result leads the over-stroke capacity to be useful in achieving the hierarchy of resistance for structural failure modes. For the analysed case study, in fact, the superstructure was able to develop all of its plastic capacity improving the resilience of the global structural system.

The second parametric analysis has been performed considering and comparing the 2D moment resistant Steel and RC frames. Four basic models for the retaining element behaviour were proposed for each building, a "Rigid" one with infinite stiffness K_{gap}, two flexible models with $K_{gap} = 0.25\%\ K_{str}$ and $K_{gap} = 0.10\%\ K_{str}$ respectively labelled as "Stiff" and "Flexible" and a model with no stiffness "No_Gap". Plus, the fixed-base cases have been considered too. Based on nonlinear static analyses, limit values for the Global Drift EDP have been set. Fragility curves have been used for all the nonlinear time histories analyses results processing. Despite different construction materials, dimensions and masses, the two structures showed the same global tendency. Fragility Curves associated with "Stiff" and "Flexible" cases are half-ways between the "Rigid" and the "No_Gap" cases showing how a more flexible retaining element

leads to lower probabilities of exceeding for the same seismic intensity. Moreover, fragility curves and Drift time histories for the "Flexible" case showed how a deformable retaining element is capable of improving the superstructural seismic performance preventing impulsive phenomena while keeping the same design dimensions of the devices. Pushover curves also showed how the effects of a lower initial stiffness for the Steel superstructure tend to increase the gap between the "Stiff" and "Flexible" fragility curves for high seismic intensities compared to the Reinforced Concrete Frame.

Results outline that, the retaining elements stiffness can significantly affect the seismic performance of structures for seismic intensities higher than the design one. Results also point out how, very flexible retaining elements, are capable of producing a superstructural response which is similar to the one associated to the ideal case of DCCSS with flat rims, thus, current design codes should give more detailed provisions on retaining elements be them restraining rings or moat walls and characterizing the limit values for their stiffness.

Algebraic solution development

Finally, based on the experience gained by the large number of structures and isolation systems numerically analysed within this dissertation, an algebraic solution for the over-stroke sliding regime characterization and the associated failure displacements has been developed. A mechanical model has been considered on the basis of previous consolidated theories such as the ones proposed by Sarlis, Kitayama and Constantinou [Sarlis and Constantinou, 2013], [Kitayama and Constantinou, 2018], [Kitayama and Constantinou, 2019b]. The force vs displacement law has been developed for the over-stroke sliding regime. The algebraic solution for two failure mechanisms accounting for the rigid slider overturning kinematic and the maximum contact pressure on the sliding interface has been provided in terms of algebraic

equations for the force-displacement relations. The solution is valid for DCCSS bearings with rigid slider and flat rim, equal radii of curvature and friction coefficients on both of the concave plates. All of the algebraic assumptions have been also validated through the aforementioned experimental tests. The utility of the proposed solutions is in checking the validity of numerical solutions of more complex models and in designing the actual limit displacement and the maximum shear force of the device with a good accuracy. Furthermore, the maximum shear force F_{lim} algebraic expression provided, is of crucial importance in the design of the connections between isolation devices and structure. In order to validate the application of the proposed algebraic equations, a structural model, suitable for nonlinear dynamic analyses has been implemented in the OpenSees software, representing the case study of a six-storey RC frame building seismically isolated, at the ground level, with DCCSS bearings with over-stroke capacity.

Results obtained by nonlinear analysis were in good agreement with the results from the direct implementation of the proposed algebraic equations. In particular, the proposed algebraic solution showed to be very accurate in the representation of shear forces acting on the single DCCSS bearing in the over-stroke regime that could not be predicted by the previously available model. Furthermore, results showed how the high accelerogram variability significantly affects the structural response. The conditional spectrum design method revealed to be inaccurate in the prediction of forces and displacements values during design, thus the algebraic solution discussed, accounting for the over-stroke behaviour of DCCSS isolators should provide a safer tool for designers.

A Matlab script has then been developed in order to provide an easy and independent tool which can be used to immediately compute the limit displacements and forces for DCCSS bearings. Furthermore, the script is capable of running NTHAs reading input time histories and providing

the force-displacement recording of a SDoF DCCSS system as output. To do so, the Newmark Equation of Motion (EOM) integration has been adopted and implemented in the script.

A comparison between OpenSEES NTHA results for a SDoF DCCSS system and Matlab script NTHA results pointed out a good agreement both in terms of forces and displacements. The developed script so, has been proven to be capable not only of providing accurate information about the DCCSS system design parameters, but also to perform quick NTHA with a good approximation when compared to more complex software.

Possible impact on design codes

The possible impact that the present doctoral dissertation may have on design codes regards seismic isolation DCCSS sliding devices. In the future, design codes may help designers giving specific prescriptions about the actual geometric limit displacement of DCCSS sliders taking into account over-stroke effects. Codes could provide different safety factors depending on the over-stroke limit displacement, the sliding material of the bearing and the presence of retaining elements. Codes could indeed provide specific prescriptions about the presence of retaining elements such as moat walls,, their distance from the isolation system, their stiffness and their relative linear/nonlinear model.

With the evidence provided by the present doctoral dissertation outcome, it can also be assumed that a possible impact on the italian design code will be about the possibility to perform nonlinear static (pushover) analyses onto base-isolated structures. The code should provide applicability rules, and simplified methods for base-isolated pushover curves representation. This code evolution could help designers determine the maximum structural base shear and could provide limit values for the structure damage.

All made assumptions should be backened by further research, investigating different structural types, constructive technologies, materials and cases.

Open fields of research.

Even though Curved Surface Sliding (CSS) devices largely diffused worldwide in last years, a full understanding of their performances, and limits, has not been yet completely reached. The present research focused on providing useful information about the performances and limits of Double Curved Concave Surface Sliders (DCCSS) featuring a rigid inner slider and characterized by the same radii of curvature and the same friction coefficient on both sliding surfaces. Further research should be carried out considering different CSS devices and a bigger range of isolated structures. Further developments are also needed to identify robust models and their cyclic behaviour for DCCSS bearings also considering the material degradation linked to the entrance in the over-stroke sliding regime, and for retaining elements such as moat walls. Finally, more experimental tests should be performed on many different devices featuring different geometric and mechanical parameters and accounting for the failure of the restraining ring and the degradation of the sliding material. The findings could contribute to estimate with major accuracy the seismic risk of seismic isolated structures with slider bearings and to develop appropriate safety factors in future building codes.

References

Akkar, S., Bommer, J.J. (2010) Empirical Equations for the Prediction of PGA, PGV, and Spectral Accelerations in Europe, the Medi-terranean Region, and the Middle East. Seismol. Res. Lett. 2010, 81, 195–206.

ASCE/SEI 7-10 (2013) Minimum Design Loads for Buildings and Other Structures.

ASCE, A. (2010). Minimum design loads for buildings and other structures.

Aslani, H, Miranda, E (2005). Probabilistic earthquake loss estimation and loss disaggregation in buildings. Report No. 157. The John A. Blume Earthquake Engineering Center, Department of Civil and Environmental Engineering, Stanford University, Stanford, CA, USA.

Baker, J. W., Cornell, C. A., Tothong, P. (2005) Disaggregation of seismic drift hazard. In Proceedings, 9th ICOSSAR05.

Baker, J.W. (2011). Conditional Mean Spectrum: Tool for ground motion selection. Journal of Structural Engineering, 137(3), 322-331.

Baker, J.W. (2015) Efficient analytical fragility function fitting using dynamic structural analysis. Earthquake Spectra, 31.1: 579-599.

Bao, Y., Becker, T.C., Hamaguchi, H. (2017) Failure of double friction pendulum bearings under pulse-type motions. EESD, 46(5), 715-732.

Bao, Y., Becker, T. C. (2018) Effect of design methodology on collapse of friction pendulum isolated moment-resisting and concentrically braced frames. JSE, 144(11), 04018203.

Bao, Y., Becker, T. C., Sone, T., Hamaguchi, H. (2018)a Experimental study of the effect of restraining rim design on the extreme behavior of pendulum sliding bearings. EESD, 47(4), 906-924.

Bao, Y., Becker, T. C., Sone, T., Hamaguchi, H. (2018)b To limit forces or displacements: collapse study of steel frames isolated by sliding bearings with and without restraining rims. SDEE, 112, 203-214.

Baraschino, R., Baltzopoulos, G., Iervolino, I., (2020) R2R-EU: Software for fragility fitting and evaluation of estimation uncertainty in seismic risk analysis. DOI: https://doi.org/10.1016/j.soildyn.2020.106093

Bowden, F.P., Tabor, D. (1964) The friction and lubrication of solids – part II Oxford University Press, London, Great Britain

Bradley, B. A., Dhakal, R.P. (2008). Error estimation of closed-form solution for annual rate of structural collapse. Earthquake Engineering & Structural Dynamics, 37(15), 1721-1737.

Cardone, D., Conte, N., Dall'Asta, A., Di Cesare, A., Flora, A., Lamarucciola, N., Micozzi, F., Ponzo, F.C., Ragni, L. (2019) RiNTC-e project: The seismic risk of existing italian rc buildings retrofitted with seismic isolation. In Proceedings of the COMPDYN 2019—7th ECCOMAS Thematic Conference on Computational Methods in SDEE, Crete, Greece, 24–26.

Cardone, D., Perrone, G. (2015). Developing fragility curves and loss functions for masonry infill walls. Earthquakes and Structures, 9(1), 257-279.

Castaldo, P., Alfano, G. (2019) Seismic reliability-based design of double sliding devices for softening structures. 227-244.

CEN, Eurocode 8 – Part 1 (2004) Design of structures for earthquake resistance—Part 1: General rules, seismic actions and rules for buildings, EN1998-1:2004, European Committee for Standardization, Bruxelles, Belgium

CEN, Eurocode 8 – Part 2 (2005) Design of structures for earthquake resistance—Part 2: Bridges, EN1998-2:2005+A1:2011, European Committee for Standardization, Bruxelles, Belgium

Constantinou, M.C., Tsopelas, P., Kasalanati, A., Wolff, E. (1999) Property Modification factors for seismic isolation bearings. Technical Report MCEER-99-0012, Multidisciplinary Center for Earthquake Engineering Research, Buffalo, New York

Cornell, C. A. (1968). Engineering seismic risk analysis. Bulletin of the seismological society of America, 58(5), 1583-1606.

Cornell, C. A., Krawinkler, H. (2000). Progress and challenges in seismic performance assessment. PEER Center News.

Daniel, W. J. T. (2001). Explicit/Implicit Partitioning of the Generalized Alpha Method. In Computational Mechanics–New Frontiers for the New Millennium (pp. 35-40). Elsevier.

De Domenico, D., Gandelli, E., Quaglini, V. (2020) Adaptive isolation system combining low-friction sliding pendulum bearings and SMA-based gap dampers. ES, 212, 110536.

De Domenico, D., Gandelli, E., Quaglini, V. (2020) Effective base isolation combining low-friction curved surface sliders and hysteretic gap dampers. SDEE, 130, 105989.

De Risi, M.T., Ricci, P., Verderame, G.M. (2017) Modelling exterior unreinforced beam-column joints in seismic analysis of non-ductile RC frames. Earthquake Engineering & Structural Dynamics 46, 899–923. https://doi.org/10.1002/eqe.2835

Decanini, L.D., Liberatore, L., Mollaioli, F. (2014) Strength and stiffness reduction factors for in-filled frames with openings. Earthq. Eng. Eng. Vib. 13, 437–454. https://doi.org/10.1007/s11803-014-0254-9

Di Cesare, A., Ponzo, F.C., Telesca, A. (2021) Improving the earthquake resilience of isolated buildings with double concave curved surface sliders, Engineering Structures, Vol.228, 111498, ISSN 0141-0296. https://doi.org/10.1016/j.engstruct.2020.111498.

Di Cesare, A., Ponzo, F.C., Telesca, A., Nigro, D., et al. (2019) Modelling of the over stroke displacement of Curved Surface Sliders using OpenSEES. OpenSEES Days Eurasia, Hong Kong.

Di Domenico, M., Ricci, P., Verderame, G. M. (2021). Predicting the out-of-plane seismic strength of unreinforced masonry infill walls. Journal of Earthquake Engineering, 25(9), 1788-1825.

Douglas, J. (2017), Ground motion prediction equations 1964-2017, http://www.gmpe.org.uk.

D.M. 30/05/1972. Decreto Ministeriale del 30/05/1972 (1972) Norme tecniche alle quali devono uniformarsi le costruzioni in conglomerato cementizio, normale e precompresso ed a struttura metallica. (in Italian)

D.M. 30/5/1974. Decreto Ministeriale 30 maggio 1974. Norme tecniche per la esecuzione delle opere in cemento armato normale e precompresso e per le strutture metalliche. Gazzetta Ufficiale n. 198 del 29 luglio 1974. (in Italian).

D.M. 27/07/1985. Decreto Ministeriale (DM) del 27/07/1985. Norme tecniche per l'esecuzione delle opere in cemento armato normale e precompresso e per le strutture metalliche, (in Italian)

D.M. 24/1/1986. Decreto Ministeriale 24 gennaio 1986. Norme tecniche relative alle costruzioni antisismiche. Gazzetta Ufficiale n. 108 del 12 maggio 1986. (in Italian).

D.M. 14/2/1992. Decreto Ministeriale 14 febbraio 1992. Norme tecniche per le opere in c.a. normale e precompresso e per le strutture metalliche. Gazzetta Ufficiale n. 65 del 18 marzo 1992. (in Italian).

Eads, L., Miranda, E., Krawinkler, H., & Lignos, D. G. (2013). An efficient method for estimating the collapse risk of structures in seismic regions. Earthquake Engineering & Structural Dynamics, 42(1), 25-41.

FEMA P 695 (2009) Quantification of Building Seismic Performance Factors.

FEMA-356, Prestandard (2000) commentary for the seismic rehabilitation of buildings. Washington, DC: SAC Joint Venture for the Federal Emergency Management Agency.

Fenz, D.M., Constantinou, M.C. (2006) Behavior of the Double Concave Friction Pendulum Bearing. Earthq. Eng. Struct. Dyn, 35, 1403–1424.

Fenz, D.M., Constantinou, M.C. (2008) Mechanical behavior of multi-spherical sliding bearings. Report No. MCEER-08-0007, Multidisciplinary Center for Earthquake Engineering Research, Buffalo, NY.

Fenz, D.M., Constantinou, M.C. (2008) Spherical Sliding Isolation Bearings with Adaptive Behavior: Experimental Verification. Earthq. Eng. Struct. Dyn., 37, 185–205.

Flora, A., Perrone, G., Cardone, D. (2020) Evaluating Collapse Fragility Curves for Existing Buildings Retrofitted Using Seismic Isolation. Appl. Sci. 10, 2844, doi:10.3390/app10082844

Furinghetti, M., Yang, T., Calvi, P.M., Pavese, A. (2021) Experimental evaluation of extra-stroke displacement capacity for Curved Surface Slider devices. Soil Dyn. Earthq. Eng., 146, https://doi.org/10.1016/j.soildyn.2021.106752

Furinghetti, M., Pavese, A., Quaglini, V., Dubini, P. (2019) Experimental Investigation Of The Cyclic Response Of Double Curved Surface Sliders Subjected To Radial And Bidirectional Sliding Motions. SDEE, doi:10.1016/j.soildyn.2018.11.020.

Furinghetti, M., Yang, T., Calvi, P. M., Pavese, A. (2020) Dynamic response of curved surface slider devices under severe input motion. 17WCEE, Sendai, Japan.

Gandelli, E., Quaglini, V., Dubini, P., Limongelli, M.P., Capolongo, S. (2018) Seismic isolation retrofit of hospital buildings with focus on non-structural components, Ingegneria Sismica, Vol. 4, p. 20-56, ISSN: 0393-1420.

Ghafory-Ashtiany, M., Mousavi, M., Azarbakht, A. (2011). Strong ground motion record selection for the reliable prediction of the mean seismic collapse capacity of a structure group. Earthquake Engineering & Structural Dynamics, 40(6), 691-708.

Gutenberg, B., Richter, C. F. (1944). Frequency of earthquakes in California. Bulletin of the Seismological society of America, 34(4), 185-188.

http://itaca.mi.ingv.it [Last access: November 2021].

http://ngawest2.berkeley.edu/ [Last access: November 2021].

http://web.stanford.edu/~bakerjw/research/conditional_spectrum.html [Last access: November 2021].

https://www.fipmec.it/ (FIP MEC srl) [Last access: November 2021].

http://www.reluis.it/ (ReLUIS) [Last access: November 2021].

Ibarra, L.F., Krawinkler, H., (2005). Global Collapse of Frame Structures under Seismic Excitations. Rep. No. TB 152, The John A. Blume Earthquake Engineering Center.

Ibarra, L.F., Medina, R.A., Krawinkler, H. (2005) Hysteretic models that incorporate strength and stiffness deterioration. Earthquake Engng Struct. Dyn. 34, 1489–1511. https://doi.org/10.1002/eqe.495

Iervolino, I., Chioccarelli, E., Convertito, V. (2011) Engineering design earthquakes from multimodal hazard disaggregation, Soil Dynamics and Earthquake Engineering, 31, 1212–1231. doi:10.1016/j.soildyn.2011.05.001.

Iervolino, I., Spillatura, A., and Bazzurro, P. (2018). Seismic Reliability of Code-Conforming Italian Buildings. JEE, 22 (Suppl. 2), 5–7.

Iervolino, I., Spillatura, A., Bazzurro, P. (2019) RINTC-E project: towards the assessment of the seismic risk of existing buildings in Italy, RINTC-e: Towards seismic risk assessment of existing residential reinforced concrete buildings in Italy, in COMPDYN 2019 - 7th ECCOMAS Thematic Conference on Computational Methods in Structural Dynamics and Earthquake Engineering, Crete, Greece.

Jalayer, F., Cornell, C.A., (2002) Alternative Nonlinear Demand Estimation Methods for Probability-Based Seismic Assessments, Earthquake Eng. Struct. Dyn.; 00:1–6

Jayaram, N., Lin, T., Baker, J. (2011) A Computationally Efficient Ground-Motion Selection Algorithm for Matching a Target Response Spectrum Mean and Variance, Earthquake Spectra, Volume 27, No. 3, pages 797–815, August 2011.

Kitayama, S., Constantinou, M.C. (2018) Collapse performance of seismically isolated buildings designed by the procedures of ASCE/SEI 7. Eng Struct 164:243–258.

Kitayama, S., Constantinou, M.C. (2019)a Probabilistic seismic performance assessment of seismically isolated buildings designed by the procedures of ASCE/SEI 7 and other enhanced criteria. ES, 179, 566-582.

Kitayama, S., Constantinou, M.C. (2019)b Effect of displacement restraint on the collapse performance of seismically isolated buildings. BEE, 1-20.

L 1684/1962. Legge 25 novembre 1962, n. 1684 (GU 22 dicembre 1684, n. 326) Provvedimenti per l'edilizia, con particolari prescrizioni per le zone sismiche. (in Italian)

Lin T., Haselton C. B. and Baker, J.W. (2013) Conditional spectrum-based ground motion selection. Part I: Hazard consistency for risk-based assessments, Earthquake Eng. Struct. Dyn. DOI: 10.1002/eqe

Masroor, A., Mosqueda, G. (2012) Experimental simulation of base-isolated buildings pounding against moat wall and effects on superstructure response. EESD, 41(14), 2093-2109.

Masroor, A., G. Mosqueda. (2013) Impact model for simulation of base isolated buildings impacting flexible moat walls. EESD 42.3: 357-376.

Mathworks (2018) T. Matlab. The MathWorks. Línea. Available: https://es. mathworks. com/products/simulink. html.[Last access: November 2021].

Mazza F., Vulcano A. (2012) Effects of near-fault ground motions on the nonlinear dynamic response of base-isolated rc framed buildings. EESD 41.2: 211-232.

McKenna, F., Fenves, G.L., Scott, M.H., Jeremic, B. (2000) Open system for earthquake engineering simulation (OpenSEES). Berkeley (CA): Pacific Earthquake Engineering Research Center, University of California.

McVitty, W. J. and Constantinou, M. C. (2015) Property Modification factors for seismic isolators: design guidance for buildings. Technical Report MCEER-15-0005, Multidisciplinary Center for Earthquake Engineering Research, Buffalo, New York.

Mokha A, Constantinou MC, Reinhorn AM (1990) Teflon Bearings in Base Isolation. I: Testing, ASCE Journal of Structural Engineering, 116(2), 438-454.

Mokha, A.S., Navinchandra, A., Constantinou, M.C., Zayas, V. (1996) Seismic isolation retrofit of large historic buildings, Journal of Structural Engineering, Vol. 122(3), pp. 298–308

Mostaghel, N., Davis, T. (1997) Representations of Coulomb friction for dynamic analysis. Earthquake engineering & structural dynamics, 26(5), 541-548.

Newmark, N. M. (1959) A method of computation for structural dynamics. Journal of the engineering mechanics division, 85(3), 67-94.

NTC 2018, Norme Tecniche per le Costruzioni, Decreto ministeriale del 17 gennaio 2018; Ministero delle Infrastrutture e dei Trasporti: Rome, Italy.

Ponzo, F.C., Di Cesare, A., Telesca, A., Nigro, D., Castellano, M.G., Infanti, S. (2020) Influence of DCCSS Bearings Over-Stroke and breakaway on the seismic response of isolated buildings. Proc. of 17th World Conference on Earthquake Engineering, Sendai, Japan.

Ponzo, F.C., Di Cesare, A., Telesca, A., Pavese, A., Furinghetti, M. (2021) Advanced Modelling and Risk Analysis of RC Buildings with Sliding Isolation Systems Designed by the Italian Seismic Code. Appl. Sci., 11, 1938. https://doi.org/10.3390/app11041938.

Porter, K.A. (2003) An overview of PEER's performance-based earthquake engineering methodology. In Proceedings of ninth international conference on applications of statistics and probability in civil engineering.

Porter, K., Kennedy, R., & Bachman, R. (2007) Creating fragility functions for performance-based earthquake engineering. Earthquake Spectra, 23(2), 471-489.

Presidente del Consiglio dei Ministri (2003) Ordinanza N. 3274 Primi elementi in materia di criteri generali per la classificazione sismica del territorio nazionale e normative tecniche per le costruzioni in zona sismica

Quaglini, V., Dubini, P., Poggi, C. (2012) Experimental assessment of sliding materials for seismic isolation systems, Bulletin of Earthquake Engineering, Springer-Verlag, Berlin Heidelberg (D), Vol. 10, pp. 717-740

Ragni, L., Cardone, D., Conte, N., Dall'Asta, A., Di Cesare, A., Flora, A., Leccese, G., Micozzi, F., Ponzo, C. (2018) Modelling and seismic response analysis of Italian code-conforming base-isolated buildings. JEE, 22 (Suppl. 2), 198–230.

RD 640/1935. Regio Decreto Legge n.640 (GU n. 120, 22/05/1935) NUOVO TESTO DELLE NORME TECNICHE DI EDILIZIA CON SPECIALI PRESCRIZIONI PER LE LOCALITÀ COLPITE DAI TERREMOTI. (in Italian)

RD 2229/1939. Regio Decreto n.2229 (1939) Norme per la esecuzione delle opere in conglomerato cementizio semplice ed armato, n.2229 del 16/11/1939. (in Italian)

ReLUIS-RINTC Workgroup. (2018) Results of the 2015-2017 RINTC Project; ReLUIS-RINTC report; ReLUIS: Naples, Italy.

Ricci, P., Manfredi, V., Noto, F., Terrenzi, M., Petrone, C., Celano, F., De Risi, M.T., Camata, G., Franchin, P., Magliulo, G., et al. (2018) Modeling and Seismic Response Analysis of Italian Code-Conforming Reinforced Concrete Buildings. JEE, 22 (Suppl. 2), 105–139.

Ricci, P., Manfredi, V., Noto, F., Terrenzi, M., De Risi, M.T., Di Domenico, M., Camata, G., Franchin, P., Masi, A., Mollaioli, F., et al. (2019) RINTC-e: Towards seismic risk assessment of existing residential reinforced concrete buildings in Italy. In Proceedings of the COMPDYN 2019—7th ECCOMAS Thematic Conference on Computational Methods in SDEE, Crete, Greece, 24–26.

Ricci, P., Di Domenico, M., & Verderame, G. M. (2020) Effects of the in-plane/out-of-plane interaction in URM infills on the seismic performance of RC buildings designed to eurocodes. Journal of Earthquake Engineering, 1-35.

RINTC Workgroup (2018) Results of the 2015-2017 Implicit seismic risk of code-conforming structures in Italy (RINTC) project. ReLUIS report, Rete dei Laboratori Universitari di Ingegneria Sismica (ReLUIS), Naples, Italy, available at http://www.reluis.it/

RINTC Workgroup (2018) Results of the 2018 Implicit seismic risk of structures in Italy (RINTC) project. ReLUIS report, Rete dei Laboratori Universitari di Ingegneria Sismica (ReLUIS), Naples, Italy, available at http://www.reluis.it/

Ruggieri, S., Uva, G. (2020) Accounting for the Spatial Variability of Seismic Motion in the Pushover Analysis of Regular and Irregular RC Buildings in the New Italian Building Code. Buildings, 10, 177, doi:10.3390/buildings10100177.

Ryan, K.L., Polanco, J. (2008). Problems with Rayleigh damping in base-isolated buildings. Journal of Structural Engineering, 134: 1780–1784

Sarlis, A.A., Constantinou, M.C. (2013) Model of triple friction pendulum bearing for general geometric and frictional parameters and for uplift conditions. Report No. MCEER-13-0010, Multidisciplinary Center for Earthquake Engineering Research, Buffalo, NY.

Sassun, K., Sullivan, T.J., Morandi, P., Cardone, D. (2016) Characterising the in-plane seismic performance of infill masonry. Bulletin of the New Zealand Society for Earthquake Engineer-ing 49(1), 100–117.

Shinozuka, M., Feng, M.Q., Lee, J., et al. (2000) Statistical analysis of fragility curves. Journal of Engineering Mechanics 126: 1224–1231.

Spence, R., Le Brun, B. (2006) "Preface". Bulletin of Earthquake Engineering, 4(4).

Tazarv, M. (2021) SDOF (https://www.mathworks.com/matlabcentral/fileexchange/71787-sdof), MATLAB Central File Exchange.

Touaillon, J. (1870) US PATENT 99973

UNI EN. 15129 (2009) Anti-seismic devices. European committee for standardization (CEN), Bruxelles, Belgium.

Yang, T. (2020) High performance friction-type bearings for seismic isolation. PhD Thesis. University of Washington.

Zayas V.A., Low S.S. and Mahin S.A. (1987) The FPS earthquake protection system, Earthquake Engineering Research Center Report, No. 87-01, Berkeley, California

Zayas, V.A., Low, S.S., Mahin, S.A. (1990) A simple pendulum technique for achieving seismic isolation, Earthquake Spectra, Vol. 6(2), pp. 317-333

Appendix A

```
%% Response of a Linear SDOF DCCSS isolator to an Earthquake Ground Motion
% Solving Equation of Motion using Newmark Method
% (c) Alessio Telesca
% School of Engineering, University of Basilicata, Potenza, Italy
% September 2021
% Version 1.0
%_____________________________________________________________________________
%% Copyright notice
%_____________________________________________________________________________
% For the EOM integration the script set up by Mostafa Tazarv has been used
% Copyright (c) 2019, Mostafa Tazarv
% All rights reserved.
% Redistribution and use in source and binary forms, with or without modification,
% are permitted provided that the following conditions are met:
% * Redistributions of source code must retain the above copyright notice, this list of conditions and the following disclaimer;
% * Redistributions in binary form must reproduce the above copyright notice, this list of conditions and the following
%    disclaimer in the documentation and/or other materials provided with the distribution;
% * Neither the name of South Dakota State University nor the names of its
%    contributors may be used to endorse or promote products derived from this
%    software without specific prior written permission.
% THIS SOFTWARE IS PROVIDED BY THE COPYRIGHT HOLDERS AND CONTRIBUTORS "AS IS"
% AND ANY EXPRESS OR IMPLIED WARRANTIES, INCLUDING, BUT NOT LIMITED TO, THE
% IMPLIED WARRANTIES OF MERCHANTABILITY AND FITNESS FOR A PARTICULAR PURPOSE ARE
% DISCLAIMED. IN NO EVENT SHALL THE COPYRIGHT OWNER OR CONTRIBUTORS BE LIABLE
% FOR ANY DIRECT, INDIRECT, INCIDENTAL, SPECIAL, EXEMPLARY, OR CONSEQUENTIAL
% DAMAGES (INCLUDING, BUT NOT LIMITED TO, PROCUREMENT OF SUBSTITUTE GOODS OR
% SERVICES; LOSS OF USE, DATA, OR PROFITS; OR BUSINESS INTERRUPTION) HOWEVER
% CAUSED AND ON ANY THEORY OF LIABILITY, WHETHER IN CONTRACT, STRICT LIABILITY,
% OR TORT (INCLUDING NEGLIGENCE OR OTHERWISE) ARISING IN ANY WAY OUT OF THE USE
% OF THIS SOFTWARE, EVEN IF ADVISED OF THE POSSIBILITY OF SUCH DAMAGE.
%_____________________________________________________________________________

clc; clear all; close all;

%% INPUT
output_fold='C:\____INPUT OUTPUT FOLDER_____';  % input output folder
Filename=strcat(output_fold,'\OUTPUT_FILE.xlsx');       %Creates an excel file with results
% please note: change the file extension to *.xls according to you MatLab version

%_____DCCSS_PARAMETERS_____________________________________________________________
%_____________________________________________________________________________
g=input;                % The Acceleration of Gravity in the acceleration unit (e.g. mm/s^2)
M= input./g;            % Mass[ton] of SDOF = Weight[N]/g     [N s^2/mm]=[ton]
W=(M*g);                % Weight [N]
d_bd= input;            % Design displacement [mm]
d_c= input;             % Displacement capacity [mm]
mu= input;              % friction coefficient adimensional [-]
```

```
Delta_mu= input;        % friction coefficient increase for the Sliding Regime II, adimensional [-]
R_eff= input;           % Effective curvature radius [mm]
h_s= input;             % Rigid Slider Height [mm]
R_1=((R_eff+h_s)/2);    % Concave surface radius [mm]
K_ini= input;           % Initial Stiffness of the DCCSS isolation system 5000*24=120000 [N/mm]=[kN/m]
mu_2=mu+Delta_mu;       % Sliding Regime II coefficient of friction, adimensional [-]
%_____________________________________________________________________________________

%______RECORD_AND_ANALYSIS_____________________________________________________________
%_____________________________________________________________________________________
Ag=load('INPUT.txt');  % Define Earthquake Motion. INPUT a *.txt file with two columns: 1. Time [s], 2. Acceleration [g]
% please note: INPUT.txt file must be in the 'output folder'
% please note: the INPUT file must not have two or more consecutive null acceleration values
ft=Ag(:,2);             % Ground Acceleration in g
dt= input;              % Time Step of the INPUT Motion [s]
NM=2;                   % Select Newmark Method, 1=Average  2=Linear
Analysis_Break=1;       % The analysis stops (1) or not (0) when the overturning displacement has been reached
%_____________________________________________________________________________________

d_ot=(R_eff/(2*R_1))*(d_c+F_s); % OverTurning displacement [mm]

displ=d_c;              % initial displacement for d_p computing
r_bc=(F_s/2);           % distance between sliding pad Border and slider Centre [mm]
chord=0;                % circumference chord connecting the intersection points between slider and pad circumferences [mm]
beta_angle=0;           % angle described by connecting the intersection points between slider and pad circumferences [rad]
A_ext=0;                % area of the slider external to the sliding pad [mmq]
A_eff=pi*((F_s/2)^2);   % effective area of contact between slider and pad [mmq]
sigma=(W)/A_eff;        % initial pressure for d_p computing
d_p=0;

while sigma<sigma_lim && displ<=(F_s+d_c)
   displ=displ+1;

   r_bc=d_c+(F_s/2)-displ;
   chord=2*(sqrt(((F_s/2)^2)-(r_bc^2)));
   beta_angle=2*asin((chord/2)/(F_s/2));
   A_ext=0.5*((F_s/2)^2)*beta_angle-(chord*(r_bc/2));
   A_eff=pi*((F_s/2)^2)-A_ext;
   sigma=(W)/A_eff;

   if sigma>=sigma_lim
      d_p=displ;
   end

   if displ==(F_s+d_c-1)
      d_p=d_ot;
   end
end

k=W*((1/R_eff)+(mu/d_bd));      % Stiffness of SDOF in force/length (e.g. [N/mm]=[kN/m])
T=2*pi*sqrt(M/k);               % fundamental period
zet=min((100*(2/pi)*(1/((d_bd/(mu*R_eff))+1))),28.); % Damping Ratio in Percent, maximum value = 28%
```

```
if d_p==0
   F_lim=((mu_2*W*(2*R_1/R_eff))+(W*(d_ot/R_eff)));    % limit Force value [N]
else
   F_lim=((mu_2*W*(2*R_1/R_eff))+(W*(d_p/R_eff)));     % limit Force value [N]
end

string1=strcat('Mass is:_',num2str(M),' ton');
string2=strcat('Stiffness is:_',num2str(k),' N/mm');
string3=strcat('Period is:_',num2str(T),' s');
string4=strcat('Damping is:_',num2str(zet),' %');
string4b=strcat('_____________________________________________________________________________');
string5=strcat('Overturning displacement is:_',num2str(d_ot),' mm');

if d_p==d_ot
   string6=strcat('Limit pressure displacement is higher than overturning displacement');
   string7=strcat('Limit Force value is referred to the overturning displacement: F_lim=_',num2str(F_lim),' N');
else if d_p==0
      string6=strcat('ERROR: Limit pressure displacement is reached in static conditions, check the axial load W');
      string7=strcat('Limit Force value is referred to the overturning displacement: F_lim=_',num2str(F_lim),' N');
   else
   string6=strcat('Limit pressure displacement is:_',num2str(d_p),' mm');
   string7=strcat('Limit Force value is referred to the limit pressure displacement displacement: F_lim=_',num2str(F_lim),' N');
   end
end

disp(string1);
disp(string2);
disp(string3);
disp(string4);
disp(string4b);
disp(string5);
disp(string6);
disp(string7);
disp(string4b);

cd(output_fold);




%_____________________________________________________________________________
%% EOM integration
c=2*M*(k/M)^.5*zet/100;

if NM==1
   Gamma=0.5;
   Beta=0.25;
else
   Gamma=0.5;
   Beta=1/6;
end
```

```
a1=M/(Beta*dt^2)+Gamma*c/(Beta*dt);
a2=M/(Beta*dt)+(Gamma/Beta-1)*c;
a3=M*(1/2/Beta-1)+dt*(Gamma/2/Beta-1)*c;
K=k+a1;

u=zeros(length(Ag),1);
v=zeros(length(Ag),1);
ac=zeros(length(Ag),1);
ft(end+1)=0;
Start_Motion=0;

 for i=1:length(u)-1
    u(1,1)=0;                    %initial conditions
    v(1,1)=0;
    ac(1,1)=0;

%_______START_OF_MOTION_________INITIAL_STIFFNESS_________________
%_____________________________________________________________________
     if Start_Motion==0
    if u(i)<d_yield
        k=K_ini;      % Stiffness of SDOF in force/length (e.g. [N/mm]=[kN/m])
        c=2*M*(k/M)^.5*zet/100;
        a1=M/(Beta*dt^2)+Gamma*c/(Beta*dt);
        a2=M/(Beta*dt)+(Gamma/Beta-1)*c;
        a3=M*(1/2/Beta-1)+dt*(Gamma/2/Beta-1)*c;
        K=k+a1;

    else
          k=W*((1/R_eff)+(mu/d_bd));      % Stiffness of SDOF in force/length (e.g. [N/mm]=[kN/m])
          c=2*M*(k/M)^.5*zet/100;
          a1=M/(Beta*dt^2)+Gamma*c/(Beta*dt);
          a2=M/(Beta*dt)+(Gamma/Beta-1)*c;
          a3=M*(1/2/Beta-1)+dt*(Gamma/2/Beta-1)*c;
          K=k+a1;

          Start_Motion=1;
    end
    end
%_____________________________________________________________________


%____________OVER_STROKE_REGIME_________MU_2_____________________
%_____________________________________________________________________
    if abs(u(i))>=d_c
          k=W*((1/R_eff)+(mu_2/d_bd));      % Stiffness of SDOF in force/length (e.g. [N/mm]=[kN/m])
          c=2*M*(k/M)^.5*zet/100;
          a1=M/(Beta*dt^2)+Gamma*c/(Beta*dt);
          a2=M/(Beta*dt)+(Gamma/Beta-1)*c;
          a3=M*(1/2/Beta-1)+dt*(Gamma/2/Beta-1)*c;
          K=k+a1;
```

```
    else
        k=W*((1/R_eff)+(mu/d_bd));      % Stiffness of SDOF in force/length (e.g. [N/mm]=[kN/m])
        c=2*M*(k/M)^.5*zet/100;
        a1=M/(Beta*dt^2)+Gamma*c/(Beta*dt);
        a2=M/(Beta*dt)+(Gamma/Beta-1)*c;
        a3=M*(1/2/Beta-1)+dt*(Gamma/2/Beta-1)*c;
        K=k+a1;
    end
%_____________________________________________________________


    p=-g*M*ft(i+1)+a1*u(i,1)+a2*v(i,1)+a3*ac(i,1);
    u(i+1,1)=p/K;
    v(i+1,1)=Gamma/(Beta*dt)*(u(i+1,1)-u(i,1))+(1-Gamma/Beta)*v(i,1)+dt*(1-Gamma/2/Beta)*ac(i,1);
    ac(i+1,1)=1/Beta/dt^2*(u(i+1,1)-u(i,1))-1/Beta/dt*v(i,1)-(1/2/Beta-1)*ac(i,1);
 end

ft(end)=[];

      xlswrite(Filename,u,"u","B2");              %Inserisce la matrice tabella nel file

      string4='EOM Integration Completed';
      disp(string4);



%_____________________________________________________________________________________________
      %% Friction Force Computation

  dispX=u;            % displacement input [mm]
  L=length(dispX);
  Force_X_base=zeros(L,1);
  Force_X=zeros(L,1);
  Jump_X=zeros(L,1);
  Jump_I=2*mu*W;
  Jump_II=2*(mu+Delta_mu)*W;

  i=1;

   while i<=(L-1)
            if dispX(i)<=(-d_c)
            Force_X_base(i)=-((mu_2*W*(2*R_1/R_eff))-(W*(dispX(i)/R_eff)));
            Jump_X(i)=(2*mu_2*W);
             else
                if dispX(i)<=0
                Force_X_base(i)=-(((mu*W*(2*R_1/R_eff))-(W*dispX(i)/R_eff)));
                Jump_X(i)=(2*mu*W);
                  else
                   if dispX(i)<d_c
                   Force_X_base(i)=(mu*W*(2*R_1/R_eff))+(W*dispX(i)/R_eff);
                    Jump_X(i)=-(2*mu*W);
```

```
            else
            Force_X_base(i)=((mu_2*W*(2*R_1/R_eff))+(W*(dispX(i)/R_eff)));
            Jump_X(i)=-(2*mu_2*W);
          end
        end
      end



if Analysis_Break==1
  if abs(dispX(i))>=d_ot
      string4='The Overturning displacement has been reached. Analysis concluded.';
      disp(string4);
     break
  end
end



  if abs(dispX(i))<abs(dispX(i+1))
    Force_X(i)=Force_X_base(i);
  else
    F_Jump(i)=(Force_X_base(i)+Jump_X(i));
      if abs(Force_X(i-1))<abs(F_Jump(i))
        Force_X(i-1)=F_Jump(i);
      else
        yp=Force_X_base(i-1);
        xp=dispX(i-1);
          if dispX(i)<=(-d_c)
                while ((abs(Force_X(i-1)-yp))<Jump_II) && (abs(dispX(i))>abs(dispX(i+1))) && (i<(L-1))
                Force_X(i)=yp+(K_ini*(dispX(i)-xp));
                i=i+1;
                end
           else
              if dispX(i)<=0
                 while ((abs(Force_X(i-1)-yp))<Jump_I) && (abs(dispX(i))>abs(dispX(i+1))) && (i<(L-1))
                 Force_X(i)=yp+(K_ini*(dispX(i)-xp));
                 i=i+1;
                 end
               else
                    if dispX(i)<d_c
                       while ((abs(Force_X(i-1)-yp))<Jump_I) && (abs(dispX(i))>abs(dispX(i+1))) && (i<(L-1))
                       Force_X(i)=yp+(K_ini*(dispX(i)-xp));
                       i=i+1;
                       end
                    else
                        if dispX(i)>=d_c
                           while ((abs(Force_X(i-1)-yp))<Jump_II) && (abs(dispX(i))>abs(dispX(i+1))) && (i<(L-1))
                           Force_X(i)=yp+(K_ini*(dispX(i)-xp));
                           i=i+1;
                         end
```

```
                                end
                            end
                        end
                    end
                end
            end
 i=i+1;
end

    xlswrite(Filename,Force_X,"Foglio1","C3");                  % writes Forces in the excel file
    xlswrite(Filename,cellstr('Force'),"Foglio1","C1");         % writes 'Force' label
    xlswrite(Filename,dispX,"Foglio1","B3");                    % writes Displacements in the excel file
    xlswrite(Filename,cellstr('Displacement'),"Foglio1","B1");  % writes 'Displacement' label

    string4='END';
    disp(string4);

cd(output_fold);
```